

ABSTRACT

Falzone, Alec Jacob. Accessing Long-Lived Excited States Through MMCT in Oxido-Bridged Heterobimetallic Molecules Containing First-Row Transition Metals. (Under the direction of Professor Walter W. Weare)

Photochemical transformations of organic molecules require a photocatalyst whose excited state lifetime is long-lived (\approx ns), with redox properties tuned to match the reactions of interest. The work presented herein explores a new type of molecular chromophore that utilized metal-to-metal charge transfer (MMCT) to generate redox-active metal centers after excitation. These new chromophores are derived from an unsupported, terminal M^{III} hydroxide ($M = Cr, Fe, \text{ or } Co$) that have such properties. The protic nature of the metal hydroxides allows for the design of covalently bonded, oxido-bridged heterobimetallic complexes, which contain a Ti^{IV} electron acceptor. These molecules exhibit a charge-transfer band with significant intensity that can be tuned throughout the UV-Vis spectrum through both donor metal substitution and ligand variation. The strongly reducing (> 2.0 eV vs. Fc/Fc^+) transient Ti^{III} species, in combination with the long-lived excited state, make this class of molecules an alternative to traditional photoredox MLCT-based catalysts. Understanding observed characteristics of the ground state in addition to relaxation pathways and excited state properties were explored through various electrochemical and spectroscopic techniques.

© Copyright 2017 Alec Jacob Falzone

All Rights Reserved

Accessing Long-Lived Excited States Through MMCT in Oxido-Bridged Heterobimetallic
Molecules Containing First-Row Transition Metals

by
Alec Jacob Falzone

A dissertation submitted to the Graduate Faculty of
North Carolina State University
in partial fulfillment of the
requirements for the degree of
Doctor of Philosophy

Chemistry

Raleigh, North Carolina

2017

APPROVED BY:

Dr. Walter W. Weare
Committee Chair

Dr. David Shultz

Dr. Elon Ison

Dr. Paul Maggard

DEDICATION

I would like to dedicate this to my closest friends and family who have provided me with a support system to overcome many obstacles both personally and professionally. Firstly, without the support, encouragement, and advice throughout my academic career from my better half Samantha Smith, none of this work would have been possible. I'd also like to acknowledge my parents and sister (Carlo, Eva, and Lauren Falzone) for always being available for support and advice. In addition, my maternal grandparents Helen and Joseph Csoke have always been supportive of my professional achievements and for that I am forever grateful.

BIOGRAPHY

Alec Falzone was born and raised in Palos Hills, IL, a suburb on the South Side of Chicago. He graduated from Amos Alonzo Stagg High School in 2008 where he was involved in numerous varsity sports in addition to developing a passion for music. Alec then attended Iowa State University in Ames, IA where he obtained his B.S. in Chemistry in 2012. While at ISU he joined the newly formed research group of Dr. Javier Vela where he synthesized Pd^{II} complexes for the co-polymerization of α -olefins in addition to various capping ligands for CdS/CdSe quantum dots. In October of 2012 he began his graduate school career under the direction of Dr. Walter W. Weare at North Carolina State University.

ACKNOWLEDGMENTS

I would like to thank NC State University and the Chemistry Department for provided the funding and facilities necessary to carry out these research endeavors. I'd also like to thank my advisor, Dr. Walter Weare, for his guidance throughout the past 9 semesters. I'd also like to thank my committee and other members of the Inorganic Chemistry division for their scientific suggestions and assistance in preparing this document and presentation.

I'd like to thank former group members Dr. Aaron Francis and Dr. Jürgen Bartelmess for assistance in learning new synthetic techniques in addition to the intricacies of electrochemistry. Gratitude to Dr. Eric Goggins and Dr. Xinyuan Wu are also given for their collaborative synthetic efforts and spectroscopic advice. I have also been fortunate enough to have worked with many talented undergraduate students while at NC State University, with contributions from John Nguyen included in this document.

Collaborative efforts with Dr. Jennifer Roizen at Duke University have also been immensely beneficial while working on the Manganese oxygen atom transfer catalysis project. Former group member Dr. Tao Huang made initial discoveries and laid the foundation for future advancements.

Without the assistance from Dr. Felix Castellano and his talented group members, the investigation of these new molecules would not have been possible. I'd like to especially thank Dr. Catherine McCusker for her assistance with initial transient absorption measurements and instrument training. I'd also like to thank senior graduate students

Rosalynd Joyce, Michelle McGoorty, Karim El Roz, James Yarnell, and Sofia Garakyaraghi for their instrumental assistance and data analysis throughout the duration of this work.

I'd also like to thank Dr. Roger Sommer for his excellent X-ray crystallography work and experimental suggestions. And finally, I'd like to thank current and former members of the Gorman and Shultz Groups for their helpful advice and sense of community over the past five years.

TABLE OF CONTENTS

List of Tables		ix
List of Figures		x
Chapter 1: An Introduction to Solar Energy Research		
1.1: The Broader Impacts of Solar Energy Research Efforts.....		1
1.2: Photovoltaic Cells and Photosynthesis: Current Approaches to Solar Energy..		3
1.3: Metal-to-Metal Charge Transfer in Molecules and on Surfaces.....		8
1.4: Electronic Coupling: An Introduction to Selection Rules, Franck-Condon, and Marcus Theory.....		12
1.5: Electron Transfer Between Two Systems: Marcus Theory.....		16
1.6: Distinguishing Between Förster and Dexter Energy Transfer.....		21
1.7: Cited References.....		24
Chapter 2: Synthesis and Ground State Characterization of Terminal Metal Hydroxide Complexes		
2.1: Reactivity of Supported and Unsupported Metal Hydroxides.....		27
2.2: Synthesis of Py ₅ Me ₂ Ligand.....		31
2.3: Synthesis and Bonding Analysis of the Electron Donor Source: Unsupported Terminal Metal Hydroxides.....		32
2.4: Geometric Characteristics of Synthesized Terminal Metal Hydroxides.....		38
2.5: Ground State Electronic Properties of M ^{III} OH Complexes.....		40
2.6: Redox Characteristics of M ^{III} OH Complexes.....		43

2.7:	Cited References.....	45
Chapter 3: Synthesis and Ground State Characterization of Oxido-Bridged Heterobimetallic Complexes		
3.1:	Structure and Bonding in Single Atom Bridged M-A-M Complexes.....	51
3.2:	Design of the Electron Acceptor: A Ti^{IV} d^0 Titanatane.....	59
3.3:	Synthetic Strategy and Bonding Present in Oxido-Bridged Heterobimetallic Complexes.....	62
3.4:	Ground State Characterization of Oxido-Bridged Heterobimetallic Complexes.....	68
3.5:	Structural Characteristics of Oxido-Bridged Heterobimetallic Complexes....	74
3.6:	Cited References.....	77
Chapter 4: Excited State Dynamics Following Charge Transfer in Oxido-Bridged Complexes		
4.1:	Excited State Dynamics in Six-Coordinate Cr^{III} Complexes.....	79
4.2:	Charge Transfer Dynamics in CrOH	80
4.3:	Excited State Dynamics in $\text{Cr}^{\text{III}}\text{OTi}^{\text{IV}}$: Evidence for Indirect MMCT.....	87
4.4:	Excited State Characterization of $\text{Fe}^{\text{III}}\text{OTi}^{\text{IV}}$: Iron-Based Molecule with a Nanosecond Lifetime.....	96
4.5:	Cited References.....	99

Chapter 5: Advancements in the Understanding of Atom Transfer Reactivity in Manganese (III) Porphyrin Complexes	
5.1: An Introduction to Oxygen Atom Transfer Chemistry in Mn (III) Complexes	101
5.2: Synthesis and Ground State Characterization of MnTPP(DMF)	102
5.3: Epoxidation Trials of <i>cis</i> - β -Methyl Styrene with MnTPP(DMF)	104
5.4: NIR Measurements of d-d Bands in Select Mn(Porphyrin)(L) Catalysts	105
5.5: Cited References	109
Appendix A: Supporting Information for Reported Molecules	111
Appendix B: Electronic Absorption Spectra	122
Appendix C: Fourier Transform Infrared Spectra	128
Appendix D: Electrochemistry Supplemental Information and Voltammograms	135
Appendix E: Nuclear Magnetic Resonance Spectra	142
Appendix F: Transient Absorption and Emission Spectra	143
Appendix G: Single Crystal Data	155

LIST OF TABLES

Table 2.1:	Measured Stretching Frequencies of ν_{OH} in $\text{M}^{\text{III}}\text{OH}$ Complexes.....	36
Table 2.2:	Selected Metal-Ligand Bond Lengths in Terminal Metal Hydroxides.....	42
Table 2.3:	$E_{1/2}$ Potentials for the $\text{M}^{\text{III/IV}}$ Oxidative Couples in the Terminal $\text{M}^{\text{III}}\text{OH}$ Complexes.....	46
Table 3.1:	Experimentally Obtained m/z Values Through HR-ESI/MS Measurements..	63
Table 3.2:	$E_{1/2}$ Potentials Obtained Via Cyclic Voltammetry of Heterobimetallic Complexes.....	72
Table 3.3:	Select Bond Lengths and Angles Obtained for $\text{Cr}^{\text{III}}\text{OTi}^{\text{IV}}$ and $\text{Co}^{\text{III}}\text{OTi}^{\text{IV}}$	75
Table 5.1:	Catalytic Data for the Epoxidation of <i>cis</i> - β -Methyl Styrene using $\text{MnTPP}(\text{DMF})$	105
Table 5.2:	NIR Measurements of d-d Bands in Select Mn^{III} Porphyrin(L) Catalysts....	107
Table 5.3:	d-d Band Energies and Catalytic Data in Select $\text{MnTPP}(\text{L})$ Complexes.....	108

LIST OF FIGURES

Figure 1.1:	Projected Worldwide Energy Consumption Totals.....	2
Figure 1.2:	Measured PV Cell Efficiencies for Various Types of Cells through 2015.....	4
Figure 1.3:	Reaction Diagram for Water Oxidation.....	5
Figure 1.4:	Simplified Photosynthesis Diagram as Represented by the Z-Scheme.....	6
Figure 1.5:	Reported EAS of Heterobimetallic Complexes by Wagenknecht.....	10
Figure 1.6:	HOMO/LUMO Calculations of Heterobimetallic Molecules.....	11
Figure 1.7:	Classic Potential Well Diagram Depicting the Franck-Condon State.....	14
Figure 1.8:	Potential Energy Well Diagram as Described Through Marcus Theory.....	18
Figure 1.9:	Jablonski Diagram Depicting Förster Resonance Energy Transfer.....	22
Figure 1.10:	Radiationless Dexter Energy Transfer Between Systems.....	23
Figure 2.1:	Initial Supported Terminal Metal Hydroxide Molecule by Borovik.....	27
Figure 2.2:	Heterometallic Synthesis Pathway for Oxido-Bridged Complexes.....	29
Figure 2.3:	NBO Analysis of Oxygen Atom's Effects in Oxido-Bridged Complexes.....	30
Figure 2.4:	Synthetic Scheme of Py_5Me_2	32
Figure 2.5:	Synthetic Scheme of Terminal Metal Hydroxides.....	33
Figure 2.6:	FTIR Spectrum of ν_{OH} in CrOH.....	35
Figure 2.7:	Created ML_5O Molecular Orbital Fragment for a Model Complex.....	38
Figure 2.8:	Single Crystal Structure of CrOH.....	40
Figure 2.9:	Single Crystal Structures of FeOH and CoOH.....	41
Figure 2.10:	Solvent Effects on Absorption Bands in CrOH.....	43

Figure 2.11:	Molar Absorptivity Plot of CrOH, FeOH, and CoOH.....	44
Figure 2.12:	Cyclic Voltammogram Depicting Electrochemical Reversibility in FeOH...	46
Figure 3.1:	Reported Homobimetallic Ruthenium Complex.....	51
Figure 3.2:	Qualitative MO Diagram Supported by Electrochemistry of a Ru ^{III} -O- Ru ^{III} (bpy) dimer.....	53
Figure 3.3:	Relative Energies of Frontier Orbitals in M-O-M Complexes.....	54
Figure 3.4:	Frontier Molecular Orbitals in a Non-Linear Fe ^{III} -O-Fe ^{III} Complex.....	57
Figure 3.5:	Synthesis of the Asymmetric Methyl TiO ⁱ Pr Complex.....	59
Figure 3.6:	Synthesis of Analogous Ti ^{IV} Alkoxide Complexes.....	60
Figure 3.7:	EAS of TiO ⁱ Pr in Dichloromethane.....	61
Figure 3.8:	Synthetic Scheme for all Heterobimetallic Complexes Synthesized.....	62
Figure 3.9:	Simplified Homobimetallic M-O-M' MO Diagram.....	64
Figure 3.10:	Derived Heterobimetallic Complex M-O-M' MO Diagram.....	66
Figure 3.11:	EAS Difference Spectrum of Cr ^{III} OTi ^{IV} with Fitted Gaussians.....	68
Figure 3.12:	EAS Difference Spectrum of Fe ^{III} OTi ^{IV} with Fitted Gaussian.....	69
Figure 3.13:	EAS Difference Spectrum of Co ^{III} OTi ^{IV}	70
Figure 3.14:	Single Crystal Structures Obtained for Cr ^{III} OTi ^{IV} and Co ^{III} OTi ^{IV}	74
Figure 4.1:	Static Transient Absorption Spectrum of CrOH in DCM.....	80
Figure 4.2:	Transient Decay Kinetics at Room Temperature of CrOH.....	81
Figure 4.3:	Excitation Wavelength Dependence Plot of CrOH.....	82
Figure 4.4:	Photodecomposition as Evident in the EAS of CrOH in DCM.....	83

Figure 4.5:	Fluorescence Decay Fit of CrOH at Room Temperature.....	84
Figure 4.6:	Proposed Relaxation Mechanism Following Excitation in CrOH.....	85
Figure 4.7:	Initially Proposed Three State Model in Cr ^{III} OTi ^{IV}	87
Figure 4.8:	Static Transient Absorption Spectrum and Decay Kinetics of Cr ^{III} OTi ^{IV}	88
Figure 4.9:	Spectral Map of Cr ^{III} OTi ^{IV} in DCM at Room Temperature.....	89
Figure 4.10:	Probe Dependence Plot of the Pre-Exponential Term of Cr ^{III} OTi ^{IV}	90
Figure 4.11:	Arrhenius Plot of τ_1	91
Figure 4.12:	Arrhenius Plot of τ_2	92
Figure 4.13:	Uncorrected Emission Spectrum of Cr ^{III} OTi ^{IV}	93
Figure 4.14:	Proposed Jablonski Diagram of the Nanosecond CT Dynamics in Cr ^{III} OTi ^{IV}	94
Figure 4.15:	Ultrafast Spectral Map of Fe ^{III} OTi ^{IV} in DCM at Room Temperature.....	96
Figure 4.16:	Bleach Recovery Kinetic Analysis of Fe ^{III} OTi ^{IV}	97
Figure 5.1:	Synthesis of the 5-Coordinate MnTPP(DMF) Catalyst.....	103
Figure 5.2:	Orbital Occupancy in Pentacoordinate Mn ^{III} Complexes.....	106

1 Chapter 1: An Introduction to Solar Energy Research

1.1 The Broader Impacts of Solar Energy Research Efforts

Modern society's dependence on fossil fuels as the overwhelming generator of electricity and transportation means is not a long-term sustainable model. According to the United States Energy Information Administration (EIA) the worldwide amount of marketed energy consumption has been projected to increase 48% from the year 2012 – 2040.¹ It is important to note these projections do not take into account any future regulations on fossil fuel consumption or changes to emission standards worldwide. Nor does this projected increase in energy demand include legislation enacted in the United States or elsewhere between 2012 and the current date. The bulk of the increase in energy consumption will be derived from countries whose economies are growing at some of the fastest rates over the past decade, and are not members of the Organization for Economic Co-operation and Development (OECD).² In the reproduced graph from the EIA's report below¹, the data depicts the total amount of energy consumed (in quadrillion Btu) from various sources starting in the year 1990 and projected through the year 2040. The bulk of the energy consumption worldwide is unsurprisingly fossil fuel-based, which includes natural gas, liquid petroleum products, and coal. It is somewhat encouraging to note that the rate of coal consumption per annum has been projected to decrease through the year 2040. However, the gross amount of coal consumed per year is still projected to increase each year throughout the report. The CPP designations in **Figure 1.1** represent the projected effects the Clean Power Plan will have on the energy produced from coal and renewables sources following approval.³

The green line in **Figure 1.1** represents the total amount of energy originating from renewable sources. The majority of this renewable energy production involves hydroelectric dams (which have their own adverse environmental impacts) and wind turbines. Less than 33% of the worldwide renewable energy production originates from sources other than hydroelectric dams or wind turbines, of which solar energy production is a contributor.¹ Within OECD member countries, the majority of growth in the renewable energy sector has

been from solar resources. This growth can be attributed to generous tax incentives put in place by government entities, in addition to decreasing costs of raw materials used in traditional single band gap semiconductors. With the flux of new photovoltaic devices increasing every year, many observers would expect the growth of solar-derived energy to be much greater than it has been. Much of this can be attributed to the theoretical limits of traditional single band gap semiconductors, otherwise known as the Shockley-Quiesser

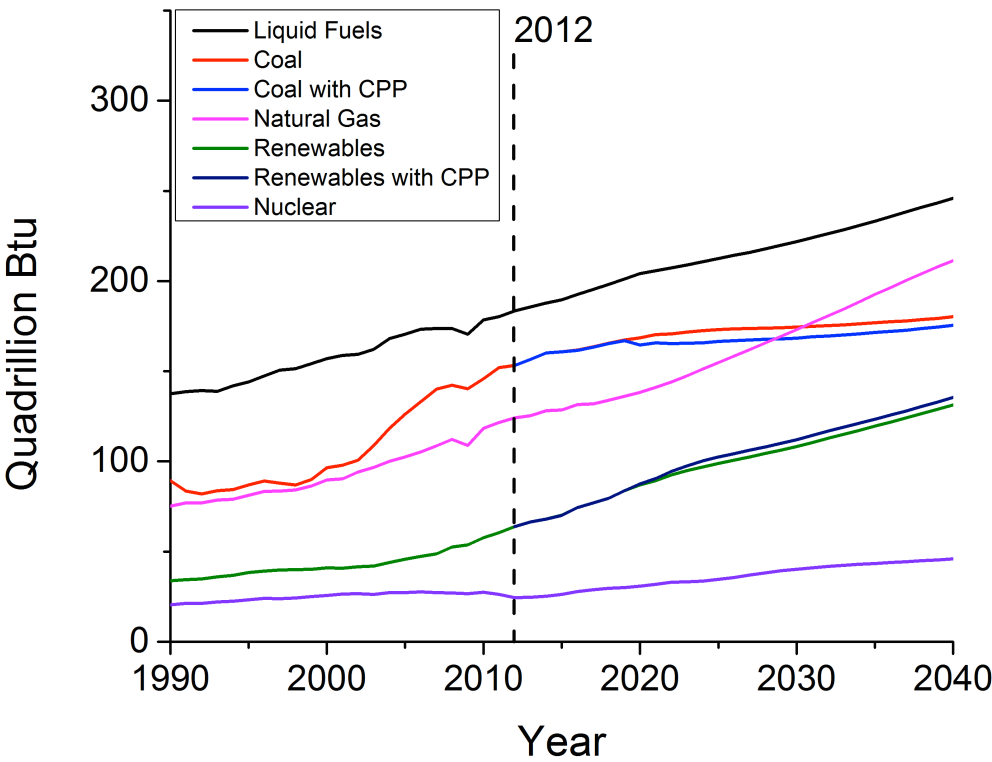


Figure 1.1 World Energy Consumption by Source from 1990 Projected Through 2040

limit.⁴

This innate technological barrier has prevented the employment of many solar-producing devices and has left the door open for alternative means for harnessing the enormous amount of energy absorbed by the Earth from the Sun (TW). Identifying this glaring need for technologies that are both cost-effective and efficient in harnessing the Sun’s energy for energy production allows us to envision an alternative way to absorb these photos

in a new and exciting way. One alternative way to harness the Sun's photons to produce consumable energy is to produce a solar fuel. Solar fuel production has been in existence in nature for billions of years in the form of photosynthesis, which is how plants store energy in chemical bonds through a series of electron transfer steps. An overview of both solar fuel production (photosynthesis) and photocurrent generation (photovoltaic cells) will be presented at length in the next section of this document. This dissertation explores the synthesis and fundamental chemistry of a new chromophore which shows immense promise as a photocatalyst for the production of solar fuels.

1.2 Photovoltaic Cells and Photosynthesis: Current Approaches to Solar Energy

There are two current and functional approaches to harnessing the Sun's energy for human consumption, one of which is a photovoltaic cell (PV) that uses electron/hole pairs for photocurrent generation. The other is artificial photosynthesis, which aims to mimic the process that nature has evolved over billions of years.

Photovoltaic cells are currently the most popular method for harvesting solar energy. These traditional solar panels use a semiconductor to convert sunlight into electric current. Research and development of photovoltaic cells has progressed alongside other semiconductor technologies. Most photovoltaic panels available commercially are composed of crystalline silicon, with a maximum operating efficiency of 25.0%.⁵ Other semiconducting materials suitable for PVs are known, but are cost-prohibitive. Maximum theoretical operating efficiency has been shown to be 33.7% by Shockley and Queisser for a single band-gap semiconductor.⁴ Crystalline silicon's efficiency has been measured at 29.0%, which leaves little to no realistic improvement over the currently maximum production efficiency.⁵ The development of more efficient PVs has neared its ceiling, and the efficiency of crystalline silicon PV's has risen by less than 5% over the last 24 years.⁵ Increases in operating efficiency has been observed in almost every type of photovoltaic cell developed thus far, which is depicted in an adapted figure from the NREL in **Figure 1.2**.⁶ The cost of electricity produced by PV's has decreased dramatically since their introduction, however they remain priced out of most markets when compared to fossil fuels.⁵

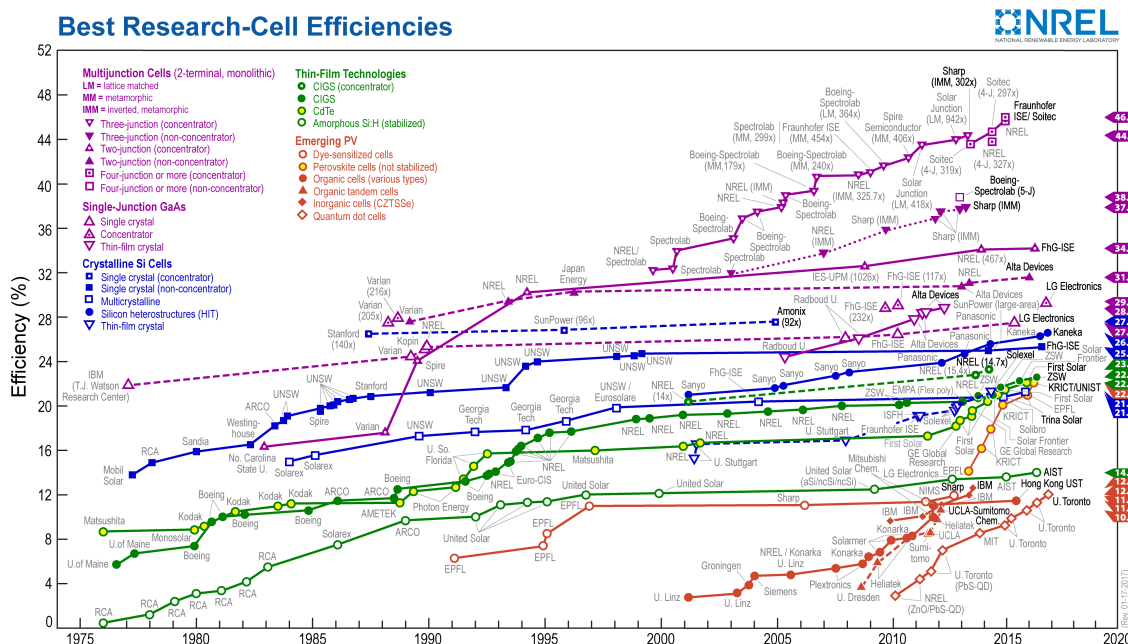


Figure 1.2 Optimum Operating Cell Efficiencies for Various Types of Photovoltaic Cells (1975 – 2015)

The reason PVs have been regarded as the energy source of the future is their well-established reputation and clean method of electricity production. They work well when there is an abundance of photons such as during daylight hours. However, they produce no electricity in the dark due to the lack of sunlight. Currently, there is no cost-effective energy storage technology for solar to electricity conversion. Therefore, the power must be consumed as it is produced. Industrial-scale electrolyzers have been proposed, but remain too inefficient and cost-prohibitive for large-scale deployment.⁷ Admittedly, the energy storage issue is the only technological hurdle PV's need to overcome to be humanity's best option for sustainable energy production.

However, to date battery technology has not been able to provide the needed storage on a large scale for commercial electric grid-scale implementation.⁸ One substitute for photovoltaic cells is to store photo-generated energy in chemical bonds rather than electrical current. This approach to alternative energy production is better known as artificial photosynthesis or solar fuel production. In order to understand the motivations behind creating artificial photosynthesis, we must take a closer look at the chemistry of natural

photosynthesis. It is important to note there is a distinct difference between photosynthetic approaches to alternative energy production (solar fuels) and the more studied photocatalytic pathways. A recent review by Osterloh at the University of California-Davis describes this difference in great detail.⁹ One important distinction between the two is the thermodynamic requirements for a system to be considered photosynthetic versus photocatalytic is much different. In a traditional sense, catalysts speed up reactions through lowering the energy barrier. However, in most photochemical reactions, photocatalysts are only able to speed up chemical processes that are already thermodynamically downhill ($\Delta G < 0$). On the other hand, molecules or devices that are capable of artificial photosynthesis possess the ability to drive energetically uphill ($\Delta G > 0$) reactions. This process of storing energy in chemical bonds utilizes absorbed photons to drive these energetically demanding chemical reactions, which otherwise would not occur.

Natural photosynthesis is a process that has been evolving over billions of years in plants and bacteria. Photosystem I (PSI) and Photosystem II (PSII) are the major components of photosynthesis, with the initial charge separated electron for the electron transport chain (ETC) generated in PSII. Photon absorption by chlorophyll pigments initiates charge separation, with the excited electron entering the ETC. Water oxidation occurs concomitantly to this and is depicted in **Figure 1.3**.



Figure 1.3 Water Oxidation Produces Molecular Oxygen, Protons, and Measureable Electric Current

Initial charge separation in PSII results in the formation of P680^{*+} , the cationic radical state of P680. In natural photosynthesis, the absorption profile of chlorophyll pigments has a selective range of photons to induce charge separation. P680 has λ_{max} values of ≈ 440 nm and 680 nm, with limited absorption outside these two peak maxima.¹⁰ This long-lived charge separated excited state is the result of a triplet excited state formation ($^3\text{P680}$), localized on one of the Ch1 molecules.¹¹ Water oxidation in PSII is performed by the inorganic cluster Mn_4CaO_5 , otherwise known as the oxygen evolving complex (OEC). This cluster is capable of extracting electrons from a poor electron donor, such as water, and

catalytically driving the reaction depicted in **Figure 1.3**. The cation radical $P680^{*+}$ present after charge separation, withdraws electrons from this Mn-centered cluster with single-electron driven photoreactions. The charge-separated lifetime of $P680^{*+}$ is approximately 10 ps, with the total photosynthetic process requiring between 5 to 30 milliseconds for NADPH creation.¹²

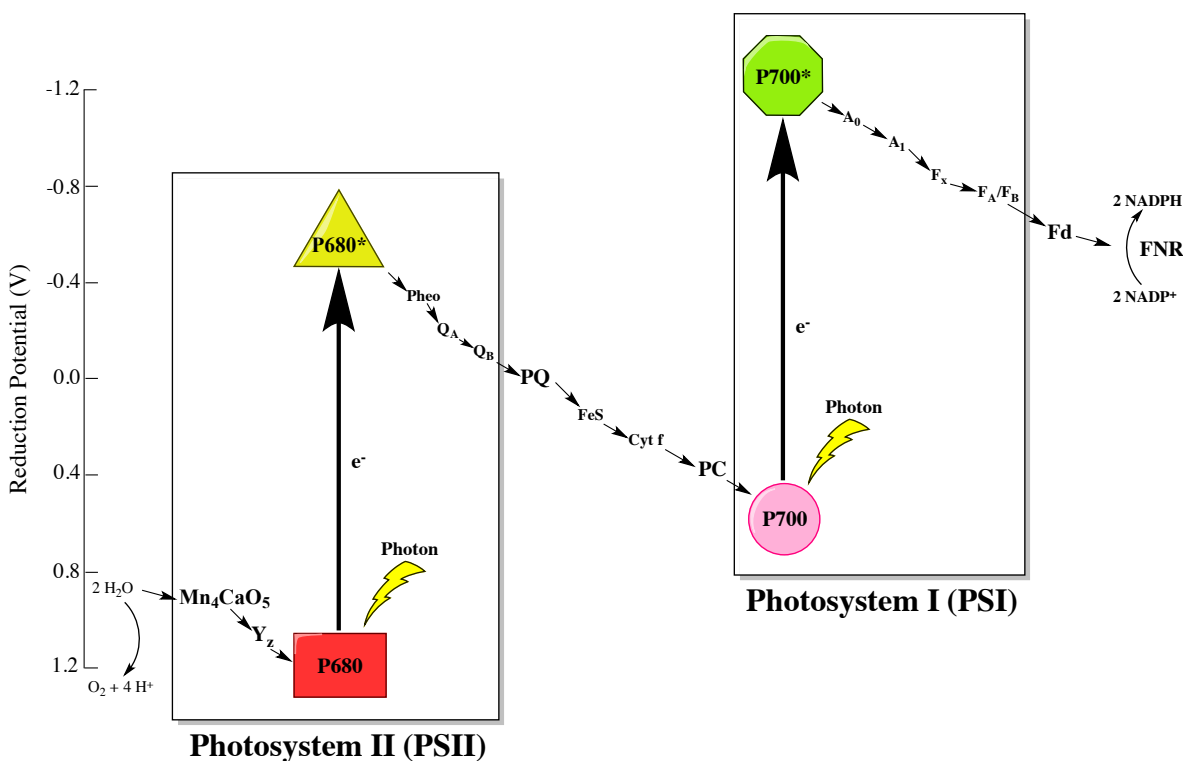


Figure 1.4 Simplified charge carrier process throughout the natural photosynthetic process, known as the Z-Scheme. Reduction potentials are reported versus NHE. Figure adopted from Govindjee et. al.¹²

Following the induced singlet excited state in $P680^{*+}$, the electron proceeds through the electron transport chain (ETC) through multiple steps as seen in **Figure 1.4**.¹² This process ultimately fills the photogenerated hole in PSI, concluding with the reduction of $NADP^{+}$ to form NADPH after a second excitation. NADPH is primarily consumed in the light-independent Calvin cycle, which fixes carbon dioxide and synthesizes carbohydrates.

Solar-to-fuels conversion has yet to be efficiently and competitively demonstrated artificially, however recent discoveries are moving us towards this goal. A major issue in artificial systems is the low quantum efficiency for fuel production. In natural systems, the

probability of charge recombination is extremely small due to the nature of the ETC. The ETC is a systematic process of sequential one electron hopping steps from donor to acceptor. This is opposite from synthetic systems where electrons often transfer directly from donor to acceptor through a one-step tunneling process. Reverse electron transfer back to the ground state in natural systems is not favored following the forward pathway due to the multiple one-electron steps. Potential relaxation occurs via a tunneling process back to the original electron donor. Both of these processes lead to extremely long excited state lifetimes in natural systems. However, this approach in artificial photosynthetic such control is not synthetically possible to date. Thus, the high probability of charge recombination is an issue that is amplified when short excited-state lifetime chromophores are utilized, and needs to be addressed.¹³

One of the most recent examples of a functional mimic of natural photosynthesis is that of Nocera and coworkers. Their system, the “Artificial Leaf”, uses a triple junction technology with various materials to mimic the entire fuel cycle of photosynthesis.¹⁴ The designed PSII OEC mimic in this system employs Co^{2+} and phosphate anions to self-assemble as a film on the silica surface in aqueous solution.^{15, 16} Upon realization that non-precious metals could be used to mimic the OEC, a NiMoZn metal alloy was then developed as a high-surface area material to perform hydrogen evolution, the synthetic variant of NADPH.¹⁴ Their maximum instantaneous solar-to-fuels conversion power efficiency was determined to be 2.5% in the wireless configuration under 1 sun irradiation. While the conversion seems low, it is an important step forward to mimic photosynthesis synthetically through the utilization of Earth-abundant materials. Although this tandem catalytic system does not store energy as carbohydrates, the authors claim the combination of $\text{H}_{2(g)}$ with incoming $\text{CO}_{2(g)}$ could render this conversion possible in the future. The $\text{O}_{2(g)}$ that is generated throughout this process would then be separated from this mixture to be subsequently stored for later use, or released into the atmosphere through engineering modifications.

One other approach to mimicking photosynthesis in synthetic systems uses molecules or materials capable of metal-to-metal charge transfer (MMCT) to drive thermodynamically unfavorable reactions. Intense coloration in inorganic complexes and solid-state materials containing different metals has been observed for hundreds of years.¹⁷ This phenomenon has been attributed to the transfer of an electron from one metal center to another, usually of a different oxidation state. One of the most famous examples of this electron transfer is observed in Prussian blue, which contains both an Fe^{2+} and Fe^{3+} metal center ligated and bridged by cyanide ligands. The intense blue color of this pigment upon light absorption has been attributed to the electron transfer from Fe^{2+} to Fe^{3+} . Observation of this chromophore and others like it has led researchers to study its mechanism and potential applications.¹⁸

1.3 Metal-to-Metal Charge Transfer in Molecules and on Surfaces

Although MMCT has been observed for many years, it was not until the early 21st century when it started to be looked at as a chromophore of interest for light-harvesting applications. In 2005, Lin and coworkers published their findings on a new series of heterometallic materials where transition metals were covalently linked through oxido-bridges on a mesoporous silica surface.^{19,20} In their article, the authors described a synthetic technique that introduces Cu^{I} and Ti^{IV} defects on the surface of MCM-41 in sequential synthetic steps, resulting in the formation of $\text{Cu}^{\text{I}}\text{-O-Ti}^{\text{IV}}$ linkages.¹⁹ At the time, covalently linked first row metals on surfaces had not been explored and their utility as photocatalysts had not yet been discovered. In this type of material, the Cu^{I} served as the electron donor metal, an oxygen atom as the bridge, and Ti^{IV} as the electron acceptor. The authors employed diffuse reflectance spectroscopy (DRS) to study the changes in optical activity upon introduction of the various metals on the material. Upon overlaying the independently modified Cu^{I} -MCM-41 surface with the $\text{Ti}^{\text{IV}}\text{Cu}^{\text{I}}$ -MCM-41 material, a spectral difference could be taken to deconvolute the combined spectra to reveal new features once the donor-bridge-acceptor linkages were formed. This difference revealed a new absorption feature in the UV-Vis region and assigned this broad absorption to a MMCT, resulting in the generation of a transient $\text{Cu}^{\text{II}}\text{-O-Ti}^{\text{III}}$ species. Further assignment of the transient Ti^{III} species

was confirmed through electron paramagnetic resonance (EPR) measurements following UV-Vis excitation.

Following their demonstration of MMCT in these transition metal/mesoporous silica materials, Frei and coworkers expanded their scope of targeted transition metals for these heterometallic linkages.²¹⁻²⁴ One of these examples includes one of the first published cases of photoreduction of a substrate following excitation of a MMCT chromophore in either a solid-state material or molecule in solution.²⁰ This particular example substituted Zr^{IV} centers for the Ti^{IV} in the previously discussed example, but kept Cu^{I} as the electron donor. Zr^{IV} offers a few advantages over Ti^{IV} . One of which is the substitution of Zirconium for Titanium that shifts the MMCT due to the varied electronegativity difference between the donor and acceptor metals. Due to the increased availability of lower wavelength photons from the sun, the optimized energy required for MMCT would utilize these lower-energy wavelengths.

A few years later, Cuk and coworkers were able to continue the advancements of these oxido-bridged heterobimetallic materials containing first row transition metals, and were able to obtain the excited state lifetimes and transient absorption features for the first time.²⁵ These $\text{Mn}^{\text{II}}\text{-O-Ti}^{\text{IV}}$ containing materials exhibited an excited state lifetime of 1.8 μs at room temperature which remained consistent (within experimental error) upon varying the excitation wavelength. At the time of publication literature precedence for lifetimes on this scale in inorganic materials and even more specifically, metal-to-metal charge transfer, were not present. Recently, McClure and coworkers published their extensive investigation of a similar oxido-bridged $\text{Mn}^{\text{II}}\text{-O-Ti}^{\text{IV}}$ chromophore and proposed various relaxation mechanisms en route to a 2.4 μs excited state lifetime.²⁶

Published examples of solution-phase, molecular examples of MMCT are few and far between, but there are a few examples that have set precedence for others to follow. One attempt to characterize electron transfer between metal centers in solution was demonstrated by Reid and coworkers.²⁷ The MMCT in these cyano-bridged mixed valence complexes containing Ru^{II} and Ru^{III} metal centers exhibited femtosecond excited state lifetimes at an excitation wavelength of 895 nm in aqueous media. The short lifetime in these molecules can be attributed to the lack of an excited-state stabilizing ligand environment, and relaxation

mechanism, which relies heavily on solvent rearrangement. The latter of which was revealed through a kinetic-isotope effect, resulting in a significant lifetime lengthening upon deuterium substitution.

Wagenknecht and coworkers at Furman University have published an interesting set of examples of MMCT in organic solution. Their initial work sought to investigate Ti^{IV} as an electron acceptor in D- π -A type molecules, employing a Cp-derived ligand environment

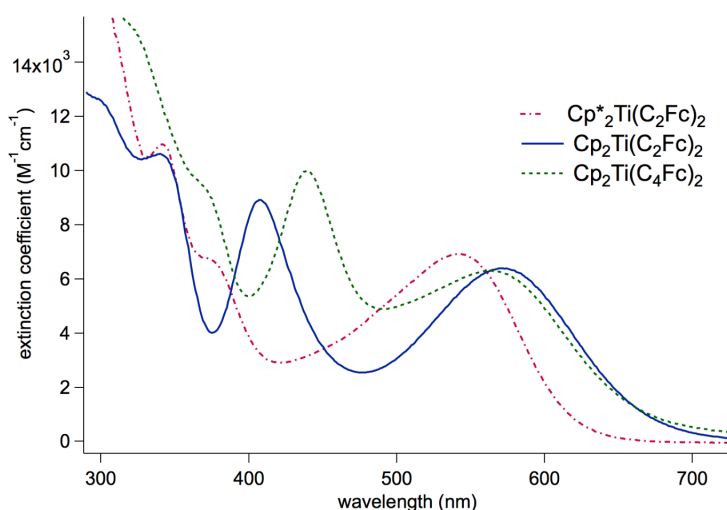


Figure 1.5 Reported EAS of various alkynyl-bridged Titanocene/Ferrocene complexes with a broad MMCT in the visible region.³⁰

around the acceptor metal.²⁸ It was discovered that these new molecules exhibited intense charge transfer (LMCT) in the visible region where the electron originates from a DMA (N,N-dimethylaniline) functional group in the molecule. These discoveries lead to their most recent paper that describes MMCT in an analogous complex.²⁹ In this follow-up paper the authors substituted Ferrocene for the DMA functional group while conserving the alkynyl bridge, and discovered that the Fe^{II} center was now the electron donor. The charge transfer intensity decreased upon donor substitution, however its role as a potential photosensitizer for TiO_2 injection following MMCT is conserved ($\epsilon \approx 10^3$). Although the MMCT in these complexes are in a favorable region of the UV-Vis spectrum at 575 nm (**Figure 1.5**), the charge-separated excited state lifetime leaves much to be desired (picosecond lifetimes). TD-DFT calculations on these complexes confirmed the HOMO assignment as having a large

Ferrocene contribution and the LUMO largely being localized on the Titanocene (**Figure 1.6**). Despite their spectroscopically observed lifetimes, they do exhibit reversible redox characteristics. Ferrocene's reversible redox behavior in organic solution has been studied extensively and is the literature standard for reporting $E^{1/2}$ potentials. The important take-away from Wagenknecht and coworkers' findings is the observed reversible redox behavior of the $Ti^{IV/III}$ couple throughout repeated electrochemical measurements and photoexcitations.

Recent findings by Wu and coworkers describe a $V^{IV}-O-Fe^{II}$ to V^V-O-Fe^I MMCT in a datively bonded heterobimetallic complex that has both favorable energetic requirements for charge transfer and observed excited state lifetime.³⁰ Unpublished work by Wu has revealed

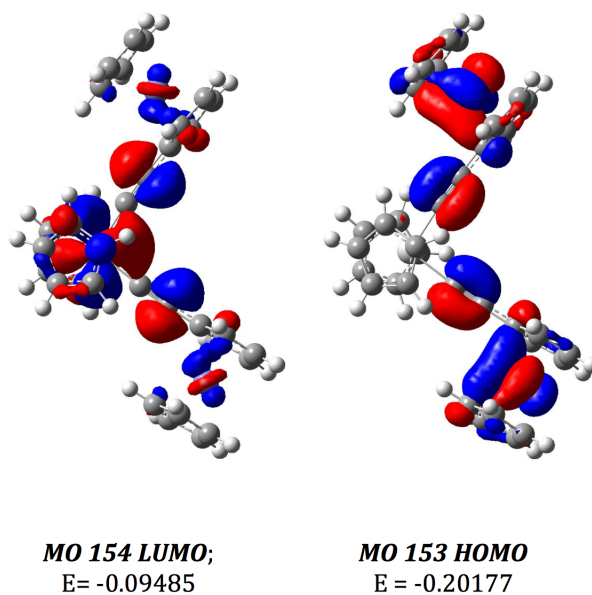


Figure 1.6 HOMO/LUMO Calculations of Heterobimetallic Molecules by Wagenknecht and coworkers

a \approx 1.0 nanosecond excited state lifetime in organic solution for this type of chromophore and is one of the first examples of a first row transition metal complex to exhibit a lifetime of this magnitude.

1.4 Electronic Coupling: An Introduction to Selection Rules, Franck-Condon, and Marcus Theory

Electronic coupling between two systems can result in either electron transfer or energy transfer. To determine the degree of electronic coupling between two systems, the most common tool implemented is electronic absorption spectroscopy (EAS). The observed spectrum represents the electronic transitions present between molecular and/or atomic orbitals. Selection rules play a vital role in experimentally observed intensities of electronic transition, in that the more forbidden a transition is, the weaker the intensity. The aforementioned intensity of an electronic absorption band in an EAS is represented by its molar absorptivity, or ϵ , with units of $M^{-1}cm^{-1}$. To determine how “allowed” a particular electronic transition is, it is worthwhile to discuss the orbitals involved in the transition of interest and the selection rules that govern them. The following section aims to introduce selection rules present in electronic transitions with a brief discussion of their characteristics.

Quantum mechanics defines the allowedness of an electronic transition between two orbitals as the value of the transition moment integral. This integral is reliant upon the wavefunction of each orbital involved in the transition, in addition to the transition moment operator (**Equation 1.1**). This is otherwise known as the electronic dipole operator, which is

$$\textbf{Equation 1.1} \int \Psi_1 | \mu | \Psi_2 d\tau$$

a function of the nuclear and electronic coordinates of the orbitals of interest. For an electronic transition, the dipole operator transforms as the Cartesian coordinates (x, y, z). This operator is a vector quantity that is associated with the initial and final states of the transition whose direction determines how the orbitals will interact with a polarized electromagnetic field.³¹ It is important to note even if the transition transforms as a Cartesian coordinate, its transition intensity may still be zero. Electronic transitions between orthogonal

orbitals do not have any overlap; therefore the value of the integral will be zero leading to the absence of an observed transition.

The first selection rule involved in a transition that will be elaborated upon is the orbital selection rule, otherwise known as the Laporte rule. This rule states in order to be a Laporte or orbitally allowed transition, there must be a change in parity between the initial and final states.³² In order to change parity, the sign of a single spatial coordinate must change during the transition. A more practical analysis of the Laporte rule involves the comparison of orbitals and their centrosymmetric characteristics. Laporte allowed transitions result from the transition of an electron originating from an orbital which has opposite centrosymmetric characteristics from its destined orbital. For an orbital to be characterized as gerade, it must contain an element of symmetry with respect to an inversion center (i.e. a 3d orbital). Opposite that of orbitals characterized as gerade are ungerade, in that they do not contain a symmetry element in relation to an inversion center (i.e. a 2p orbital). In other words, an electron of gerade origin must transition to an orbital that contains ungerade characteristics. Transitions between ungerade and gerade orbitals ($\Gamma_g \otimes \Gamma_u$) often transform as either a single Cartesian coordinate or combination of them. This resulting Cartesian coordinate transformation reveals the polarization involved in the electronic transition of interest. It is also important to know that electronic transitions that are Laporte forbidden can still be observed in electronic spectroscopy, albeit very weak in intensity. These transitions are able to gain intensity through vibronic coupling, which in turn makes them vibronically allowed. When vibronic coupling occurs, typically the $v=0 \rightarrow v'=0$ is not observed. But rather the energy for the vibronically allowed transition is located at an energy of the v_{0-0} band plus one quanta of vibrational energy ($T_g \otimes \Gamma_{vib} \otimes T_g$). In order for this transition to gain intensity through vibronic coupling, it must contain the totally symmetric irrep, a_1 . Vibronically allowed transitions are not limited to orbitally forbidden transitions, they may also be present in Laporte allowed transitions. Examples of such transitions are d-d bands in transition metal complexes, which can be observed through increasing the concentration of the EAS sample or by employing a more advanced spectroscopic method such as magnetic circular dichroism (MCD).

Another selection rule that dictates the intensity of an electronic transition involves spin. In order for an electronic transition to be spin allowed, it must conserve multiplicity in that ΔS must equal zero. For example, for an electronic transition from a ground singlet state (1S_0), the initially generated excited state must also be a singlet in nature (1S_1). This is a fairly significant selection rule in that transitions that disobey spin selection rules are generally not observed. However, spin selection rules can be relaxed with the introduction of spin-orbit coupling. Spin-orbit coupling is the interaction of a nuclei's motion with its spin. Just like in the previous example of the transition dipole operator transforming as Cartesian coordinates as seen in a character table the spin-orbit operator, $\lambda L \cdot S$, transforms as rotations in 3D space (R_x , R_y , and R_z). The magnitude of spin-orbit coupling is proportional to what is known as a spin-orbit coupling constant, SOC. These values have been experimentally measured and theoretically calculated for various nuclei, namely transition metals in their various oxidation states. The SOC are usually directly proportional to atomic number, and also the metal's

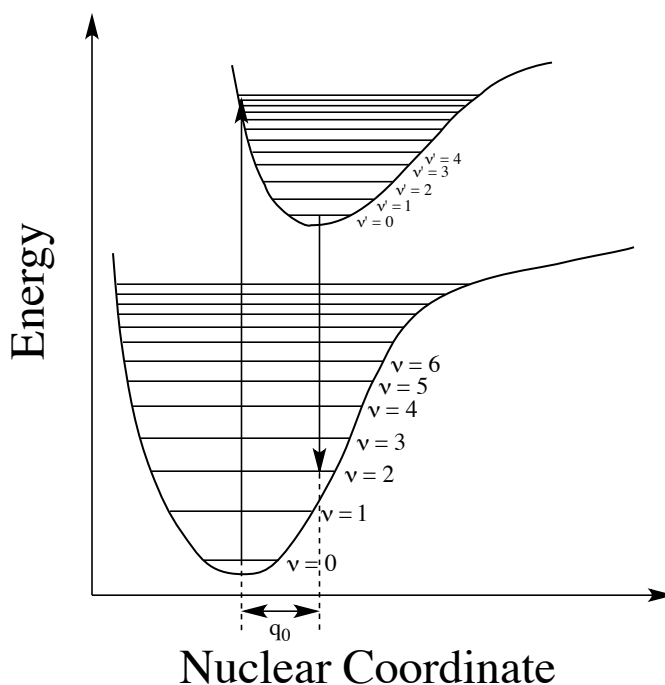


Figure 1.7 Classic potential well diagram predicting the initially generated excited state sans nuclear motion as governed by the Franck-Condon Factor.

nuclear charge, however this is not always the case. Nevertheless, SOCs for large 2nd and 3rd row transition metals are significantly larger than those of 1st row metals, with significant trends observed when proceeding down a group of the same oxidation state (ex: Fe^{III} at 460 ζ vs. Ru^{III} at 1180 ζ).³³

Practically speaking, spin-orbit coupling mixes states of different multiplicity to relax the $\Delta S = 0$ selection rule. In an electronic transition, angular momentum is held constant thus this change in spin while relaxing this selection rule is attributed to a change in orbital angular momentum. This change in orbital angular momentum is observed when an electron's motion near a nucleus is accelerated, inducing a small magnetic field. This observation is again manifested in the larger SOCs for larger nuclei with higher oxidation states. The larger this change in orbital angular momentum is, the more mixing between spin states can take place, the more intense these spin-forbidden transitions are.

However important these selection rules are, the underlying principle governing electronic transitions is what is known as the Franck-Condon factor that takes into account the vibrational requirements for electron transfer. Mathematically it can be represented by the overlap of the vibrational wavefunctions of the initial (Ψ_0) and final (Ψ_f) electronic states. This principle states that electronic motion is monumentally faster than nuclear motion, and therefore electronic transitions do not involve changes in nuclear coordinates or momenta. In other words, electronic transitions occur much faster than structural changes do within a molecule, and result in what is called a Franck-Condon state upon excitation. In the ground state at room temperature, a molecule usually exists in the ground vibrational state, in that $v = 0$. Since electronic transitions occur so quickly with respect to structural relaxation, the initially generated excited state may exist in a non-zero vibrational state ($v' \neq 0$).³¹ This is coupled with the fact that the greatest overlap between vibrational wavefunctions typically occur between non-zero vibrational states in the excited conformation. Population of vibrational levels higher than $v = 0$ are possible, and most readily observed at elevated temperatures which can be controlled fairly readily with experimental controls. This introduction of thermal energy will not excite the molecule electronically, however it may result in the observation of new absorption bands that disappear upon cooling the sample to

room temperature. These absorption bands are referred to as hot bands, as they originate from vibrational levels in the ground state that are $v \neq 0$ due to the introduction of thermal energy to access them. The shift in nuclear coordinates between the ground state and initially generated Franck-Condon state is designated in the figure as q_0 . Relaxation to the ground state must occur from the $v' = 0$ state, as seen in the **Figure 1.7**. This absorption of vibrational quanta can also manifest itself in the observation of vibronically allowed transitions, as discussed previously.

Once it has been determined that an electronic transition can occur, it is important to tailor the requirements for and characteristics of the chromophore of interest. In this research I aim to synthesize a new class of molecules which contain a donor-bridge-acceptor framework which are capable of achieving long-lived charge separated excited states capable of electron transfer. To understand the basis of this project it is important to outline the parameters that govern electron transfer, as first described by Marcus and coworkers.^{34, 35}

1.5 Electron Transfer Between Two Systems: Marcus Theory

Now that the requirements for electronic transitions have been presented at length in **Section 1.4** under the guise of selection rules, we can now apply this knowledge to electron transfer phenomena. There are essentially two types of electron transfer that can occur in molecules in solution or in the solid state. One of which is known as inner-sphere electron transfer, or the transfer of an electron from electron donor to acceptor through direct orbital overlap. Typically in a D-B-A type structure, the bridging ligand facilitates electron transfer through a covalent interaction with both the donor and acceptor; while preventing direct overlap between the two redox-active sites. The other type of electron transfer observed in systems is known as outer-sphere electron transfer, which is favored heavily in systems found in nature and is governed largely by Marcus Theory.³⁵ Marcus Theory also describes observations seen in inner sphere electron transfer processes, and will be treated as the model for understanding MMCT.

In the classical Marcus theory approach, it is assumed that the two chemical species that will undergo electron transfer must first be in close enough proximity with one another to allow electronic coupling between the donor and acceptor orbitals. It is also assumed to

follow the Franck-Condon principle previously mentioned, electron transfer occurs much faster than changes in nuclear coordinates can occur. With this understanding, it can be reasonably assumed that electron transfer will occur at the intersection of the initial and final states' potential wells. This combination of Marcus' theory and the Franck-Condon principle means that at the instantaneous moment of electron transfer, the initial and final states share common nuclear coordinates, position q_{DA} in **Figure 1.8**. This depicts the classic potential well overlay of the initial and final states as described by Marcus. The variable $q_{0, D}$ represents the nuclear coordinate of the electron localized in the donor orbital prior to electron transfer. In addition to this, the variable $q_{0, A}$ depicts the location of the acceptor orbital prior to electron transfer. This orbital may be vacant or occupied, however after the elaboration on selection rules in electronic transitions in an earlier section the probability of an electron violating these is extremely low. The distance dependence on electron transfer finds itself integrated into the electronic coupling constant, H_{AB} , which will be discussed at length shortly.

Let us now describe another important variable when thinking about electron transfer between two systems, which takes into account relaxation pathways both in the inner and outer spheres, λ . The reorganization term λ in **Figure 1.8** can be broken down into its two components, λ_I and λ_O . **Equation 1.2** breaks down the inner-sphere component to the reorganization energy, λ_I .³⁴ f_j^r represents the j^{th} force constant present in the initial electronic state and f_j^p represents the same in the final state after electron transfer. Δq_j represents the change in equilibrium position of the j^{th} nuclear coordinate. For simplicities sake, the

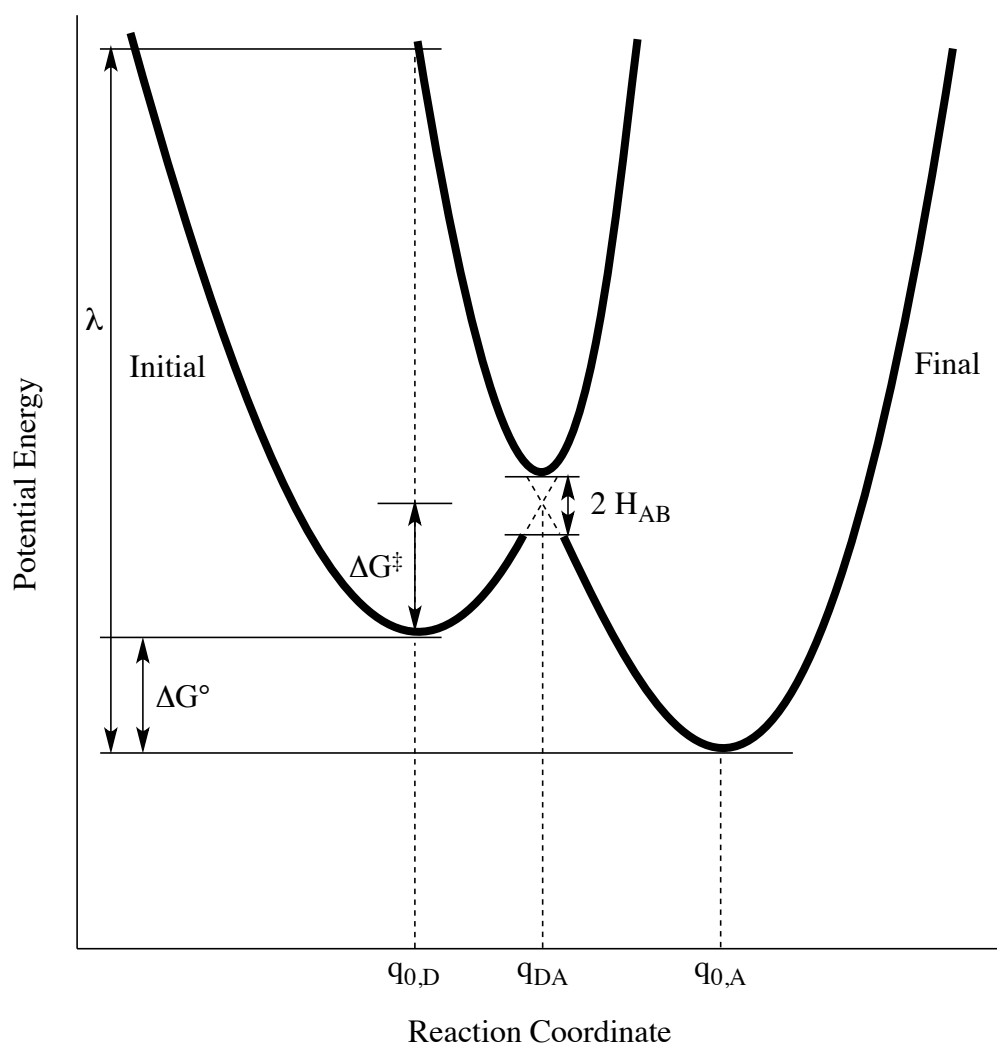


Figure 1.8 Potential energy curves of the Initial Electronic State (Electron Donor) and Final Electronic State (Electron Acceptor), which represents an electron transfer event as described by Marcus

vibrations in both the initial and final states were treated as classic harmonic oscillators.

$$\textbf{Equation 1.2 } \lambda_I = \sum_j \frac{f_j^r f_j^p}{f_j^r + f_j^p} (\Delta q_j)^2$$

In addition to the inner sphere reorganization energy, there is also an outer sphere component that takes into account solvent and distances of the donor and acceptor. For an electron transfer involving an outer sphere component, **Equation 1.3** describes the components of such a process.

$$\textbf{Equation 1.3 } \lambda_O = (\Delta e)^2 \left[\frac{1}{2a_1} + \frac{1}{2a_2} - \frac{1}{r} \right] \left[\frac{1}{D_{OP}} - \frac{1}{D_S} \right]$$

The amount of charge transferred from donor to acceptor is represented by the Δe term and can be measured experimentally. The a_1 and a_2 variables represent the physical radii of both the donor and acceptor respectively, and assume a spherical orientation of the two components. The “ r ” term is representative of the equilibrium distance between the two centers of the nuclei, and can be described as the physical distance between the two orbitals. And finally, the second bracket is representative of outer sphere solvent effects. Unlike the inner sphere components to reorganization energy, the solvent effects are not treated as harmonic oscillators but rather are linearly dependent on changes in electronic charge. The D_{OP} component is representative of the optical dielectric constant of the solvent and can be thought of as the refractive index squared. In other words, D_{OP} is the dielectric constant of the solvent upon introduction of irradiation. D_S on the other hand takes into account the static dielectric constant of the solvent. When the difference of D_S and D_{OP} is equal to zero, the outer sphere component of the electron transfer process essentially does not contain a dipole moment, be it local or global. When this occurs, the solvent is considered non-polar and the reorganization term λ_O is considered zero.

Another key component of Marcus theory is the thermodynamic term, ΔG^\ddagger . This is representative of the energetic requirement to overcome the barrier of electron transfer between the initial and final states. This term takes into account both the inner and outer sphere reorganization energies, λ , in addition to the differences in potential energies of the initial and final states. The closer in energy these two states are, the less energetically

demanding the electron transfer process will be and will result in a smaller ΔG^\ddagger . This term is now rearranged as depicted in **Equation 1.4**.

$$\mathbf{Equation\ 1.4}\ \Delta G^\ddagger = \frac{(\lambda_0 + \Delta G^0)}{4\lambda_0}$$

The variable ΔG^0 is representative of the Gibbs free energy of reaction in the electron transfer process, or the activation energy requirements plus a modest overpotential factor independent of reorganization parameters. Classic thermodynamics reveals the more negative the Gibbs free energy difference is, the more spontaneous the chemical process is. In the case of electron transfer, this would lead to the assumption that the rate of electron transfer will increase with a more negative ΔG^0 . This turns out not to hold true, and manifests itself in the Marcus inverted region.³⁴ As ΔG^* initially decreases, the rate of electron transfer does in fact increase. However, as the energy requirements approach those of the reorganization energy, the rate of electron transfer actually decreases. In other words, when $-\Delta G^0 \gg \lambda$, ΔG^* increases leading to the Marcus inverted region phenomenon.

We can now plug all of this information into the electron transfer rate equation, relating the previously discussed variables to the actual rate of electron transfer (**Equation 1.5**). Where is equal to the rate of electron transfer and the newly introduced term, pZ , is representative of the electronic coupling term H_{AB} .³⁶⁻³⁸

$$\mathbf{Equation\ 1.5}\ k = pZe^{\left[-\frac{(\Delta G^0 - \lambda)^2}{4\lambda k_B T}\right]}$$

The magnitude of H_{AB} is represented by the off-diagonal matrix elements in the secular determinant. This electronic coupling term describes the degree of mixing between the initial and final electronic states involved in the electron transfer process and is directly proportional to the rate of the electron transfer.

Expanding the pZ term allows us to obtain the final form of the Marcus equation described in **Equation 1.6**.

$$\mathbf{Equation\ 1.6}\ k_{ET} = \frac{2\pi}{h} |H_{AB}|^2 \frac{1}{\sqrt{4\pi\lambda k_B T}} e^{\left(-\frac{(\lambda + \Delta G^0)^2}{4\lambda k_B T}\right)}$$

This relationship of the rate of electron transfer to the variables discussed earlier is extremely useful when describing both inner and outer sphere electron transfer processes.

The only additional information that is useful to point out is that there is a Boltzmann distribution in the population of vibrational states in both the initial and final electronic states. Again, this can be thought of in a Franck-Condon sense in that the most probable vibrational state populated initially is the $v = 0$ state, and due to the presence of modest overpotential after electron transfer to the final excited state $v \neq 0$.

1.6 Is it Electron Transfer for Energy Transfer? Distinguishing Between Förster and Dexter Energy Transfer

Once the initially generated excited state is populated, it inherently can undergo two different relaxation mechanisms. The first of which that will be discussed occurs in through-space interactions in systems that do not have any covalent orbital overlap, this is known as Förster Resonance Energy Transfer (FRET). FRET can occur over long distances, in some cases up to 100 Å, and is most prevalent in biological systems.³⁹⁻⁴¹ The initial basis of Förster's mechanism of decay pathway following electron transfer, involved a fluorescence quenching event between two independent molecules in solution. His initial experiments involved the energy transfer from chloroanthracene, which itself has an incredible low fluorescence quantum yield due to internal conversion, to perylene which experience an increase in fluorescence quantum yield with increasing photosensitizer concentration. In FRET, there is essentially coupling of two electronic transitions, the emission of a photon by the photosensitizer and the transfer of this energy to an electron acceptor. For this to occur, there must be sufficient electronic coupling between the donor and acceptor as described previously by Marcus theory and governed by the Franck-Condon principle. **Figure 1.9** depicts a FRET process involving two different molecules in solution as a Jablonski diagram. Förster energy transfer may be either a radiative energy transfer process or it may be radiationless.

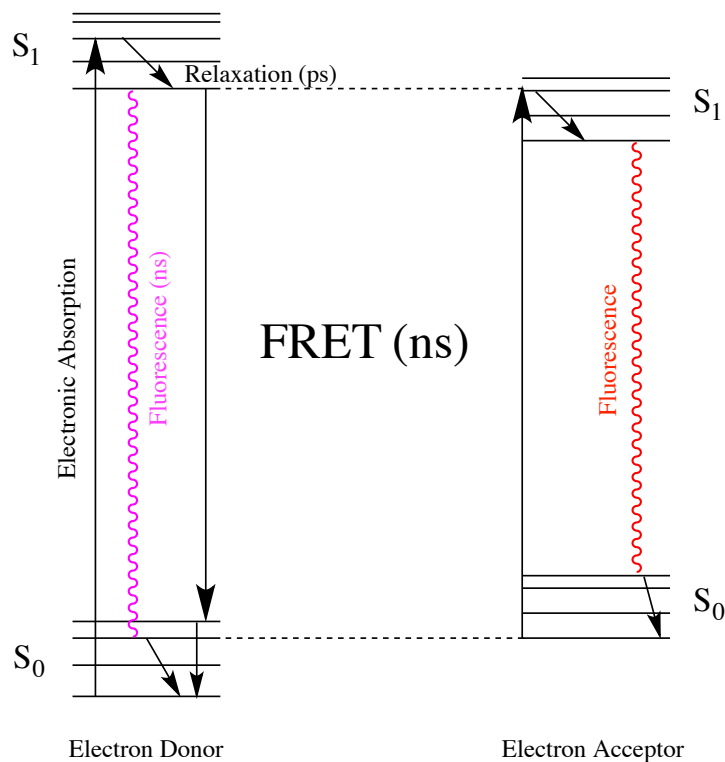


Figure 1.9 Jablonski Diagram depicting a general FRET system with experimentally observed timeframes

There are essentially two pathways for FRET to occur in a donor-acceptor coupled system. In the first, the electron donor absorbs a photon, generating the initially formed singlet state which decays back to the ground state through emission. The electron acceptor then absorbs this photon if the energetic requirements are met for acceptor excitation. This S_1 state of the electron acceptor can then decay either radiatively or through a radiationless pathway. This type of FRET can be studied through quantum yield measurements of both the donor and acceptor, and can be thought of as a fluorescence quenching mechanism. The second possible pathway for FRET involves non-radiative energy transfer from donor to acceptor through a dark pathway. Non-radiative transfer can occur if the donor and acceptor orbitals are sufficiently coupled to one another.

The other type of energy transfer, which can occur in systems that have electronically coupled orbitals, involves a Dexter-type mechanism. The main requirement for Dexter energy transfer is that the donor and acceptor orbitals must have direct orbital overlap, which essentially eliminates the possibility for any multimolecular processes.⁴² In Dexter energy transfer there also exists a much larger distance dependence due to this orbital overlap requirement. It is generally accepted that wavefunctional overlap will only be sufficient for electron transfer if the distance is 10 Å or less. Dexter energy transfer can also be considered when determining fluorescence quenching mechanisms, as any presence of it will decrease the quantum yield of the donor fluorophore. **Figure 1.10** depicts the radiationless electron transfer present in Dexter type systems.

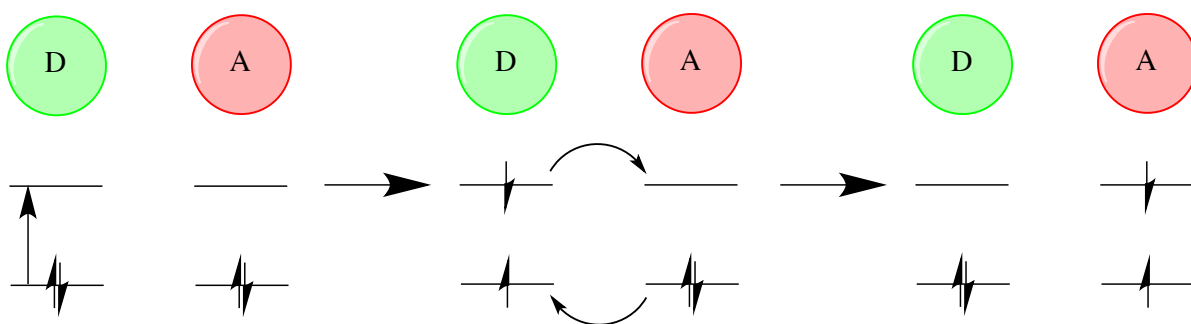


Figure 1.10 Schematic diagram of the radiationless energy transfer between Donor and Acceptor in a Dexter type process

Dexter energy transfer can also be described as an electron exchange process, similar to magnetic exchange coupling, which demands similar requirements in terms of overlap. After excitation, the electron in the S_1 state of the electron donor is then transferred to the electron acceptor. There is then an exchange of an electron from electron acceptor to the initial donor to complete the cycle. The energy transfer occurs in this step, whereby the electron transferred from donor to acceptor is in a higher energy state. The opposite is true for the electron transferred from the acceptor to donor, as it is present in a lower energy state. In molecules that possess direct orbital overlap between donor and acceptor, there exists a higher probability of energy transfer through a Dexter-type mechanism provided that the electronic coupling is sufficient.

1.7 Cited References

- 1) U.S. Energy Information Administration. World Energy Demand and Economic Outlook, Released May 11th 2016. <https://www.eia.gov/outlooks/ieo/world.cfm> (Accessed January 18th 2017)
- 2) Organization for Economic Co-operation and Development: Energy <https://www.oecd.org> (Accessed January 28th 2017)
- 3) Carbon Pollution Emission Guidelines for Existing Stationary Sources: Electric Utility Generating Units, *Federal Register*, **2015**, *80*, 64661-65120
- 4) Shockley, W.; Queisser, H. S. *J. Appl. Phys.* **1961**, *32*, 510
- 5) Barbose, G.; Darghouth, N.; Weaver, S.; Wiser, R. *Tracking the Sun VI*, **2013**, LBNL, 6350
- 6) NREL: Photovoltaic Research <http://www.nrel.gov/pv/> (Accessed January 28th 2017)
- 7) MIT Technology Review. Energy News: Hydrogen Storage Could Be Key to Germany's Energy Plan <http://www.technologyreview.com/news/427360/hydrogen-storage-could-be-key-to-germanys-energy-plans/> (Accessed May 15, 2014)
- 8) The Role of the Chemical Sciences in Finding Alternatives to Critical Resources: A Workshop Summary <https://www.ncbi.nlm.nih.gov/books/NBK100028/> (Accessed January 28, 2017)
- 9) Osterloh, F. E. *ACS Energy Lett.* 2017, *2*, 445-453.
- 10) Shevela, D.; Björn, L. S.; Govindjee. Oxygenic Photosynthesis. Natural and Artificial Photosynthesis: Solar Power as an Energy Source. Razeghifard, R., Ed.; *John Wiley and Sons, Inc.*, **2013**
- 11) Van Mieghem, F. J. E., Satoh, K., and Rutherford, A. W. (1991) *Biochim. Biophys. Acta* *1058*, 379-385
- 12) Govindjee; Kern, J. F.; Messinger, J.; Whitmarsh, J. Photosystem II. Encyclopedia of Life Sciences (ELS) *John Wiley and Sons, Ltd.*, Chichester. **2010**
- 13) Fukuzumi, S.; Ohkubo, K.; Suenobu, T. *Acc. Chem. Res.* 2014, *47*(5), 1455-1464
- 14) Nocera, D. G. *Acc. Chem. Res.* **2012**, *45*, 767
- 15) Kanan, M. W.; Nocera, D. G. *Science* **2008**, *321*, 1072

- 16) Surendranath, Y.; Dincâ, M.; Nocera, D. G. *J. Am. Chem. Soc.* **2009**, *131*, 2615
- 17) Blasse, G. *Struct. Bond.* **1991**, *76*, 154
- 18) Reguera, E. Martin, E.; Calderón, A.; Rodriguez-Hernandez, J. *Spectrochimica Acta Part A: Molecular and Biomolecular Spectroscopy* **2007**, *68(1)*, 191
- 19) Lin, W.; Frei, H. *J. Phys. Chem. B* **2005**, *109*, 4929
- 20) Lin, W.; Frei, H. *J. Am. Chem. Soc.* **2005**, *127*, 1610
- 21) Han, H.; Frei, H. *Microporous Mesoporous Mater.* **2007**, *103*, 265
- 22) Behar, D.; Frei, H.; Macnaughtan, M.; Rabani, J. *J. Phys. Chem. C* **2012**, *116*, 23477
- 23) Lin, W.; Han, H.; Frei, H. *J. Phys. Chem. B* **2004**, *108*, 18269
- 24) Kim, W.; Yuan, G.; McClure, B. A.; Frei, H. *J. Am. Chem. Soc.* **2014**, *136*, 11034
- 25) Cuk, T.; Weare, W. W.; Frei, H. *J. Phys. Chem. C* **2010**, *114*, 9167
- 26) McClure, B. A.; Frei, H. *J. Phys. Chem. C* **2014**, *118*, 11601
- 27) Reid, P. J.; Silva, C.; Barbara, P. F. *J. Phys. Chem.* **1995**, *99*, 2609
- 28) Pienkos, J. A.; Agakidou, A. D.; Trindle, C. O.; Herwald, D. W.; Altun, Z.; Wagenknecht, P. S. *Organometallics*, **2016**, *35*, 2575-2578
- 29) Turlington, M. D.; Pienkos, J. A.; Carlton, E. S.; Wroblewski, K. N.; Meyers, A. R.; Trindle, C. O.; Altun, Z.; Rack, J. J.; Wagenknecht, P. S. *Inorg. Chem.* **2016**, *55*, 2200-2211
- 30) Wu, X.; Huang, T.; Lekich, T. T.; Sommer, R. D.; Weare, W. W. *Inorg. Chem.* **2015**, *54*, 5322-5328
- 31) Harris, D. C.; Bertolucci, M. D. "Symmetry and Spectroscopy: An Introduction to Vibrational and Electronic Spectroscopy." *Dover Publications, Inc.* New York, **1978**.
- 32) Laporte, O.; Meggers, W. F. *J. Opt. Soc. Am.* **1925**, *11*, 459-463
- 33) Shultz, D. A.; Wertz, D. W. "Advanced Inorganic Chemistry II: Applications of Group Theory to Bonding and Spectroscopy." *NC State University.* Raleigh, **2013**.
- 34) Marcus, R. A.; Sutin, N. *Biochimica et Biophysica Acta* **1985**, *811*, 265.
- 35) Marcus, R. A. *J. Phys. Chem.* **1956**, *24*, 966-978
- 36) Sutin, N. *Acc. Chem. Res.* **1968**, *1*, 225 – 231
- 37) Marcus, R. A. *Annu. Rev. Chem. Phys.* **1964**, *15*, 155-196

- 38) Marcus, R. A. *J. Phys. Chem.* **1965**, *43* (2), 679 – 701
- 39) Förster, T. *Discuss. Faraday. Soc.* **1959**, *27*, 7-17
- 40) Van Der Meer, B. W.; Coker, G. I.; Chen, S. Y. *Resonance Energy Theory and Data*;
VCH Publishers: New York, **1994**
- 41) Scholes, G. D. *Ann. Rev. Phys. Chem.* **2003**, *54*, 57-87
- 42) Dexter, D. L. *J. Phys. Chem.* **1953**, *21*(5), 836-850

2 Chapter 2: Synthesis and Ground State Characterization of Terminal Metal Hydroxide Complexes

2.1 Reactivity of Supported and Unsupported Metal Hydroxides

Chemically speaking, there are two different classes of terminal metal hydroxides: supported and unsupported. The term “unsupported hydroxide” in the context means that the functional group lacks a network of hydrogen bonding. Supported metal hydroxides are less relevant to this project and will only be covered briefly. Unsupported metal hydroxides find use both in natural system mimics and synthetic catalysis applications; both will be expanded upon at length in this section. The synthetic building block for targeting oxido-bridge heterobimetallic molecules exploits the protic character of these terminal metal hydroxides and whose metal center serves as the electron donor upon completion.

Supported metal hydroxides are commonly found in the bioinorganic chemistry literature as well as synthetic systems to observe proton coupled electron transfer (PCET). Perhaps the most well known examples are those published by Borovik and coworkers.¹⁻¹³

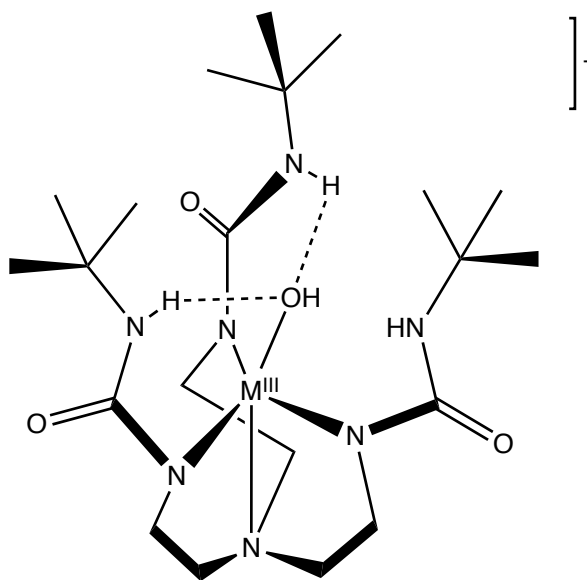


Figure 2.1 Borovik and coworkers’ initial M-OH complexes exhibited trigonal bipyramidal geometry and exhibited modest reactivity¹

These molecules exhibit outer sphere electron transfer through a PCET mechanism. Terminal metal hydroxides in these structural motifs are supported through a network of hydrogen bonding with the ligand environment. Borovik and coworkers initially set out to study these complexes due to their relevance in isolated enzymes from horseradish peroxidase and whose structure resembled the depicted molecules in **Figure 2.1**. Prior to his work, there was one fully characterized monomeric M-OH complex in the literature revealing the critical need to investigate biological mimics of various enzymes. It was later revealed that these hydrogen bonded terminal metal hydroxides were created upon the activation of molecular oxygen by the active enzyme. This activity was largely modulated by the ability of these metal hydroxide complex's ability to control the secondary coordination sphere through the hydrogen bonding network.³ In addition to isolated metal hydroxides for use in studying the activation of oxygen, Borovik and coworkers were also able to synthesize heterobimetallic complexes of these biologically relevant enzyme mimics which contained a hydrogen bonded μ -OH core, which have striking similarities to the OEC in Photosystem II.⁸⁻¹³ These complexes were synthesized in order to study the role of Ca^{2+} throughout the evolution of molecular oxygen by the OEC by way of water oxidation. This natural process has proven to be very difficult to mimic artificially, due to the demanding process of coordinating a 4 electron, 4 proton exchange process. It is important to note, the nature of these hydrogen bonded heterometallic structures with bridging hydroxide cores lack the ability to undergo MMCT. This process requires significant electronic coupling between the two metal centers that is not present in the hydrogen-bonded networks.

On the other hand, terminal metal hydroxides are more analogous to this work and serve as the inspiration for the synthesis of the heterobimetallic design.¹⁴ Using this reactivity of these metal hydroxides enables our synthetic approach for creating this M-O-M' structural motif. The individual metal centers in these bimetallic complexes have been shown by Roesky and coworkers to retain their individual characteristics. However they have also been tuned to exhibit synergistic reactivity.

Harnessing the Brønsted acidic character of the metal hydroxide is characteristic of Roesky's approach for heterobimetallic synthesis from a M-OH perspective. His specific research aim was to design homogeneous catalysts that contain bifunctional reactivity, which had not previously been observed remained to be elucidated. His metal hydroxide precursors followed the structure pattern of LMR(OH), where $L = \text{CH}\{\text{N}(\text{Ar})(\text{CMe})\}_2$; $\text{Ar} = 2,6\text{-}i\text{Pr}_2\text{C}_6\text{H}_3$; $\text{M} = \text{Al}, \text{Ga}, \text{or Ge}$; $\text{R} = \text{alkyl}, \text{aryl}, \text{or a lone pair of electrons}$. In **Figure 2.2**, the metal hydroxides protonate the $\text{N}(\text{SiMe}_3)_2$ leaving group, which act as the Brønsted base.

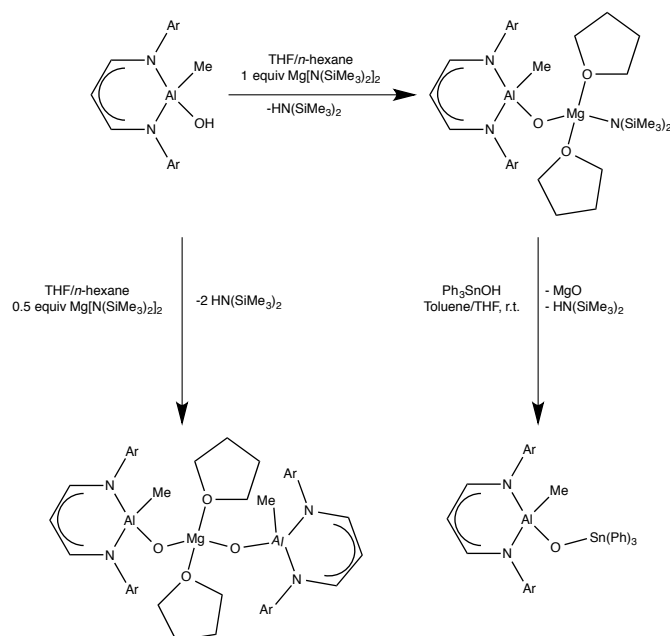


Figure 2.2 Synthesis of various heterometallic molecules by Roesky

This concept of utilizing the acidic character to protonate a basic leaving group to form the heterometallic core of the molecule is exactly what has successfully demonstrated in the complexes presented herein. Compared to the supported metal hydroxides reported by Borovik and coworkers, increased Brønsted acid strength is expected from unsupported metal hydroxides. The molecules synthesized by Roesky and coworkers contain early transition metals such as Zr and Ti, alkali Earth metals such as Mg, main group elements such as Sn and Al, in addition to some lanthanide containing compounds. Each of their heterometallic

complexes that contain transition metals are d^0 systems, which render them unable to undergo MMCT.

Roesky set out to employ this new class of molecules in homogeneous catalysis, namely inspired by the Ziegler-Natta catalyst for use in olefin polymerization. Initial work with the lanthanide-containing heterometallic catalysts investigated the potential to ring open and polymerize lactones.¹⁴ Roesky was able to successfully demonstrate this proof of concept experiment and moved on to more complex mechanisms. In addition to outlining the potential for catalysis in his review paper,¹⁴ Roesky aimed to investigate his findings of the electronic effects the bridging oxygen atom has on electron deficient metal centers, such as Ti^{IV} and Zr^{IV} .¹⁵ NBO analysis revealed the oxygen atom pulled significant amounts of

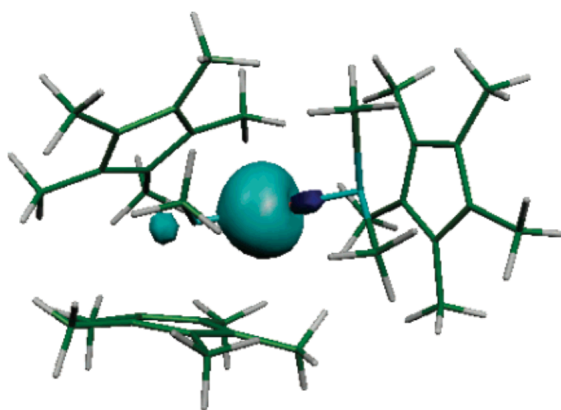


Figure 2.3 NBO analysis of the electronic effects of the bridging oxygen atom has on a Ti^{IV} center¹⁵ electron density away from the metal centers, as anticipated. Consequently this phenomena leaves the metals extremely Lewis acidic and the bridging oxygen atom electron-rich. This finding was to be expected, and is consistent of the MO analysis presented later of the synthesized molecules herein.

Another recent use of molecular terminal metal hydroxides has been to mimic enzymatic activity in synthetic systems, which contain biologically relevant metals such as Manganese and Iron. Stack and coworkers have been able to demonstrate the utility of such complexes employing a polypyridyl ligand set, penned PY5.¹⁶⁻¹⁸ They aimed to synthesize a functional mimic of the naturally occurring lipoxygenase enzyme, which oxygenates unsaturated fatty acids found in various lipids.

2.2 Synthesis of Py₅Me₂ Ligand

When choosing a ligand to coordinate either an electrochemically or photochemically active metal, it is advantageous to choose one that is inert and robust. 2,2'-bipyridine (bpy) is perhaps the most common ligand chosen in the photochemical literature. However, in certain cases it has been shown to lose their bidenticity throughout multiple catalytic cycles. The Py₅Me₂ ligand set is pentadentate, which limits the open coordination sites on the metal center to one. This offers control of where on the metal center catalysis can take place by inhibiting additional competing sites for proton reduction or other chemical processes. Pentadentate ligand sets such as the Py₅Me₂ framework have also been shown to stabilize a wide-range of transition metals with varying oxidation states, such as M^{II}, M^{III} and M^{IV}.¹⁹⁻²³ Chang, Long, and coworkers have shown that Mo^{IV} and Co^{II} based catalysts with a polypyridyl-based ligand set can be implemented to drive proton reduction electrochemically.^{19-21, 23} The redox tunability of the M^{II/III} couple using this ligand set has also been shown to be possible through various ligand modifications. Substituting either electron withdrawing or donating groups on the axial pyridine ring can vary the metal's redox potential varied by as much as 310 mV. This ligand modification inductively affects the electron density in the occupied aromatic pyridine ligand orbitals. Whereby these modifications effectively take away (CF₃) or donate (NMe₂) electron density from the metal center. These redox effects are relatively small, as the ligand modifications do not directly affect the position metal d-orbitals energetically, but are more of a second order effect. The Py₅Me₂ ligand environment has served as the targeted ligand environment for synthesizing these unsupported terminal M^{III} hydroxides.

The first synthetic step in the preparation of the Py₅Me₂ ligand is to perform an ortho-lithiation on the 2-ethylpyridine in THF at low temperature (**Figure 2.4**). The initial preparation of this molecule was reported by Canty et. al and modified by Chang et al.²⁴ Using a dry ice acetone bath offers control of the exothermicity of the addition of an alkyl lithium reagent, in addition to stabilizing the reactive intermediate prior to the 2-fluoropyridine addition. Vacuum distillation at an elevated temperature following the aqueous quenching step is necessary to remove the pure 1,1-bis(2-pyridyl)ethane from

polymerized pyridines generated throughout the reflux period. Detailed experimental information is included at the end of this chapter. The second and final step of synthesizing the pentacoordinate ligand involves the ortho-lithiation of the previously purified 1,1-bis(2-pyridyl)ethane, and reaction with another halogenated pyridine, 2,6-difluoropyridine, followed by another refluxing period and aqueous workup (**Figure 2.4**).

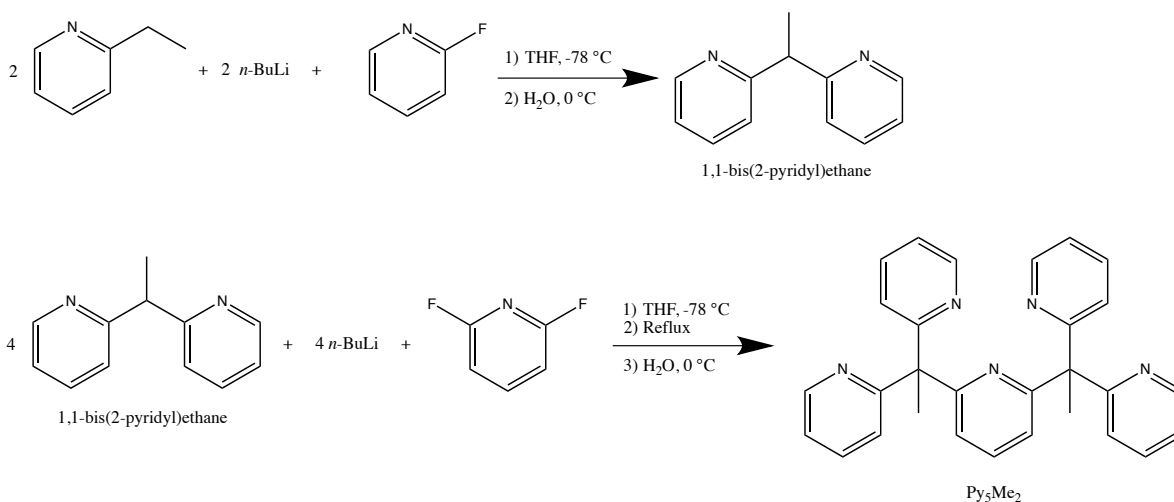


Figure 2.4 Synthesis of Py₅Me₂ starting from 2-ethylpyridine

Purification of the final Py₅Me₂ product involves repeated recrystallizations by dissolving the solid in dichloromethane and layering with cold pentane. This isolated polypyridyl molecule displays two absorption features in the EAS, both fairly high in energy (263 nm and 257 nm). These two absorption bands do not display noticeable solvatochromism, which is indicative of lacking charge transfer bands. The measured ϵ of 42262 and 42026 ($M^{-1}cm^{-1}$) also support the assignment of these bands to either $\pi \rightarrow \pi^*$ or $n \rightarrow \pi^*$ transitions.

2.3 Syntheses and Bonding Analysis of the Electron Donor Source: Unsupported Terminal Metal Hydroxides

Creating a synthetic system to mimic artificial photosynthesis is a daunting task, which has yet to be completely elucidated. Ideally, the design of such a molecular system would contain both the photosensitizer and photocatalyst. This molecule would contain both the electron donor and acceptor within close proximity to one another, and possess an excited

state lifetime long enough to drive an external chemical reaction. The method of such a strategy harnesses the Brønsted acidic character of M^{III} hydroxides to react with a Ti^{IV} molecule containing an alkoxide leaving group, to form the heterobimetallic complex.²⁵ This results in the formation of a complex with an oxido-bridged M^{III} -O- Ti^{IV} type of structure. The oxido-bridged heterobimetallic motif has been chosen due to their potential to drive

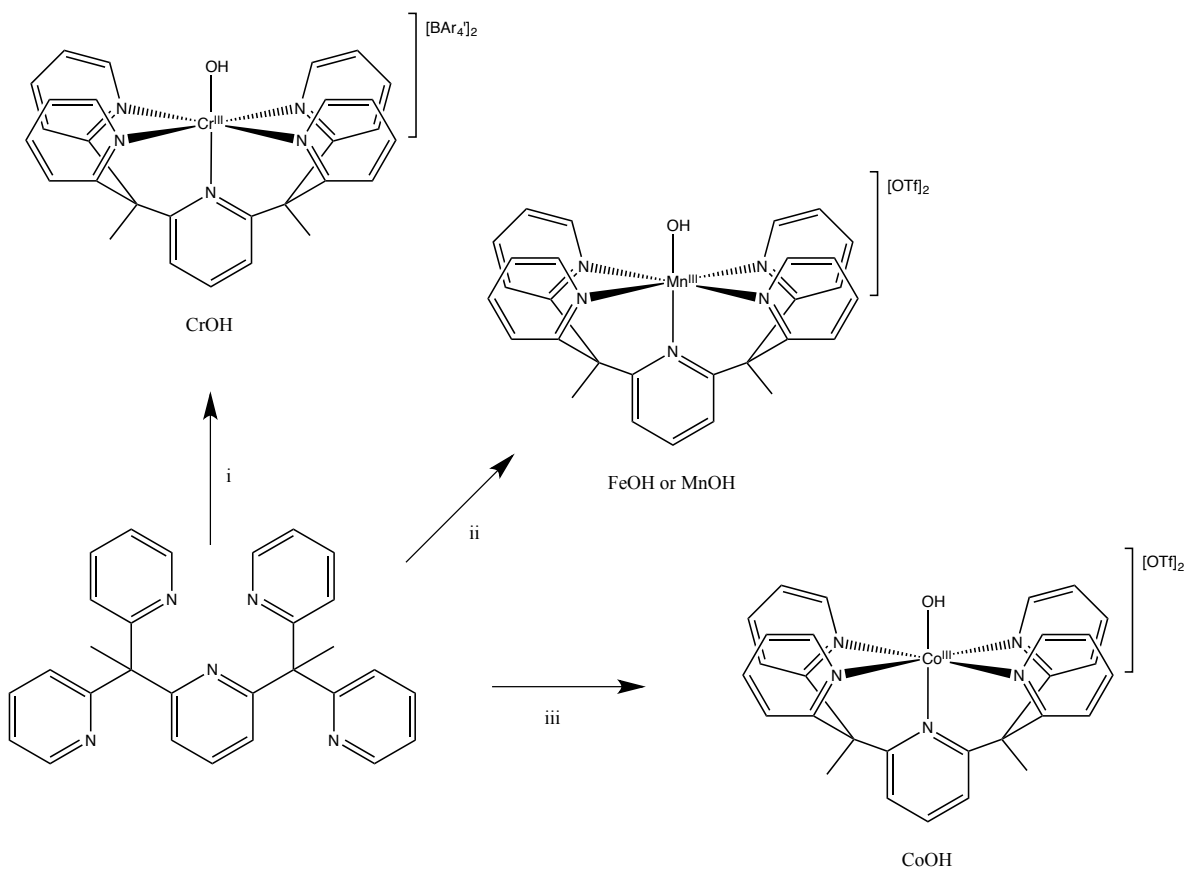


Figure 2.5 (i) Anhyd. $CrCl_2$, MeCN, 72h followed by H_2O and anion exchange with $[BAR_4]^+$. (ii) $Fe(MeCN)_2(OTf)_2$, or $Mn(MeCN)_2(OTf)_2$ MeCN, 12h, followed by iodosobenzene oxidation, 2h. (iii) $Co(MeCN)_2(OTf)_2$, MeCN, 12h, followed by H_2O and aerobic oxidation, 48h.

chemical processes using incident light on silica surfaces.²⁶⁻³⁵ Designing molecules that retain this interaction between donor and acceptor, and studied in solution offers many advantages over traditional surface studies as seen in Frei's extensive work.²⁶⁻³⁶ Solution-based spectroscopic experiments on the MMCT chromophore offer enhanced resolution and increased detection limits, which can be limited for heterobimetallic structures on

surfaces.^{35, 36}

The molecules in herein undergo a tunable MMCT in the ultraviolet and/or visible region of the electromagnetic spectrum, with an extinction coefficient indicative of significant electronic coupling between the donor and acceptor metal centers. The energetics optimization of the induced MMCT is achieved through the substitution of a different electron donor, but can also be achieved through ligand modification.¹⁹ Targeted metals for use in these terminal metal hydroxide complexes must be single-electron redox active, in addition to being stabilized in the M^{III} oxidation state by the chosen polypyridyl ligand set. This fact has prevented the scientific community from targeting Ti, V, Cu, Ni and Zn based complexes for use in the M^{III} -O-Ti^{IV} motif, although recently Chang and coworkers have characterized a transient V^{III} -OH complex using the Py_5Me_2 ligand set.²²

Figure 2.5 depicts the general synthetic approach for all synthesized M^{III} -OH complexes. The first complex which will be discussed at length is $[CrOH(Py_5Me_2)][BAR_4']_2$ (CrOH) and will serve as the benchmark for all comparisons. The chelation of $CrCl_2$ with the Py_5Me_2 ligand initially yields $[(Py_5Me_2)CrCl][Cl]$, an uncharacterized intermediate en route to the formation of $[(Py_5Me_2)CrOH][Cl]_2$, via oxidation by water. Replacement of chloride counter ions with tetrakis[3,5-bis(trifluoromethyl)phenyl]borate (BAR_4') anions results in the formation of the isolated product CrOH. Replacing the counter ion with the non-coordinating BAR_4' gives coordination complexes the ability to dissolve in most organic solvents. Whereas complexes with smaller anions such as chloride have their solubility limited to solvents with high dielectric constants such as water or acetonitrile. In addition to the observed solubility properties of complexes with BAR_4' anions, halides can also be redox active, which may inhibit their use in subsequent synthetic steps and photophysical measurements and applications. In order to test the lability of the terminal hydroxide ligand, the hydroxide ligand was displaced with chloride upon reaction with TMS-Cl, which resulted in the formation of $[CrCl(Py_5Me_2)][BAR_4']$ (CrCl). This molecule will not be discussed in further detail due to its lack of reactivity and its inability to form oxido-bridged molecules. This synthetic step and isolation of the CrCl derivative was important to confirm the aforementioned lability of the hydroxide ligand in addition to the accessibility of this

coordination site for future reactivity studies. The presence of this terminal hydroxide was confirmed by treatment of crude $[\text{CrCl}(\text{Py}_5\text{Me}_2)]^{1+}$ with D_2O . ($\nu_{\text{OD}} = 2690 \text{ cm}^{-1}$ vs. $\nu_{\text{OH}} = 3646 \text{ cm}^{-1}$). In addition to confirming the presence of the terminal hydroxide ligand, this synthetic step was necessary to rule out aerobic oxidative addition or any other potential oxygen contamination source. The relatively weak intensity of the O-H ligand stretching frequency is consistent with previous work reported by Stack.¹⁶ The weak absorption intensity of the hydroxide stretch (**Figure 2.6**) is attributed to the lack of polarization of the O-H bond due to the proximity of the Cr^{III} center. In addition to the decreased intensity of the band, lack of peak broadening is accredited to the lack of intermolecular hydrogen bonding between terminal metal hydroxides in addition to other molecules which exhibit hydrogen bonding such as water.

Unlike the synthesis of CrOH , the Fe and Mn polypyridyl complexes use utilize a triflate precursor in $[\text{M}(\text{ACN})_2(\text{OTf})_2]$ prepared from either anhydrous FeCl_2 or MnCl_2 and trifluoromethanesulfonic acid in acetonitrile. The oxidation of Fe^{II} and Mn^{III} to the

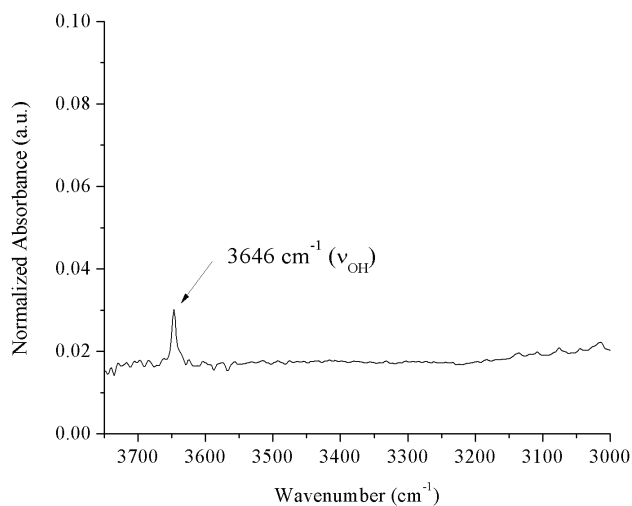


Figure 2.6 ATR-IR spectrum of CrOH taken under inert conditions

corresponding hydroxides is a more thermodynamically demanding process, requiring iodobenzene as a stoichiometric oxidant, which yields the product. An undesirable subsequent one-electron oxidation of Fe^{III} and Mn^{III} is possible using this synthetic pathway,

and requires careful stoichiometric control throughout the reaction. This procedure is covered expanded upon in the experimental section. The FeOH complex has been isolated and fully characterized. The MnOH analog remains elusive and efforts to characterize it are in progress.

Synthesis of the cobalt derivative $[(\text{CoOH}(\text{Py}_5\text{Me}_2))][\text{OTf}]_2$, CoOH, was performed using the same synthetic coordination strategy as employed for MnOH and FeOH. Chang and coworkers first reported this synthetic route for the formation of various catalytically active Co^{II} complexes.¹⁹ The oxidation of the Co^{II} to Co^{III} was performed aerobically in the presence of water. Using triflate as a counter anion has been shown to remain electrochemically inert throughout many catalytic cycles, lending it useful for future photochemical applications.¹⁹

Table 2.1 Measured ν_{OH} stretching frequencies

Complex	$\nu_{\text{OH}} (\text{cm}^{-1})$
CrOH	3646
MnOH	3599
FeOH	3535
CoOH	3521

In order to identify a trend in the assigned ν_{OH} bands, employing FTIR as the tool was necessary. The information obtained provides insight into the potential reactivity of the hydroxide ligand itself for heterobimetallic formation. **Table 2.1** displays the different ν_{OH} stretching frequencies of all three terminal metal hydroxides synthesized. The trend of decreasing frequency of the ν_{OH} mode can be seen as the metal center becomes more electron rich. All three metal ions exist as M^{III} , which eliminates the effect of different oxidation states as the contributing factor to this trend. The difference in stretching frequency can be attributed to the interaction between the metal center and oxygen atom, explained through the relative Lewis acidity of the metal center. Cr^{III} is the most electron deficient metal, leading it to be the weakest electron donor of the three metals. Conversely, Co^{III} is the most electron rich, thus is the best candidate for electron density donation to the hydroxide ligand's σ^*

orbital. This donation of electron density into antibonding molecular orbitals localized on the hydroxide ligand will weaken the σ interaction between the oxygen p_z orbital and hydrogen $1s$ orbital. Population of the hydroxide ligand antibonding orbitals occurs due to both the bonding and non-bonding orbitals being occupied between the oxygen and hydrogen atom. The result of this weakening of the O-H bond thus manifests itself in the decreasing stretching frequency moving across the periodic table from CrOH to CoOH. As a result, it may be stated that the Cr^{III} -OH interaction is the weakest. This observation results in the strongest O-H bond in the series, thereby potentially limiting the protic character of this unsupported terminal hydroxide. As seen in **Chapter 3**, the O-H bond in CrOH is the strongest; there is no observable inhibition of heterobimetallic formation and inhibition of

Brønsted acidity. Analysis of the CrOH complex by Evans' method confirmed the hypothesis of a nominally octahedral Cr^{III} center exhibiting a high-spin ground spin state of $S = 3/2$ ($\mu_{\text{eff}} = 3.42_{\text{BM}}$). Due to the spin stabilization effects and population of the t_{2g} set of bonding orbitals, this is the preferred state for octahedral d^3 first row metals. In order to comprehend the bonding present in the $M^{\text{III}}\text{OH}$ complexes, a group theory approach using molecular orbitals was employed. In order to develop an understanding of the bonding in these complexes, a ML_5O model complex has been simplified to exhibit bond angles present in pure O_h molecules and has been assigned C_{4v} symmetry. Both the π and σ frameworks have been taken into consideration in the ML_5O MO depicted in **Figure 2.7**. The σ framework irreps transform as $3a_1 + b_1 + e$, whereby the L_5 fragment and O fragment have been treated

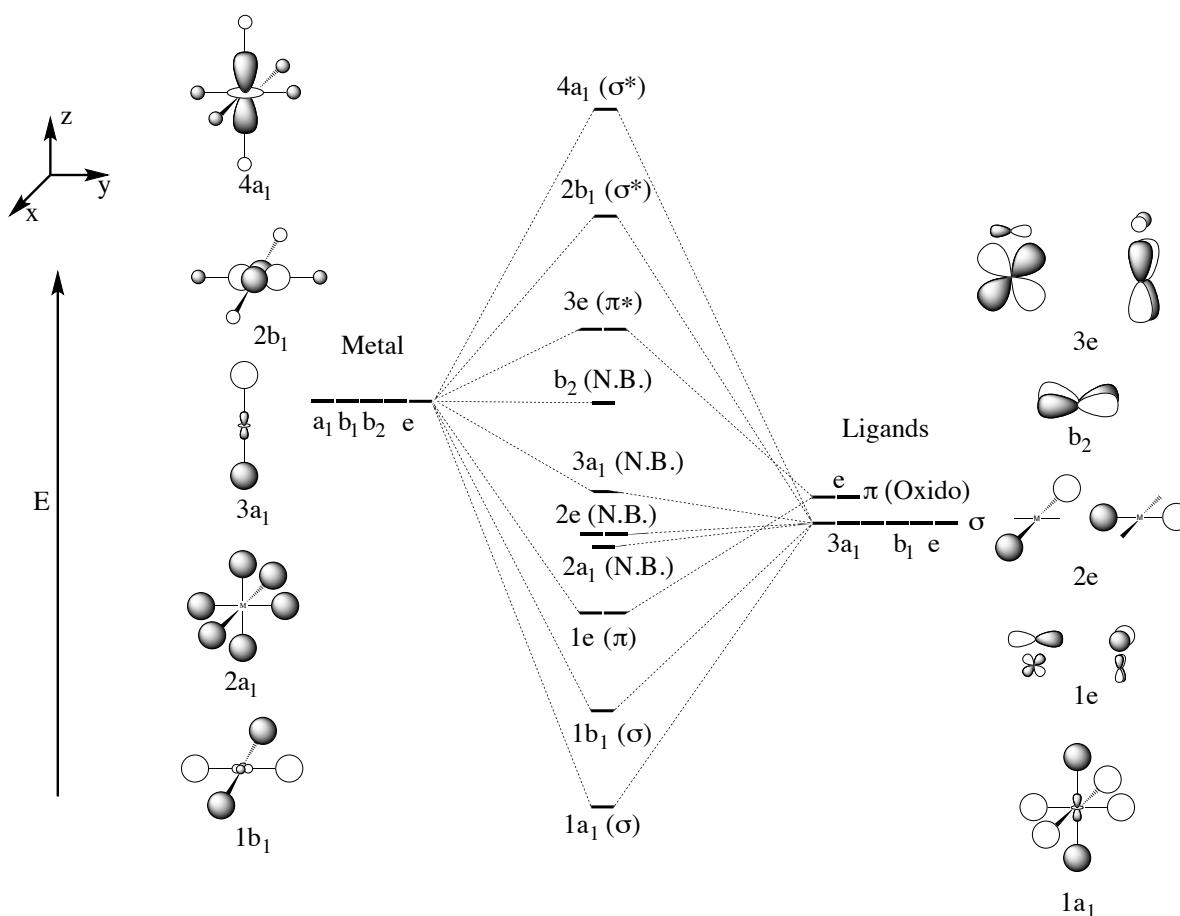


Figure 2.7 Generated ML_5O fragment representing the bonding present in the prepared $M^{\text{III}}\text{OH}$ complexes

separately in order to obtain their respective contributions. For simplicity purposes, it has been reasonably assumed that the L_5 fragment does not contribute significantly to π -bonding in the complex. As a result, the π framework transforms as a double degenerate e irrep, localized on the axial O fragment. The generated MO in **Figure 2.7** has not been drawn to scale, and should be considered a qualitative representation of the bonding present in these $[M^{III}OH(Py_5Me_2)]^{2+}$ coordination complexes.

The five “L-type” ligands present in this MO represent the polypyridyl ligand Py_5Me_2 , and contribute ten total valence electrons into the σ framework. The treatment of the orbitals involved has also been simplified; and as such they are depicted as totally symmetric spheres. These orbital contributions have been depicted above and include the bonding MO's $1a_1$ and $1b_1$, in addition to the nominally non-bonding $2a_1$ and $2e$ MO's. The O ligand has also been included in the orbital contributions depicted in **Figure 2.7**, but perhaps its most important contribution to the bonding analysis of this ML_5O fragment is in the π framework. π -bonding across the oxido bridge is what gives these bridged molecules their observed bent geometries in the analysis of their crystal structures. All of the ligand-based orbitals are filled in this ML_5O representation, and the frontier orbitals in the MO are localized largely on the metal center. The b_2 irrep is non-bonding in nature and is the lowest in energy of the metal-based orbitals. Due to the π^* nature of the d_{xz} and d_{yz} ($3e$ MO) orbitals, they are destabilized and increase in energy removing the degeneracy present in the t_{2g} set observed in O_h symmetry. This ML_5O bonding analysis can be applied to all of these $[M^{III}OH(Py_5Me_2)]^{2+}$ complexes, with the only differences being the d-electron count.

2.4 Geometric Characteristics of Synthesized Terminal Metal Hydroxides

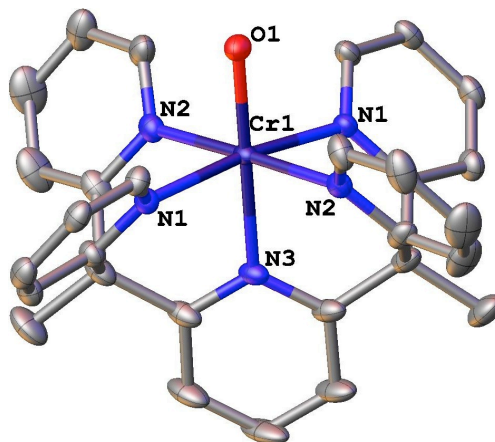


Figure 2.8 Single crystal structure of CrOH exhibiting pseudo O_h geometry

Crystal structures of the three synthesized terminal metal hydroxides have been obtained. All three complexes contain a pseudo-octahedral geometric conformation. The energy splitting between the non-bonding b_2 (d_{xy}) orbital and e ($d\pi$) set is not considerably large, as the Evan's method experiments of the Cr^{III} -OH complex confirms the presence of a high spin d^3 metal center. ($\mu_{eff} = 3.44_{BM}$). If the energy gap between the b_2 and e set were significant, the complex would favor a $S = \frac{1}{2}$ state with observable Jahn-Teller distortion present in the complex due to the partially occupied e set. As a result, the overall energy splitting of the d-orbitals can be treated as an octahedral case with C_{4v} symmetry. The crystal structure of CrOH is depicted in **Figure 2.8** with the anions and hydrogen atoms omitted for clarity. All equatorial pyridine nitrogen atoms are located within the xy plane, with the aromatic rings directed away from one another due to electron repulsion, resulting in favorable stability. The basicity of the pyridine rings in all three complexes are equivalent from the lack of modifications to the Py_5Me_2 ligand itself. Therefore, the varying bond lengths observed in the metal complexes are explained through the number of d-electrons available for bonding. Additionally, the amount of metal ligand orbital mixing as predicted by the electronegativity differences of each individual metal must also be considered when comparing the bond lengths between the metal and ligands. Selected bond lengths and angles for CrOH, FeOH, and CoOH can be found in **Table 2.2**. The single crystal X-ray structure of

CrOH shows an axial hydroxide ligand with a Cr-O bond length of 1.87 Å. This bond length is comparable to other Cr^{III} hydroxides, and considerably shorter than Cr^{III} aquo complexes of similar ligand environments.³⁸⁻⁴⁰ The average equatorial Cr-N bond length is 2.07 Å, whereas the axial Cr-N bond length is 2.09 Å.

FeOH and CoOH are structurally similar to CrOH; however they have considerably different bond lengths between the metal and ligands depending on the identity of the metal (**Figure 2.9**). In CrOH, the strongest Lewis Acid, the Cr^{III}-O bond length was found to be 1.87 Å. In FeOH and CoOH, this M^{III}-O bond length increases to 2.03 Å in FeOH and

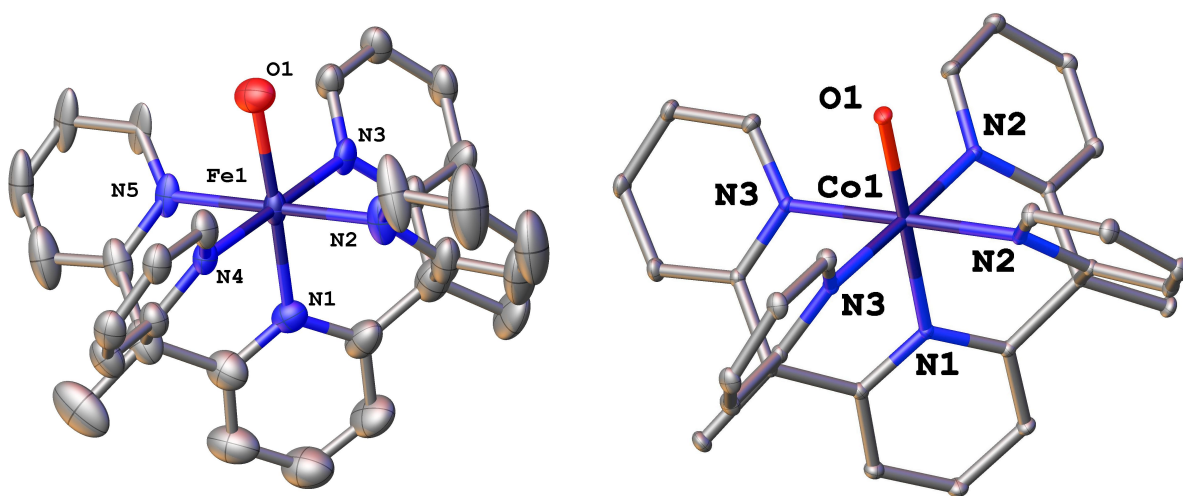


Figure 2.9 Single crystal structures obtained for the FeOH and CoOH derivatives. All three isolated M^{III}OH complexes exhibit identical coordination environments

decreases to 1.85 Å in CoOH. The increase in metal oxygen bond length in the Fe^{III} complex can be attributed to the population of the d_z^2 $d\sigma^*$ orbital in its high spin state ($S = 5/2$).

Although the increased electronegativity of Fe^{III} center reveals the potential for more orbital overlap between the iron and oxygen, the existence of an antibonding interaction negates this fact. Evan's method experiments on FeOH have been unsuccessful. The shortening of the Co^{III}-O bond length in CoOH can be attributed to the filling of the $d\pi$ set of the metal center. This complete filling of the metal bonding orbitals increases the number of potential bonding interactions with the ligands. There also exists more orbital overlap

between the Co center and Py_5Me_2 ligand when compared to the Cr derivative due to the increased electronegativity moving across the periodic table.

Table 2.2 Selected metal-ligand bond lengths in synthesized terminal metal hydroxides

Complex	M ^{III} -O Length (Å)	M ^{III} -Axial Pyridine Length (Å)	M ^{III} - Calc'd Avg. Equatorial Pyridine Length (Å)
CrOH	1.8375(16)	2.0912(17)	2.0715(56)
FeOH	2.029(8)	1.970(6)	1.9950(40)
CoOH	1.8533(8)	1.9753(6)	1.9731(123)

The average equatorial metal-pyridine distance in CrOH was found to be 2.07 Å, in FeOH it was found to be 1.99 Å, and in the Co analogue it was found to be 1.97 Å. This follows the trend of increasing electronegativity going across the periodic table, resulting in more metal-nitrogen orbital mixing. These values are not absolutely conclusive, as the average equatorial M^{III}-N bond lengths calculated for FeOH and CoOH are within the experimental error. The completely occupied e and b₂ sets in CoOH nominally results in the shortest bond lengths, as expected from this trend.

2.5 Ground State Electronic Characteristics of $M^{III}OH$ Complexes

Not only does substituting the metal change the physical structure of the complex, it also alters the resulting electronic properties. Standard solution-phase electronic absorption spectroscopy (EAS) was used to identify electronic transitions present in the terminal metal hydroxides in order to identify the MMCT band in the covalently bonded heterobimetallic complexes. As stated earlier, Py_5Me_2 -based electronic transitions dominate the spectra in the UV region, namely below 280 nm. **Figure 2.10** depicts the EAS spectrum of $CrOH$ in various solvents, but being limited by those who do not absorb strongly in the UV region of the spectrum. Two electronic transitions are observed between 350 – 650 nm, and do not exhibit any solvent-effects amongst those employed in these measurements. The band present at approximately 545 nm has been assigned to the nominally $t_{2g} \rightarrow e_g$ d-d band on the Cr^{III} center due to its lack of solvent dependency and molar absorptivity on the order of 10^2 . The

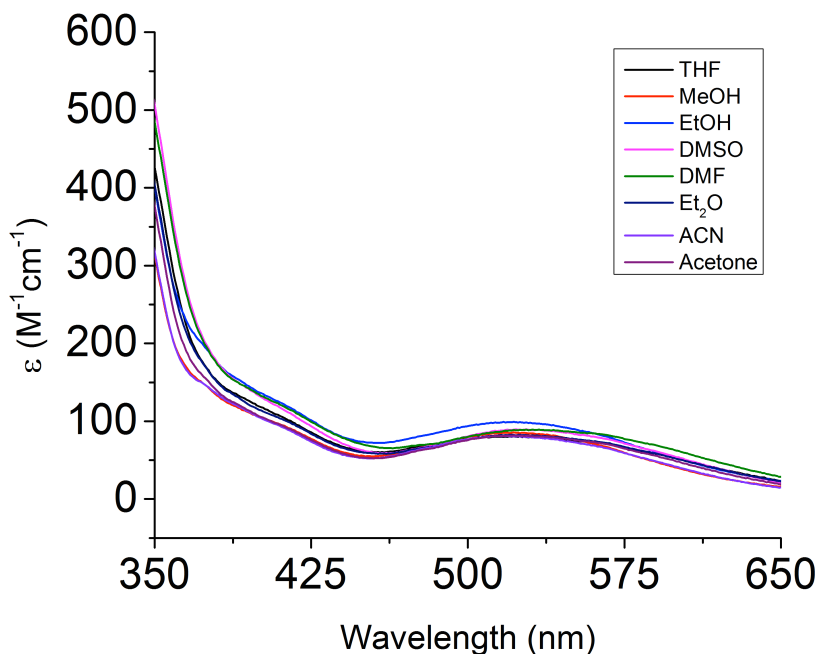


Figure 2.10 EAS of $CrOH$ taken in various solvents at a concentration of 1.0×10^{-3} M

shoulder present at approximately 385 nm in this complex does show a small solvatochromic effect. However, due to its overlap with other bands, its exact magnitude can only be qualitatively stated. This band is also on the order of 10^2 , however, due to the energy required for this transition, it is unlikely to be the result of a metal-based orbitally forbidden transition. This band has been assigned to the hydroxide \rightarrow Cr^{III} charge transfer transition, which exhibits a hypsochromic shift upon the introduction of the electron acceptor metal that will be elaborated on at length in **Chapter 3**.²⁵

These M^{III}OH Py₅Me₂ complexes do not exhibit many electronic transitions of great intensity in the UV-Vis region. This reveals their immense utility for studying MMCT bands upon the introduction of the electron acceptor metal. Since ligand-based transitions or charge transfer bands between the metal center and polypyridyl ligand do not dominate the EAS,

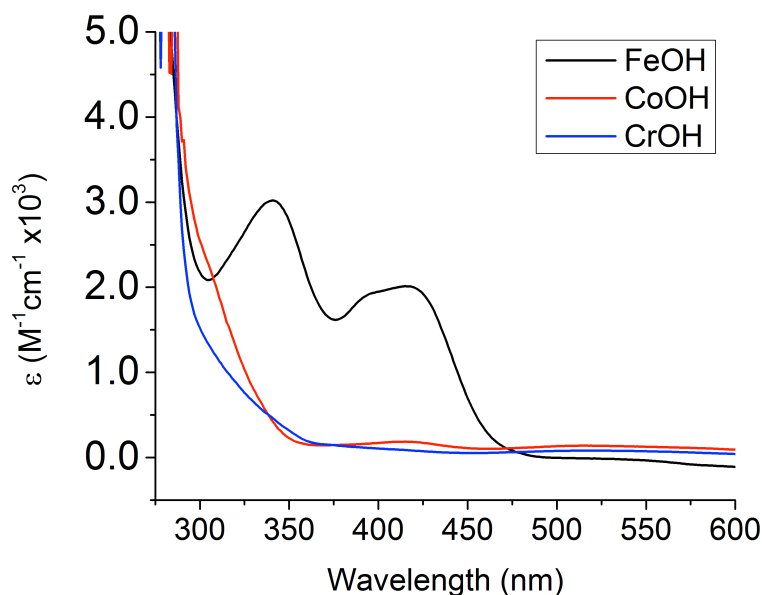


Figure 2.11 Molar absorptivity plot of CrOH, FeOH, and CoOH with all spectra obtained in acetonitrile

and new electronic transitions between metal centers should be much more resolved if they are present. **Figure 2.11** compares the differences in EAS features in the three isolated unsupported terminal metal hydroxides.

Both the Cr^{III} and Co^{III} complexes exhibit d-d bands in the 525 – 575 nm region of the EAS. One important observation however is that the FeOH derivative does not contain this

characteristic band. This can be attributed to the Fe^{III} center exhibiting a h.s. ground state $S = 5/2$ at room temperature. Not only are d-d bands in the FeOH complex orbitally forbidden due to their gerade nature, but the h.s. ground state also makes these transitions spin-forbidden thus resulting in an extremely weak intensity. Magnetic circular dichroism could be employed to investigate these transitions in all $\text{M}^{\text{III}}\text{OH}$ complexes further, however this is outside the scope of this work. The CoOH complex exhibits similar electronic absorption characteristics to CrOH. This can again be explained by the orbital occupancy characteristics of CoOH, which are identical to that of CrOH. CoOH exists in $S = 0$ ground state at room temperature which fully occupies the nominally t_{2g} set in this particular molecule.

FeOH displays many more absorption features in the EAS, mainly due to the occupancy of the e_g set which was not observed in the previous two molecules. The band at 335 nm is the result of a bathochromic shift of the hydroxide \rightarrow Fe^{III} charge transfer transition resulting from the increased electronegativity of the iron center and increased orbital mixing. Fe^{III} is a stronger Lewis acid than the previously discussed Cr^{III} center, as a result making it more electron-rich. Consequently, there is an increased propensity for MLCT in FeOH compared to the other two metal hydroxides. Overlapping, intense absorption features between 375 and 425 nm are the result of this inherent characteristic of the FeOH complex.

2.6 Redox Characteristics of $\text{M}^{\text{III}}\text{OH}$ Complexes

Employing cyclic voltammetry for electrochemical measurements allows insights as to where the frontier orbitals lie energetically in addition to their identities. A control CV of the Py_5Me_2 ligand in both acetonitrile (ACN) and trifluorotoluene (TFT) did not reveal any reductions or oxidations between 3.0 and 2.0 V (vs. Fc/Fc^+), which is consistent with the inert characteristics described in previous work using this ligand set.^{19-23, 25} Varying the identity of the electron donor offers us the opportunity to tune the energy of the MMCT transition. The electron donor in these systems is either: Cr, Fe, or Co, all existing in the +3 oxidation state. FeOH and CoOH were obtained in ACN, whereas CrOH was obtained in TFT. The $\text{Cr}^{\text{III/IV}}$ $E_{1/2}$ couple was not observable within the potential limits of ACN, revealing the need to find a suitable solvent to observe this oxidation. TFT proved to be ideal due to its

dielectric constant proximity to dichloromethane, in addition to its resistance to electrochemical oxidation. In addition to this, the standard electrolyte tetrabutylammonium hexafluorophosphate, had to be substituted due to its insolubility in TFT.

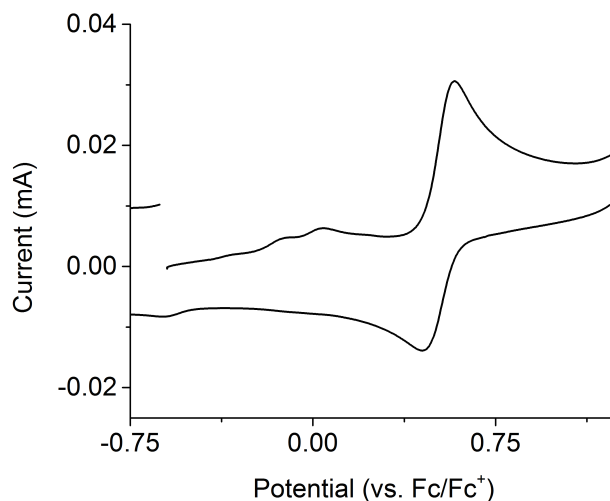


Figure 2.12 Cyclic voltammogram of FeOH depicting the reversibility of the Fe^{III/IV} couple taken in ACN

Tetrabutylammonium BAR₄' was identified as a potential substitute and was prepared through a salt metathesis reaction prepared from NaBAR₄' and tetrabutylammonium chloride. The lack of solubility in TFT of complexes with triflate counter ions prevented cyclic voltammetry measurements of the FeOH and CoOH under the same experimental conditions. This Cr^{III/IV} oxidative process is not reversible, denoted by the lack of a return wave in the cyclic voltammogram. The lack of a return wave in CrOH can be attributed to the oxidizing power of the generated transient Cr^{IV}, which may oxidize the Py₅Me₂ ligand or TFT solvent leading to the lack of electrochemical reversibility.

Table 2.3 E_{1/2} potentials for the M^{III/IV} oxidative couples in the terminal M^{III}OH complexes (vs. Fc/Fc⁺)

Complex	Solvent	M ^{III/IV} Couple (V)
CrOH	TFT	1.55
FeOH	ACN	0.514
CoOH	ACN	-0.545

FeOH and CoOH do exhibit electrochemical reversibility of the oxidative $M^{III/IV}$ couple (**Figure 2.12**), revealing their candidacy as future electron donor metals in heterobimetallic complexes. Changing the identity of the electron donor offers more than 2 eV of redox tunability of the metal in the parent $M^{III}OH$ complexes. As predicted, the most electron deficient metal center, Cr^{III} , requires the most potential to remove the first electron. The trend is completed by the Co^{III} center, which is the easiest to oxidize and whose $Co^{III/IV}$ oxidative couple cathodically shifts by 2.09 V when compared to CrOH. By lowering the energetic requirements for oxidation of the future electron donor metal, the predicted energetic requirements for MMCT should follow suit. A lower oxidative potential for the $M^{III/IV}$ couple should lead to a red-shift in the location of the observed MMCT band provided the electron acceptor identity and structure be held constant.

2.7 Cited References

- 1) Gupta, R.; Borovik, A. S., *J. Am. Chem. Soc.*, **2003**, *125*, 13234 – 13242
- 2) MacBeth, C. E.; Gupta, R.; Mitchell-Koch, K. R.; Young, V. G.; Lushington, G. H.; Thompson, W. H.; Hendrich, M. P.; Borovik, A. S., *J. Am. Chem. Soc.*, **2004**, *126*, 2556 - 2567.
- 3) Borovik, A. S., *Acc. Chem. Res.*, **2005**, *38*, 54 - 61
- 4) Parsell, T. H.; Behan, R. K.; Green, M. T.; Hendrich, M. P.; Borovik, A. S., *J. Am. Chem. Soc.*, **2006**, *128*, 8728 – 8729
- 5) Mukherjee, J.; Lucas, R. L.; Zart, M. K.; Powell, D. R.; Day, V. W.; Borovik, A. S., *Inorg. Chem.*, **2008**, *47*, 5780 – 5786
- 6) Shook, R. L.; Borovik, A. S., *Chem. Commun.*, **2008**, 6095 – 6107.
- 7) Parsell, T. H.; Yang, M. Y.; Borovik, A. S., *J. Am. Chem. Soc.*, **2009**, *131*, 2762 – 2763
- 8) Park, Y. J.; Ziller, J. W.; Borovik, A. S., *J. Am. Chem. Soc.*, **2011**, *133*, 9258 – 9261
- 9) Gary, K. Y.; Ziller, J. W.; Borovik, A. S., *Chem. Commun.*, **2012**, *48*, 2546 – 2548
- 10) Lacy, D. C.; Park, Y. J.; Ziller, J. W.; Yano, J.; Borovik, A. S., *J. Am. Chem. Soc.*, **2012**, *134*, 17526 – 17535
- 11) Park, Y. J.; Cook, S. A.; Sickerman, N. S.; Sano, Y.; Ziller, J. W.; Borovik, A. S., *Chem. Sci.*, **2013**, *4*, 717 – 726
- 12) Sano, Y.; Weitz, A. C.; Ziller, J. W.; Hendrich, M. P.; Borovik, A. S., *Inorg. Chem.*, **2013**, *52*, 10229 – 10231
- 13) Taguchi, T.; Stone, K. L.; Gupta, R.; Kaiser-Lassalle, B.; Yano, J.; Hendrich, M. P.; Borovik, A. S., *Chem. Sci.*, **2014**, *5*, 3064 – 3071
- 14) Mandal, S. K.; Roesky, H. W., *Acc. Chem. Res.*, **2010**, *43*, 248 – 259
- 15) Gurubasavaraj, P. M.; Roesky, H. W.; Sharma, M. V.; Oswald, R. B.; Dolle, V.; Herbst-Irmer, R.; Pal, A., *Organometallics*, **2007**, *26*, 3346 – 3351
- 16) Goldsmith, C. R.; Stack, T. D. P., *Inorg. Chem.*, **2006**, *45*, 6048 - 6055
- 17) Goldsmith, C. R.; Cole, A. P.; Stack, T. D. P., *J. Am. Chem. Soc.*, **2005**, *127*, 9904 - 9912
- 18) Klein Gebbink, R. J. M.; Jonas, R. T.; Goldsmith, C. R.; Stack, T. D. P., *Inorg. Chem.*, **2002**, *41*, 4633 – 4641

- 19) Sun, Y.; Bigi, J. P.; Piro, N. A.; Tang, M. L.; Long, J. R.; Chang, C. J., *J. Am. Chem. Soc.*, **2011**, *133*, 9212 - 9215
- 20) King, A. E.; Surendranath, Y.; Piro, N. A.; Bigi, J. P.; Long, J. R.; Chang, C. J., *Chem. Sci.*, **2013**, *4*, 1578 - 1587
- 21) Sundstrom, E. J.; Yang, X.; Thoi, V. S.; Karunadasa, H. I.; Chang, C. J.; Long, J. R.; Head-Gordon, M., *J. Am. Chem. Soc.*, **2012**, *134*, 5233 - 5242
- 22) King, A. E.; Nippe, M.; Atanasov, M.; Chantarojsiri, T.; Wray, C. A.; Bill, E.; Neese, F.; Long, J. R.; Chang, C. J., *Inorg. Chem.*, **2014**, *53*, 11388 - 11395
- 23) Karunadasa, H. I.; Chang, C. J.; Long, J. R., *Nature*, **2010**, *464*, 1329 - 1333
- 24) Canty, A. J.; Minchin, N. J.; Skelton, B. W.; White, A. H., *J. Chem. Dalton Trans.*, **1986**, *10*, 2205 – 2210
- 25) Falzone, A. J.; Nguyen, J.; Weare, W. W.; Sommer, R. D.; Boyle, P. D., *Chem. Commun.*, **2014**, *50*, 2139 – 2141
- 26) Lin, W.; Frei, H., *J. Phys. Chem. B*, **2005**, *109*, 4929
- 27) Lin, W.; Frei, H., *J. Am. Chem. Soc.*, **2005**, *127*, 1610
- 28) Lin, W.; Frei, H. *C. R., Chimie*, **2006**, *9*, 207
- 29) Han, H.; Frei, H., *J. Phys. Chem. C*, **2008**, *112*, 8391
- 30) Han, H.; Frei, H., *J. Phys. Chem. C*, **2008**, *112*, 16156
- 31) Han, H.; Frei, H., *Microporous Mesoporous Mater.*, **2007**, *103*, 265
- 32) Behar, D.; Frei, H.; Macnaughtan, M.; Rabani, J., *J. Phys. Chem. C*, **2012**, *116*, 23477
- 33) Lin, W.; Han, H.; Frei, H., *J. Phys. Chem. B*, **2004**, *108*, 18269
- 34) Kim, W.; Yuan, G.; McClure, B. A.; Frei, H., *J. Am. Chem. Soc.*, **2014**, *136*, 11034
- 35) Cuk, T.; Weare, W. W.; Frei, H., *J. Phys. Chem. C*, **2010**, *114*, 9167
- 36) McClure, B. A.; Frei, H., *J. Phys. Chem. C*, **2014**, *118*, 11601
- 37) Evans, D. F., *J. Chem. Soc.*, **1959**, 2003
- 38) Inamo, M.; Nakaba, H.; Nakajima, K., *Inorg. Chem.*, 2000, **39**, 4417
- 39) Qin, K.; Incarvito, C. D.; Rheingold, A. L.; Theopold, K. H., *J. Am. Chem. Soc.*, **2002**, *124*, 14008

- 40)Byun,J. C.; Yoon, C. H.; Mun, D. H.; Kim, K. J.; Park, Y. C., *Bull. Korean Chem. Soc.*, **2006**, 27, 687

3 Chapter 3: Synthesis and Ground State Characterization of Oxido Bridged Heterobimetallic Complexes

3.1 Structure and Bonding in Single Atom Bridged M-A-M Complexes

One of the earliest attempts to elucidate bonding characteristics within an oxido-bridged bimetallic system was that of a $(\text{Ru}_2\text{Cl}_{10}\text{O})^{4-}$ complex by Orgel and Dunitz.¹ The preparation and crystal structure of this molecule was first reported by Stephenson and coworkers in 1952,² and was shown to exhibit linear geometry around the M-O-M core (Figure 3.1).

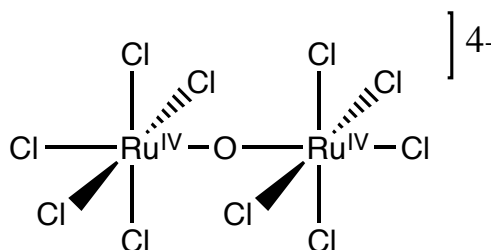


Figure 3.1 $\text{Ru}^{\text{IV}}\text{-O-Ru}^{\text{IV}}$ Complex as described by Orgel et al.¹

The complex was treated as having D_{4h} symmetry, with each metal center exhibiting local C_{4v} symmetry. This assumes the most stable conformation of the chloride ligands are eclipsed with respect to each individual metal fragment, rather than staggered. By using a standard group theory approach, it was determined that the orbital contributions of both the Cl ligands and oxido bridge transformed as: $3 A_1 + B_1 + B_2 + 2 E$. Chloride ligands were treated solely as σ -donors, as halides exhibit very weak π character, rendering it useful to ignore these interactions. The total chloride σ -contribution, both axial and equatorial, transforms as $2A_1 + B_1 + E$. The oxido ligand orbital contributions, both σ and π , transform as $A_1 (\sigma) + E (\pi)$.

In the D_{4h} point group, the metal d-orbitals transform as $A_1 (z^2)$, $B_1 (x^2-y^2)$, $B_2 (xy)$, and $E (xz, yz)$. Within the M-O-M-based orbitals, this results in two degenerate, non-bonding B_2 orbitals localized on each metal (d_{xy}). There is also the nominally non-bonding E_g set (d_{xz} , d_{yz}) localized on both metals, which also serves as the HOMO in this molecule. The next highest metal-based orbital energetically is the first $d\sigma^*$, $B_1 (d_{x^2-y^2})$, which has four anti-

bonding interactions with the chloride ligands along the x and y-axes respectively. Proceeding is the second $d\sigma^*$ orbital, $A_1(d_{z^2})$ which is anti-bonding both along the principle z-axis with the axial nodes, and with the equatorial ligands around the torus.

Linear character around the M-O-M core is attributed to the population of the non-bonding E_g set (π), with equal electron density found around each Ru center. In homobimetallic systems, this orbital does not contain any oxido bridge character. However, orbital contributions from the oxido-bridge are seen in heterobimetallic examples. This fact is the direct consequence of having two metals of differing electronegativities.

Meyer and coworkers reported the synthesis and electronic characteristics of other Ru-O-Ru dimeric species, albeit with a more sterically demanding ligand environment.³ These complexes contained bis(bipyridine) ligands (bpy) and contained two Ru^{III} centers. Unlike the diamagnetic Ru^{IV} -O- Ru^{IV} previously reported by Stephenson, these oxido bridged Ru^{III} dimers were found to be paramagnetic at room temperature. Consistent with the addition of two electrons into the metal-based anti-bonding E_g set. Meyer also treated the system in a linear sense, as the lack of bending around the M-O-M core was attributed to electron repulsion between bpy ligands. A reproduced MO diagram reported by Meyer and coworkers is depicted in **Figure 3.2**. The σ framework was omitted from this diagram due to the lack of contribution to experimentally observed spectroscopic features and lack of electron occupancy in the ground state. The π symmetry sets (n, b, and *) are stated to be different in energy due to the nature of the bpy ligands, preventing a perfectly eclipsed orientation. Electrochemical experiments by Meyer and coworkers support this electronic configuration depicted in **Figure 3.1**. The first one electron oxidative peak occurs at a fairly low potential (0.68 V vs. SSCE), suggesting this electron is anti-bonding in nature. A subsequent one-electron reduction is also observed at -0.32 V. The subsequent second electron reduction results in the decomposition of analyte, due to the complete occupation of the high-energy π^* orbital.

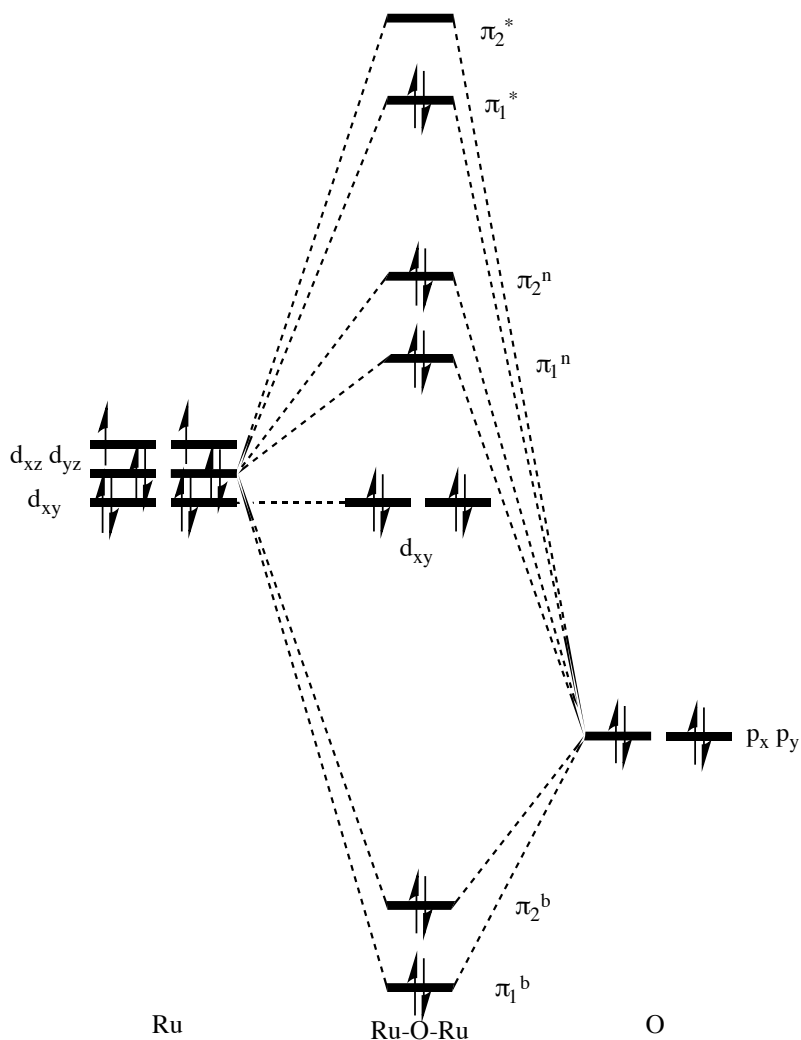


Figure 3.2 Qualitative Ru^{III}-O-Ru^{III}(bpy) dimer MO diagram published by Meyer and supported through electrochemical assignments

The lack of bending around the M-O-M core results in the lack of direct Ru-Ru interactions, and strong electronic coupling through the oxido bridge. Low energy absorption bands in the measured EAS are attributed to the π_b to π^* transition, which is symmetry-allowed giving it a significant intensity (668 nm, 17,000 ϵ). Both metals are of the same identity, thus both orbitals involved in this electronic transition are delocalized evenly on both metal centers in addition to containing significant bridge character. This observation will prove insightful when applied to the MO approach is demonstrated later in this chapter.

The early success in the 1950s – 1970s in synthesizing bridged bimetallic molecules lead to further developments in understanding the structure and bonding in these molecules. Hoffman and coworkers used extended Hückel calculations to obtain the orbital contributions on the frontier.⁴ More specifically, the energetic consequences of bending from a linear, monobridged system was studied more extensively than previously reported examples.³ As it should be expected, there are a few MOs which do not energetically change upon increasing the bond angle to 180° . Namely, the $d_{x^2-y^2}$ and d_{xy} orbitals on each metals are non-bonding with respect to each other, and do not change energetically upon bending the M-O-M bond angle.

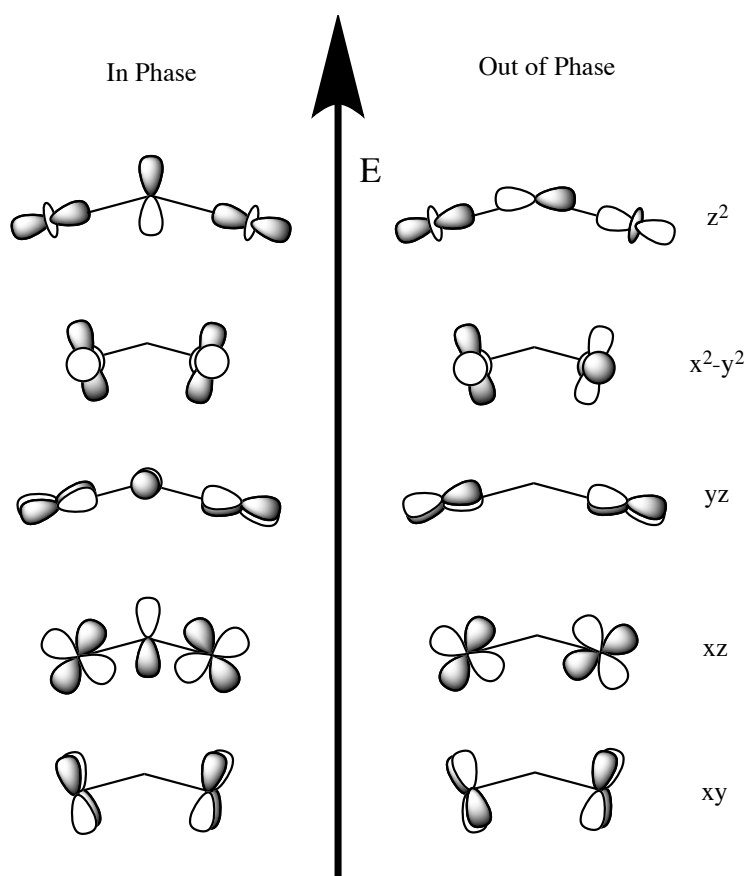


Figure 3.3 Relative energies of M-O-M molecular orbitals in a homobimetallic system

Figure 3.3 is a reproduction of the metal-based orbitals in M-O-M bimetallic molecules first reported by Hoffman.⁴ As stated earlier, the orbital overlap of the d_{xy} and $d_{x^2-y^2}$ orbitals are non-existent, and thus do not change when varying the bond angle. In the antisymmetric (out-of phase metal orbitals) the d_{xz} overlap with the bridge does not change with a varying bond angle. This is observed due to the interaction being net nonbonding, as one metal is in-phase with the bridging p_x orbital, with the other out-of phase. With respect to the in-phase example, this interaction of the two metal d_{xz} orbitals with the p_x orbital is antibonding in nature. As the molecule goes toward linear, this interaction is increasingly destabilized due to the increase in overlap of this antibonding interaction.

The orbital interactions seen with the d_{xz} orbitals are observed in with the d_{yz} orbitals. Even though the interactions are similar given the degeneracy in the linear case (D_{4h}), this interaction is not equivalent as the bond angle bends (C_{4v}). There is no change in orbital overlap when going from a bent orientation to linear, due to the nature of the bend. The M-O-M angle is treated as bending in the xz plane, thus having no effect on orbitals present in the yz plane. Finally, there is the interaction of the d_{z^2} orbitals with the bridging ligand, and in both cases the orbital overlap increases as the angle goes to 180° . In the symmetric case, the interaction goes from destabilizing (bent) to non-bonding (linear). Within the antisymmetric case, this interaction becomes increasingly more antibonding along the z -axis as the angle increases to 180° .

One other notable consequence of bending of the M-O-M angle is the reduced energy gap between the out-of phase (non-bonding) and in-phase (antibonding) combinations of the d_{xz} containing MOs.^{4,7} This realization manifests itself in the dramatically larger antiferromagnetic behavior in a linear Cr-O-Cr dimer (180°) compared to a hydroxo-bridged $\text{Cr}^{\text{III}}\text{-O-Cr}^{\text{III}}$ dimer (166°).^{5,6} It was disclosed by Hoffman that this observed magnetic behavior could also be due to the inequivalent metal-bridge bond lengths in the different complexes. However the bond angle explanation cannot be discounted.

As more advanced spectroscopic techniques were developed over time, an approach to explain newly obtained experimental observations was needed. In the late 1970s, Burdett published his review on electron transfer reactions in solution using a molecular orbital

approach.⁸ In this review, a series of ab initio-type calculations were performed, using previous work published by Hoffman and Orgel as starting points. The constructed homobimetallic MO was obtained by first generating two independent MX_5 fragments, followed by mixing these with a bridging atom, X. “X” is an atom capable of both σ and π -type interactions. It was determined that the most stable electronic configuration of a homobimetallic, M-O-M molecule contains no d-electrons. All of the L-type ligand based orbitals are filled, in addition to the orbitals localized on the bridging atom, X. It was determined by Burdett that the lowest energetically lying d-orbital was the nominally non-bonding π_g (xz, yz), which again is anti-bonding with respect to one metal, and bonding with respect to the other. This contrasts to the previously calculated lowest-lying d-orbitals by Hoffman and Meyer, which were determined to be the non-bonding d_{xy} orbitals.^{3,4} This result reported by Burdett exposes the inherent flaws of using ab initio-type calculations to obtain the orbital energies of bimetallic bridged systems, in that they are not always accurate. It can be rationalized the lowest-lying metal-centered orbital should be totally non-bonding in nature, containing no destabilizing interactions whatsoever. Which would lead one to expect the totally non-bonding d_{xy} to be energetically favored LUMO in a homobimetallic complex.

However, this revelation of the homobimetallic complex’s most stable conformation contains no d-electrons is consistent with their calculation that the π_g orbital is the lowest lying energetically. This can be rationalized by the π_g orbital containing both bonding, and anti-bonding components. This difference from previously reported could be the result of the halide bridging ligand, rather than the oxido bridge in previous examples. Then again the bridging ligand identity should not have a significant effect on the largely metal-based MOs.

In addition to the energetic positions of the metal-based MOs, Burdett also investigated the consequences of bending the M-O-M core from 180° to 140° . Upon bending, the largest effects are seen in the σ -framework. The orbital that stabilizes the most is the σ_g , or the out-of phase d_{z^2} orbitals as seen in **Figure 3.3**. This is expected as there is less overlap in this destabilizing interactions as the M-O-M core is bent to 140° . The in-phase combination of these orbitals rises in energy as the core bends, likely due to repulsion factors between the d_{z^2} orbitals of each metal respectively. The π -based orbitals also change

energetically upon bending from linear, in which the energy gap between the two (π_g and π_u) becomes smaller. This is an anticipated result as the π_g is the out-of phase nonbonding set and rises in energy upon bending. The π_u is the totally antibonding set between both metals and the bridge. As the angle bends, the negative overlap decreases, thus lowering the energy of this interaction. When these calculated consequences are compared to the experimentally reported results by Pedersen and Hodgson,^{5,6} it would be expected that halide-bridged bent homobimetallic molecules exhibit anti-ferromagnetic behavior if both metal centers contain d-electrons. This hypothesis was not tested by Burdett, but is a plausible experiment to compare their theoretical results with published experimental trends.

Additional work in the late 1980's included a Solomon et. al publication, including work on Methemerythrin and Oxyhemerythrin model systems; and contained a $\text{Fe}^{\text{III}}\text{-O-Fe}^{\text{III}}$ active site.⁹ Within this manuscript, they generated a simplified energy level diagram to

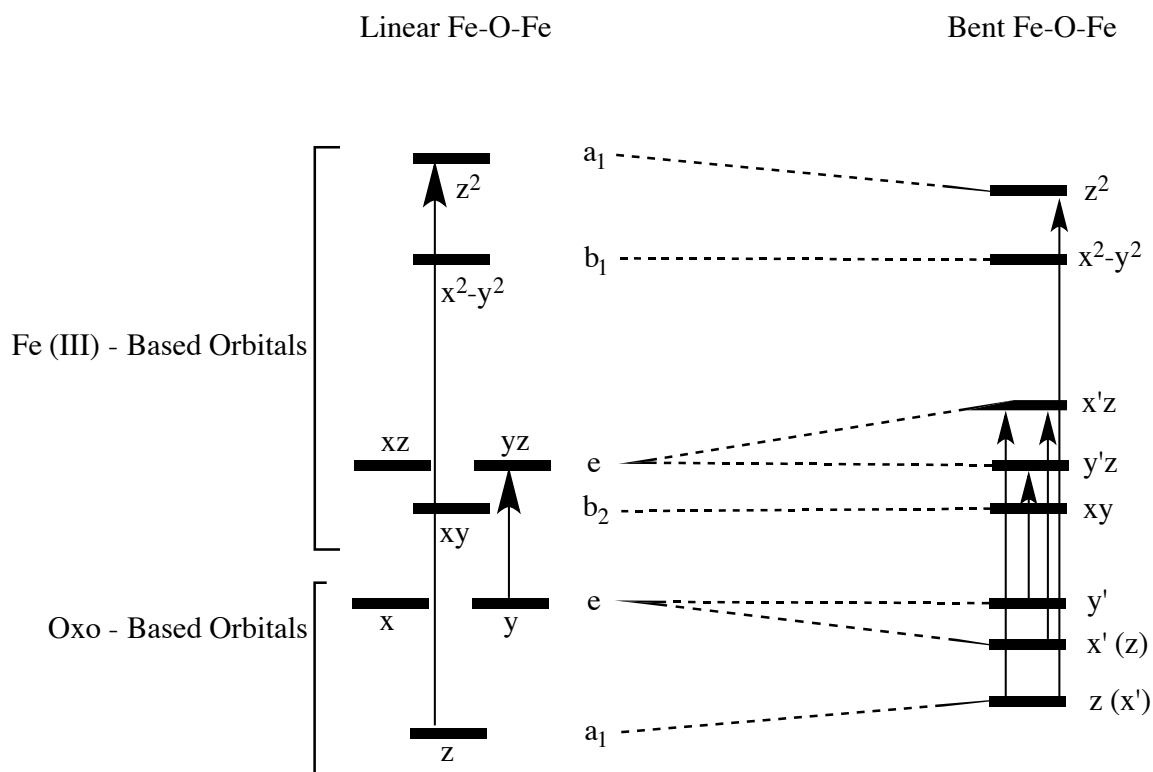


Figure 3.4 Frontier molecular orbitals in an $\text{Fe}^{\text{III}}\text{-O-Fe}^{\text{III}}$ homobimetallic systems which exhibit non-linear geometry in the M-O-M core

explain the experimentally observed spectroscopic features in their oxido-bridged ferric model complex. More specifically, they explained the observable transitions as predicted by selection rules. In this model energy level diagram, the M-O-M angle was deviated from linear to bent, which resulted in more symmetry allowed transitions due to the breaking of D_{4h} symmetry in the linear case.

In the actual proteins in question, the two iron centers are chemically inequivalent. However, the model complexes are symmetry related and treated as equivalent. This disregards any explanation of the spectroscopic features arising from charge transfer from one metal ion to the other. Bending of the Fe-O-Fe angle occurs in the xz plane, which is depicted by the orbitals along the y-axis remaining energetically unchanged. The oxido-bridged based orbital along the x-axis (p_x) lowers in energy upon bending due to decreasing π -overlap and increasing σ -overlap. As a result, the metal-based d_{x^2z} orbital is destabilized with increasing σ -interaction with the bridge. This destabilization of the d_{x^2z} orbital then results in breaking the previously degenerate d_{xz}/d_{yz} set, creating two iron-based orbitals of differing energies. Spectroscopically, this symmetry breaking results in a new symmetry afforded transition originating from the now inequivalent bridge-based orbitals to the also energetically different metal-based d_{x^2z} and d_{y^2z} orbitals. Going from a D_{4h} to C_s point group also allows for the transition from the bridge-based p_z orbital to the metal-based d_{x^2z} orbital. The highest energy band, the $p_z \rightarrow d_{z^2}$ transition, loses intensity due to the decreased σ -overlap upon bending. The energy gap between the bridge-based bonding orbital and metal-based anti-bonding orbital decreases, thus lowering the energy required for the transition.

This generated energy level diagram is consistent with those published previously, and agrees with the MO diagram generated for our synthesized heterobimetallic complexes. The spectroscopic characteristics described in Solomon's work also gives insight as to the origins of the absorption features within the complexes presented herein; namely the Fe^{III} -O-Ti^{IV} molecule.

3.2 Design of the Electron Acceptor Source: A Ti^{IV} d^0 Titanatrane

Designing a reactive metal complex that contains a leaving group capable of protonation by the metal hydroxide resulted in targeting Ti^{IV} isopropoxide complexes. Through the use of a metal center with a d^0 conformation, we avoid the use of a metal that may have competing electronic transitions both in the ground and excited state. The use of a d^0 electron acceptor also allows us to study the electron transfer mechanism as predicted by the ground state conformation of the electron donor. Thereby eliminating many possible experimental complications present with an electron acceptor with its own localized d -electrons in the ground state.

Verkade and coworkers published Ti^{IV} complexes that contain a tris-chelate ligand for use in the bulk polymerization of lactides.¹⁰ In their case, the active catalysts contained phenoxide-based leaving groups. The leaving group in our targeted titanium complexes was chosen to be isopropoxide. This was due to the decreased pK_a of isopropanol when compared to phenolic derivatives (approx. 10.0 vs. 16.5). By targeting a leaving group with a lower pK_a , we reduce the possibility of the conjugate acid deprotonating following the reaction with the protic metal hydroxide for heterobimetallic formation. Subsequent deprotonation could lead to the prevention of heterobimetallic formation, or other undesired side-products. The use of isopropoxide as our leaving group also reduced the number of synthetic steps and purification required for obtaining the desired Ti^{IV} complex.

This ligand set is advantageous in substrate polymerizations as well as stabilizing the electron acceptor in our heterobimetallic complexes. Due to the nature of the tris-chelate

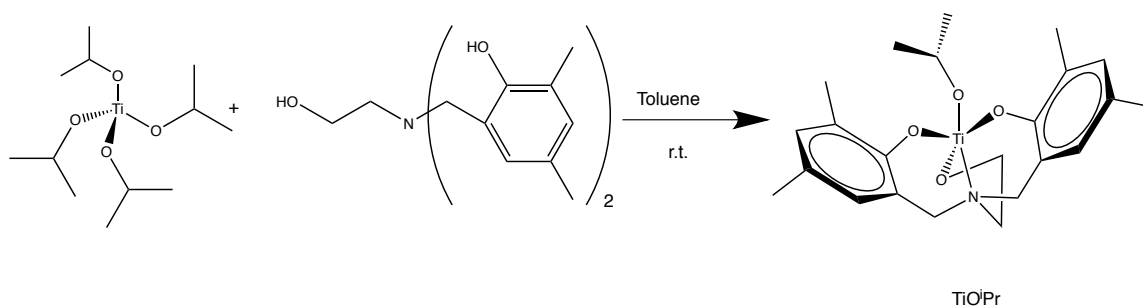


Figure 3.5 Synthesis of TiOiPr from $\text{Ti}^{\text{IV}}(\text{O}^i\text{Pr})_4$ and the tris-chelate ligand readily occurs at room temperature in toluene in the absence of moisture.

ligand, dissociation of the ligand in subsequent synthetic steps is unlikely. These ligands are synthesized according to a modified μ -wave procedure, using a Mannich-type condensation in a single reaction vessel. In addition, the ligand is redox innocent, in that it is not involved in subsequent redox processes. Electrochemical characterization of all complexes will be elaborated upon in a later section. The synthesis of aminoalcohol-bis(phenolate) and related ligands have been previously reported in the literature with moderate success.^{11,12}

Titanium isopropoxide compounds containing this type of ligand have been previously reported, yet remain to be well characterized.¹³ **Figure 3.5** is the synthetic scheme for the asymmetric methyl titanium isopropoxide complex (TiO^iPr).

This synthetic route exploits the Brønsted acid/base character of each reagent. The isopropoxide groups on the $\text{Ti}^{\text{IV}}(\text{O}^i\text{Pr})_4$ undergo protonation only if the phenolic and alcoholic protons on the ligand are more acidic than isopropoxide's conjugate acid,

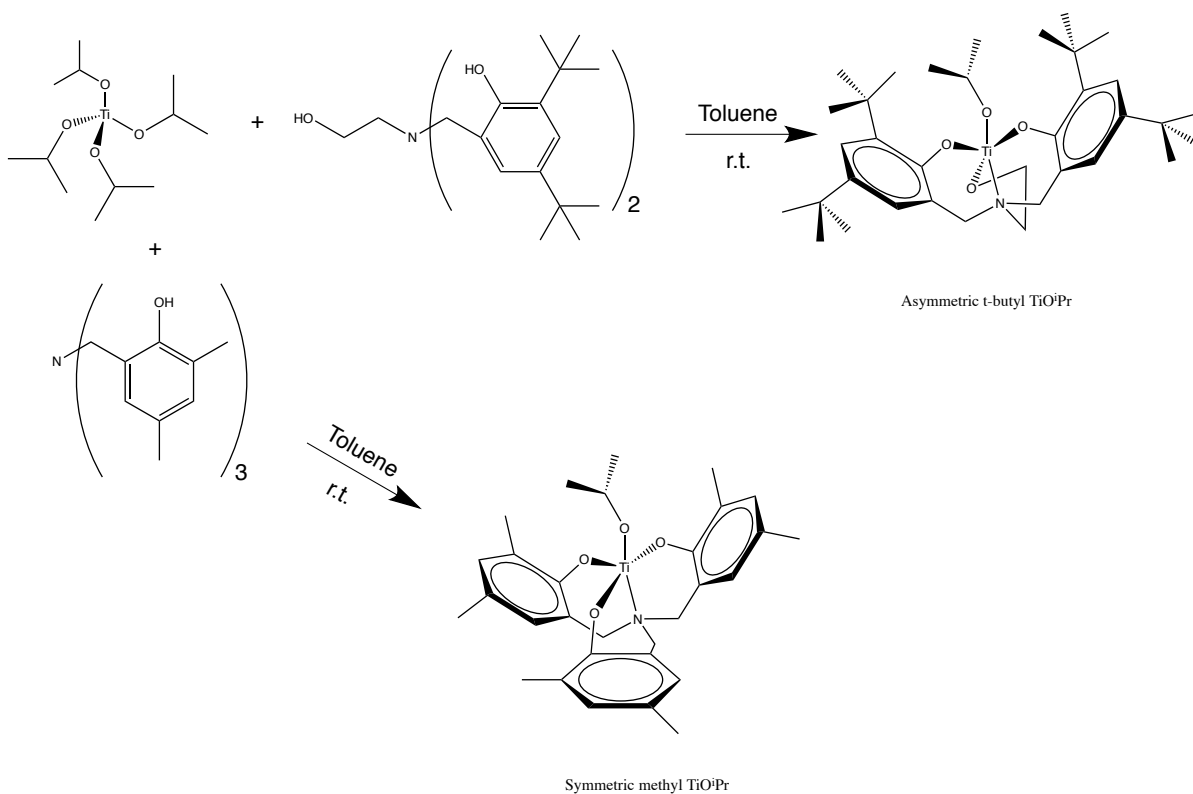


Figure 3.6 Analogous synthetic route achieves other Ti^{IV} complexes with similar structural and electronic properties

isopropanol. If this were not the case, coordination of the ligand to the metal center would not occur. However, this is not the case, as the reaction proceeds under very mild conditions with moderate yield (54.1 %) resulting in the formation of the pure complex (See **Appendix A** for full experimental details). Electrochemical experiments on the Ti^{IV} monomeric precursor did not yield any indicative peaks of the $\text{Ti}^{\text{IV/III}}$ reduction potential. This observation was expected, as the reduction potential is predicted to be lower than that of the dichloromethane solvent employed within the experiment. Acetonitrile could not be used due to the reaction with the extremely labile isopropoxide ligand, attributed to residual water in the repeatedly dried solvent. The $\text{Ti}^{\text{III/IV}}$ couple is evident in the cyclic voltammogram of the heterobimetallic complexes, which will be examined further in a later section.

Figure 3.7 depicts the electronic absorption spectrum of the TiO^iPr complex in solution. There are two distinct bands in the spectrum and having both been identified by measuring the tris-chelate ligand's spectrum independently. The transition present at 261 nm has been assigned as a ligand-based $\pi\text{-}\pi^*$ transition originating from the phenolate substituents. Due to the d^0 electronic configuration of the Ti^{IV} center and the absence of this band in the ligand's spectrum, the broad shoulder present at 332 nm has been assigned as a

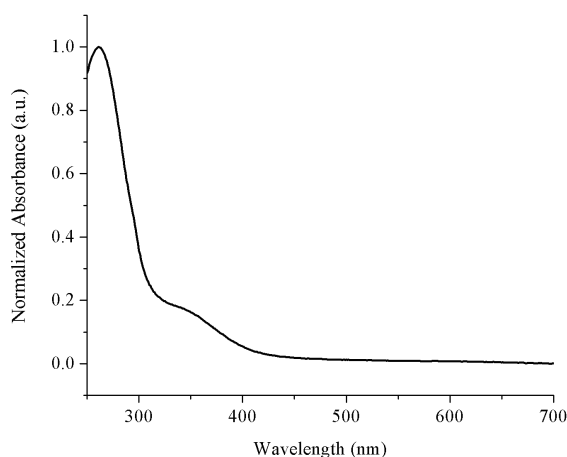


Figure 3.7 EAS of the Asymmetric Methyl $\text{Ti}^{\text{IV}}\text{O}^i\text{Pr}$ complex in DCM

LMCT transition. The symmetric methyl and asymmetric t-butyl $\text{Ti}^{\text{IV}}\text{O}^i\text{Pr}$ derivatives were synthesized and isolated however have not yet been used for the synthesis of heterobimetallic complexes. When substituting these derivatives in the formation of the heterobimetallic

complexes, there was a noticeable reduction in yield and purity. This can be attributed to the increased steric demands of the chelate ligand on the Ti^{IV} center, destabilizing the reactive intermediate en route to formation of the heterobimetallic complex. All three amino-tris chelate ligands utilized are also electrochemically inert, indicated by the lack of either reductive or oxidative Faradaic current in the cyclic voltammograms.

3.3 Synthetic Strategy and Bonding Present in Oxido-Bridged Heterobimetallic Complexes

As stated previously, the synthesis of this new class of heterobimetallic complexes is contingent on the protonation of the isopropoxide leaving group by the unsupported terminal metal hydroxide. The reaction scheme is depicted in **Figure 3.8**, and results in the formation of the isolatable heterobimetallic complexes with no purification necessary aside from the removal of unreacted starting material through solvent trituration. This reaction also generates isopropanol as a side-product, removed *in vacuo* after workup. The amount of

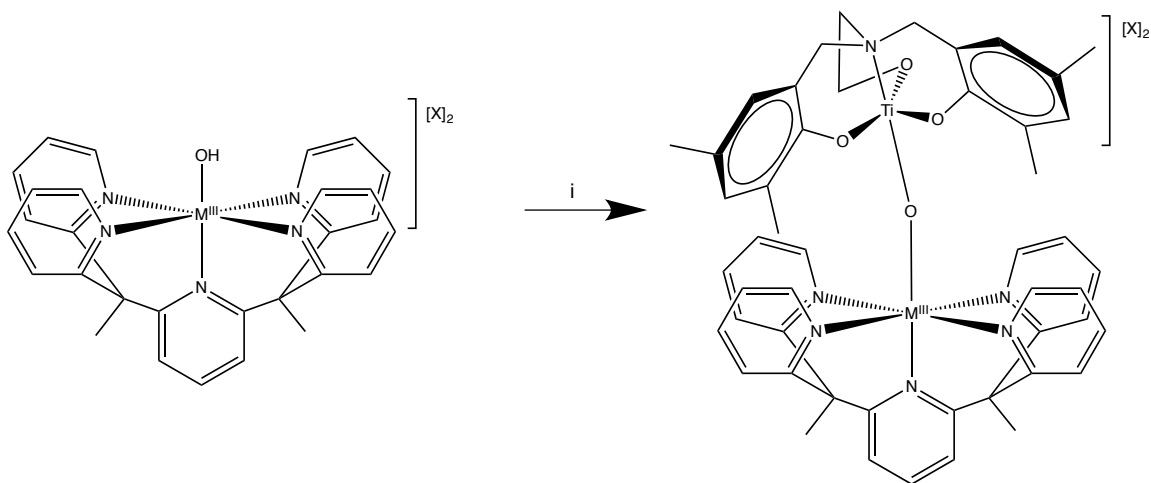


Figure 3.8 Synthesis of the heterobimetallic complexes. $M = Cr$ ($X = BAr_4'$); Fe ($X = OTf$); $M = Co$ ($X = OTf$). (i) $M^{III}OH$ is dissolved in ACN ($X = OTf$) or THF ($X = BAr_4'$) followed by reaction with $Ti^{IV}OiPr$ (1:1) for 48 hours at room temperature under inert conditions. Followed by repeated washings with *n*-pentane ($X = BAr_4'$) or THF ($X = OTf$).

isopropanol has not yet been quantified, however its generation is necessary for the reaction to proceed. The coupling of the two metal centers through the μ -oxido bridge allows for electronic coupling not seen before in the literature using this type of structural motif in molecular systems. In order to form the isolated heterobimetallic complex, the synthetic pathway likely proceeds through a one-step concerted type mechanism en route to the oxido-bridged final product.

Although the reaction time has been optimized at 48 hours at room temperature, most of the product is formed within the first four hours. With the increased reaction time, the isolated yield increases substantially, especially when using the BAr_4^- anion. Once the covalently linked oxido-bridged complexes are formed, they are stable indefinitely as a solid or in organic solution, provided they are kept free of air and residual water. When introduced to an aqueous environment, the oxido bridge is hydrolyzed, leading to an uncharacterized decomposed species. X-Ray quality crystals could be obtained for the $\text{Cr}^{\text{III}}\text{OTi}^{\text{IV}}$ and $\text{Co}^{\text{III}}\text{OTi}^{\text{IV}}$ complexes by way of vapor diffusion at room temperature in an air and moisture free environment. The structure of the $\text{Fe}^{\text{III}}\text{OTi}^{\text{IV}}$ has proven to be elusive, as residual iodosobenzene in the bulk isolated powder has prevented high-quality crystal growth. However, its isolation has been confirmed through spectroscopic measurements in addition to obtaining its m/z through HR-ESI/MS.

Table 3.1 Experimentally obtained m/z values through HR-ESI/MS measurements ($Z = 2$)

Complex	Chemical Formula	Calc'd m/z	Obtained m/z
$\text{Cr}^{\text{III}}\text{OTi}^{\text{IV}}$	$\text{C}_{49}\text{H}_{49}\text{CrN}_6\text{O}_4\text{Ti}$	442.6350	442.6350
$\text{Fe}^{\text{III}}\text{OTi}^{\text{IV}}$	$\text{C}_{49}\text{H}_{49}\text{FeN}_6\text{O}_4\text{Ti}$	444.6316	444.6305
$\text{Co}^{\text{III}}\text{OTi}^{\text{IV}}$	$\text{C}_{49}\text{H}_{49}\text{CoN}_6\text{O}_4\text{Ti}$	446.1307	446.1315

Prior to discussing the spectroscopic and geometric characteristics observed in these complexes, it is important the frontier orbitals involved in the observed reactivity and structural characteristics are understood. The starting point for this expands on the molecular orbital diagram discussed at length in **Chapter 2**, which involved treating the molecular

$M^{III}OH$ model system with C_{4v} symmetry in the generation of a model ML_5O MO. In order to comprehend the bonding and electronic transitions originating from the $M^{III}OTi^{IV}$ core, the frontier metal-based orbitals is the centralized focus. One assumption was necessary in the generation of the first $M-O-M'$ molecular orbital fragment is that the bond angle between the two metal centers across the oxido bridge is 180° . This treatment follows previous examples presented earlier in Section 3.1 and results in the treatment of the $M-O-M'$ core with D_{4h} symmetry. In order to simplify the molecular orbital analysis of this model system for our

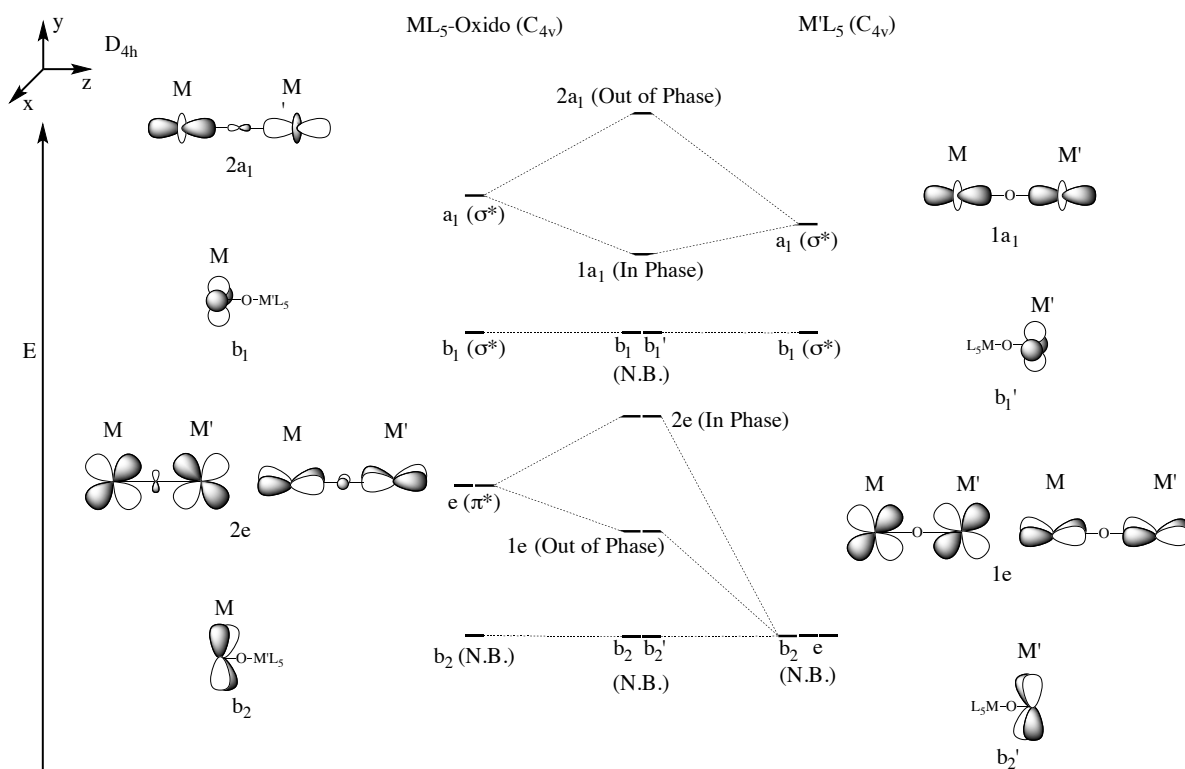


Figure 3.9 Simplified $M-O-M'$ MO diagram depicting the metal-based frontier orbitals with both metals having a d^0 electronic configuration.

understanding, avoiding non-linear molecular geometries was necessary. Upon bending the $M-O-M'$ angle from linear, the symmetry of the E set is broken resulting in the loss of orbital degeneracy. The second simplification of the generated $M-O-M'$ fragment was that the identity of both metals are the same and has been assigned to a d^0 configuration (**Figure 3.9**).

In order to generate this qualitative MO diagram of the model $M-O-M'$ system, it was necessary to mix the previously generated ML_5O portion with a simplified $M'L_5$ fragment

that contained an identical ligand environment except for the oxido portion. Since the synthesized heterobimetallic molecules contain a single atom bridge, mixing two identical ML_5O fragments together would not be the best representative model for this system. The relative decrease in energies of the $M'L_5$ MO fragment are the result of lacking an oxido contribution, which destabilizes the molecular orbitals treated in the M-O-M' model above. There are two sets of nominally non-bonding molecular orbitals with respect to the bridging oxygen atom in this simplified model molecular orbital diagram. The first of which is the b_2 and b_2' set, which represents the d_{xy} orbital which is both non-bonding in nature to the M-O-M' bridge in addition to the L_5 components as well. A somewhat destabilized non-bonding molecular orbital is higher in energy and is representative of the two $d_{x^2-y^2}$ orbitals. They are non-bonding in nature with respect to the frontier but anti-bonding in nature with the axial ligand fragments on each metal center.

The lowest-lying molecular orbital which contains orbital contributions of each metal and has some overlap across the M-O-M' bridge is the degenerate e set and represents the out-of-phase combinations of the $d\pi$ orbitals. In the homobimetallic simplification there is no bridging atom character contribution to this orbital, as its positive and negative overlap contributions negate each other. The in-phase combination of the $d\pi$ orbitals is slightly higher in energy, largely due to the anti-bonding interaction with the bridging oxygen. The electronic coupling between these two degenerate $d\pi$ orbitals is necessary for observed MMCT, as the lowest lying out-of-phase combination of these orbitals is the HOMO in the synthesized complexes. The final MO's contributing to the bonding across the M-O-M' bridge are σ^* with the p_z orbital of the bridging oxygen atom and having a large amount of negative overlap. The in-phase combination of the two d_{z^2} orbitals does not have any bridging atom character, as the positive and negative overlap is negated in the $1a_1$ MO. These orbitals are still anti-bonding in nature with respect to the L_5 interactions, leading to their designation of the most destabilized metal-based MO. The out-of-phase combination of the d_{z^2} orbitals, $2a_1$, is anti-bonding with respect to the bridging atom and both metals. In this first model system MO, the contribution of each metal to each respective interaction is assumed to be equivalent based on the assumed identical electronegativities. However, once

one of the metal identities is changed there is a noticeable deviation from equivalency. In MO depicted in **Figure 3.10**, the metal identities are correlated to the heterobimetallic complex $\text{Cr}^{\text{III}}\text{OTi}^{\text{IV}}$ however the simplifications outlined for the linear homobimetallic are held constant. The Ti^{IV} d^0 metal is representative and directly analogous to the electron acceptor in the molecules presented herein. The d^3 metal in this molecular orbital treatment is relatable to the Cr^{III} metal center, which has been assigned as our electron donor in the $\text{Cr}^{\text{III}}\text{OTi}^{\text{IV}}$ molecule.

Upon changing one of the metal's identities from a d^0 assignment to a d^3 electronic configuration and holding the other constant, there are noticeable differences in the orbital contributions and energies of each MO. The non-bonding orbitals' contributions do not change, however the degeneracies seen in the homobimetallic complex are absent in the

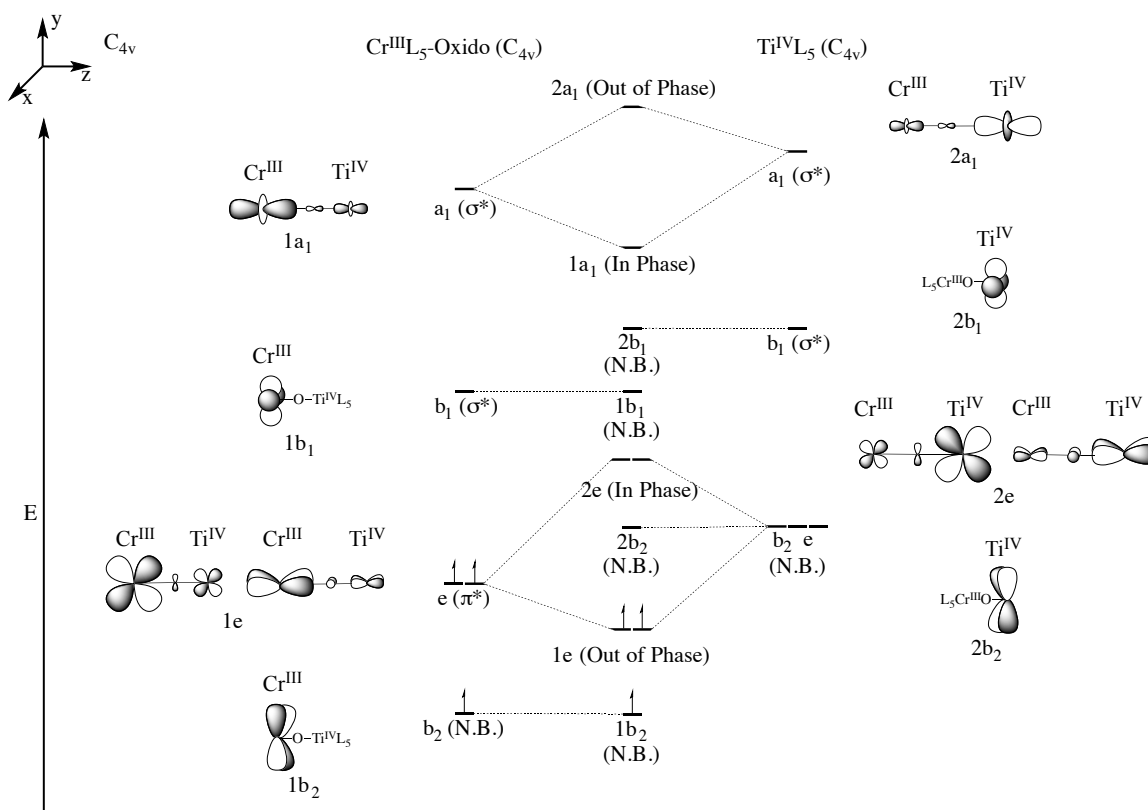


Figure 3.10 Simplified heterobimetallic MO diagram featuring the frontier orbitals of a $\text{Cr}^{\text{III}}\text{OTi}^{\text{IV}}$ model system

heterobimetallic complex model system. The more electron deficient d^0 metal's non-bonding orbitals, $2b_2$ and $2b_1$, are higher in energy than those of the electron donor metals'. Although the d_{xy} orbital ($2b_2$) is the LUMO in this heterobimetallic model system, an electronic transition involving this orbital is not expected due to the orbitally forbidden nature of such a transition. The non-bonding d_{xy} orbital ($1b_2$) of the Cr^{III} is representative of the HOMO - 1 in the heterobimetallic complex, and is partially occupied. The out-of-phase combination of the two metals has a significantly larger contribution from the Cr^{III} center, but also sees contribution from both the oxido bridge and Ti^{IV} . As a result of perturbing one metal's identity, the absence of bridging atom contribution to the out-of-phase metal combinations can no longer be assumed. The $1e$ orbital is $d\pi^*$ in nature with respect to the bridging atom and metal centers, and this degenerate set is partially occupied which results in the experimentally observed $S = 3/2$ configuration of the donor metal and is the HOMO. The $2e$ set is analogous to that seen in the previous homobimetallic model, however is largely Ti^{IV} in nature with a small contribution from the bridging atom and Cr^{III} metal. Lastly, the $d\sigma^*$ orbitals which includes the bridging p_z orbital in addition to the metals' d_{z^2} orbitals are highest in energy and also have inequivalency present in the in and out of phase combinations. With the model heterobimetallic systems now presented in detail, if an MMCT is present in these molecular oxido bridged systems it's likely origin is from the $1e$ HOMO, is localized on the M^{III} center. With the large amount of electronic coupling between the two metal centers and the bridge, this electron would likely transition to the $2e$, LUMO + 1 orbital which is largely Ti^{IV} in nature.

3.4 Ground State Characterization of Oxido Bridged Heterobimetallic Complexes

The EAS spectrum of the heterobimetallic complexes exhibits the growth of a new band, assigned as the MMCT transition. Electronic transitions present in the parent complexes are still observable, and gain intensity due to breaking the symmetry of the parent molecule. All heterobimetallic complexes are asymmetric, exhibiting C_1 symmetry. The coupling of the two metal centers results in the formation of a new absorption band in the UV/Visible spectrum, assigned to the newly formed metal-to-metal charge transfer. In order to elucidate the absorption spectral features of $\text{Cr}^{\text{III}}\text{OTi}^{\text{IV}}$ (**Figure 3.11A**), the electronic absorption spectra of mononuclear CrOH and TiO^iPr were recorded, and the sum of their spectra were overlaid with the heterobimetallic dimer, $\text{Cr}^{\text{III}}\text{OTi}^{\text{IV}}$ (**Figure 3.11A**). The mathematical difference was determined as $[\text{Cr}^{\text{III}}\text{OTi}^{\text{IV}} - (\text{CrOH} + \text{TiO}^i\text{Pr})]$, and is depicted in **Figure 3.11B**. The difference spectrum was fit with two Gaussians, centered at 4.32 and 3.98 eV. A new absorption feature for $\text{Cr}^{\text{III}}\text{OTi}^{\text{IV}}$ is evident as the fitted red curve in **Figure 3.11B**, and is assigned to the $\text{Cr}^{\text{III}}\text{-O-Ti}^{\text{IV}}$ to $\text{Cr}^{\text{IV}}\text{-O-Ti}^{\text{III}}$ MMCT transition.¹⁴⁻²⁰ The lower energy transition was assigned to the O- Cr^{III} LMCT, which is 0.68 eV higher in energy compared to CrOH . The higher energy transition at 4.32 eV (MMCT) was fitted with to Gaussian curve

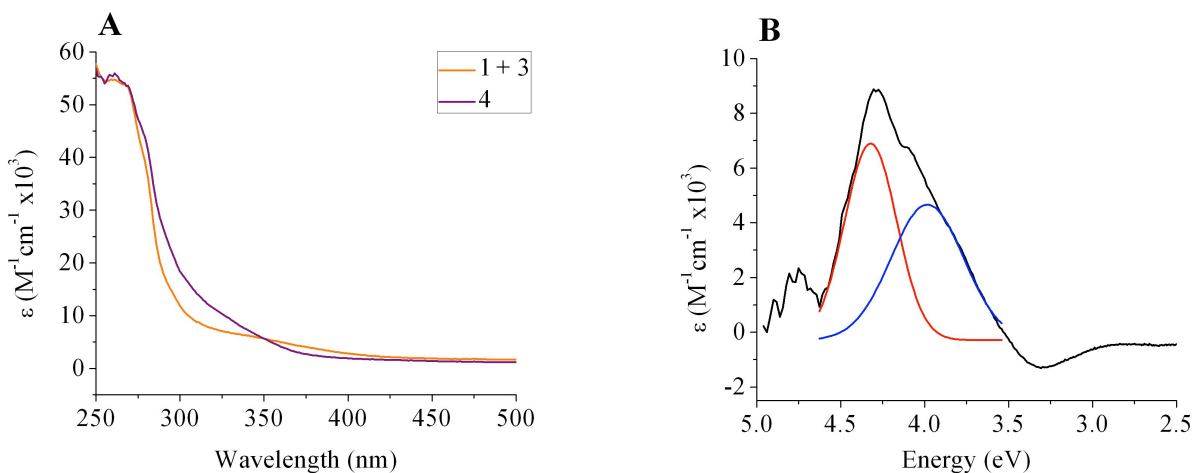


Figure 3.11 Combined absorption spectra of **1^b** (CrOH) and **3** (TiO^iPr) (purple curve) versus **4** ($\text{Cr}^{\text{III}}\text{OTi}^{\text{IV}}$) (orange curve) is depicted in A. The mathematical difference between the two curves results in the fitting of a new band at 4.32 eV (288 nm), assigned to the $\text{Cr}^{\text{III}}\text{-O-Ti}^{\text{IV}}$ to $\text{Cr}^{\text{IV}}\text{-O-Ti}^{\text{III}}$ MMCT (red curve) in B.

with an intensity of $7178 \text{ M}^{-1}\text{cm}^{-1}$. Whereas lower energy curve centered at 3.98 eV was fitted with a Gaussian with an intensity of $4945 \text{ M}^{-1}\text{cm}^{-1}$. The intensity of the LMCT present at 3.98 eV is significantly higher than that in the parent complex, which is attributed to breaking pseudo- C_{4v} symmetry resulting in greater electronic coupling between the metal and μ -oxido bridge when compared to the metal hydroxide precursor.

This spectral deconvolution procedure was also used on the Fe^{III} derivative complex, which contains an Fe^{III} donor metal and an identical ligand environment around the Ti^{IV} electron acceptor. **Figure 3.12** depicts the resulting mathematical sum in $\text{Fe}^{\text{III}}\text{OTi}^{\text{IV}}$ using the same method implemented in $\text{Cr}^{\text{III}}\text{OTi}^{\text{IV}}$. The developing trend of increasing intensities of observed transitions is evident. Similarly observed in **Figure 3.11**, the transitions present in both monomeric precursors to the heterobimetallic gain intensity, and shift upon the breaking of pseudo- C_{4v} symmetry, and subsequent electronic coupling to the Ti^{IV} donor metal. The shaded region in the spectral overlay plot is representative the increase in absorption intensity seen in the iron heterobimetallic complex. The existence of more absorption bands in the Fe^{III} containing complex can be attributed to more d-electrons present available for excitation into vacant, ligand-based MO's. The newly formed MMCT is evident by the fitted curve

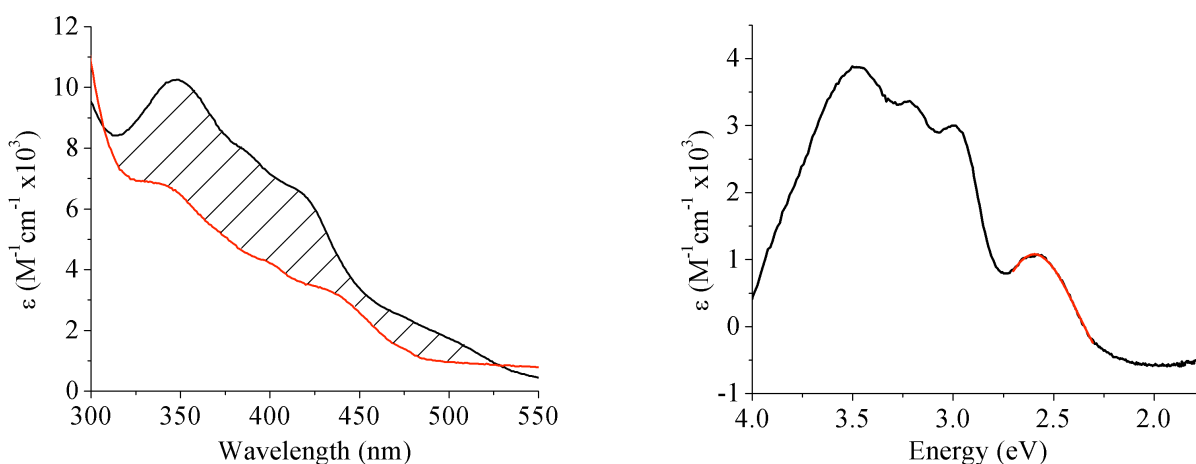


Figure 3.12 Combined absorption spectra of FeOH and TiO^{iPr} (red curve) versus $\text{Fe}^{\text{III}}\text{OTi}^{\text{IV}}$ (black curve) is depicted in the left EAS. The mathematical difference between the two curves results in the fitting of a new band at 2.59 eV (478 nm), assigned to the $\text{Fe}^{\text{III}}\text{-O-Ti}^{\text{IV}}$ to $\text{Fe}^{\text{IV}}\text{-O-Ti}^{\text{III}}$ MMCT (red curve) in the rightmost plot.

Just as seen in the $\text{Cr}^{\text{III}}\text{OTi}^{\text{IV}}$ system, the charge transfer bands present in the parent FeOH complex are blue-shifted once coupled to the Ti^{IV} electron acceptor. Due to the addition of a large electron deficient metal, the relative ligand field strength increases resulting in this hypsochromic shift in LMCT and MLCT transitions. The intensity of the MMCT in $\text{Fe}^{\text{III}}\text{OTi}^{\text{IV}}$ is significantly less ($\approx 1150 \text{ M}^{-1}\text{cm}^{-1}$) than that seen in the analogous chromium complex, indicating that the electronic coupling between the two metals is decreased upon donor metal substitution.

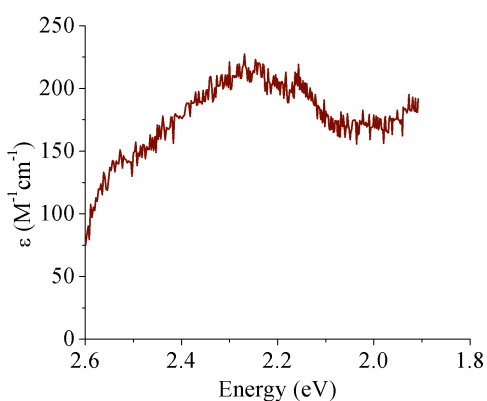


Figure 3.13 Electronic difference spectrum of $\text{Co}^{\text{III}}\text{OTi}^{\text{IV}}$ with an assigned MMCT centered at 2.26 eV.

Continuing the trend of varying the identity of the electron donor, $\text{Co}^{\text{III}}\text{OTi}^{\text{IV}}$ also exhibits a MMCT transition in the visible region. The amount of electronic coupling in this complex is significantly less than that observed in the previous two heterobimetallic complexes, with an intensity on the order of $10^2 \text{ (M}^{-1}\text{cm}^{-1})$. In comparison of the Fe^{III} and Co^{III} derivatives to the $\text{Cr}^{\text{III}}\text{OTi}^{\text{IV}}$ complex, redshifting the MMCT band through the substitution of a more electron rich metal comes at a cost to the electronic coupling of the donor and acceptor metal centers. As the Δ in electronegativities of the two metal centers becomes larger, the electronic communication between the two measured through EAS is noticeably diminished. **Figure 3.13** depicts the resulting difference spectrum obtained mathematically with the newly formed MMCT transition centered at 2.26 eV. The MMCT in $\text{Co}^{\text{III}}\text{OTi}^{\text{IV}}$ is lowest in energy amongst the three heterobimetallic complexes synthesized, however due non-ideal S/N ratio a fitted Gaussian for the electronic transition could not be generated with a large degree of confidence. Despite this fact, the ability to shift the MMCT

into a region of the visible spectrum that has a larger abundance of photons present in nature has been demonstrated.

Calculating the degree of electronic coupling between the ground state and initially generated Franck-Condon state as seen in electronic absorption spectra is possible by using an approach introduced by Hush and coworkers, and recently employed by McClure et al.^{21, 22}

$$\textbf{Equation 3.1} \quad |H_{ABopt}| = \frac{2.06 \times 10^{-3}}{r} \left(\epsilon_{max} \nu_{max} \Delta\nu_{1/2} \right)^{1/2} \text{ cm}^{-1}$$

Equation 3.1 is representative of the quantity H_{ABopt} , which is the degree of optical coupling between the ground state and Franck-Condon state as measured by electronic absorption spectra. To calculate this value, it is necessary to have the geometric parameters of the molecule or system of interest, to determine the equilibrium distance between the orbitals involved in an electronic transition. In **Equation 3.1**, this distance is represented by the parameter, r . For these heterobimetallic complexes, this distance is the through-space distance between the donor (M^{III}) metal and Ti^{IV} acceptor and is obtained through crystallographic analysis and has units of nm. The other three variables necessary to calculate the optical coupling are obtained through fitting the spectroscopically observed absorption curves. Molar absorptivity of the absorption band, ϵ_{max} , with units of $M^{-1}cm^{-1}$ and ν_{max} is the energy of the transition, with units of cm^{-1} . Finally, the $\Delta\nu_{1/2}$ is the full peak width at half maxima of the fitted Gaussian curves outputted by software used, also with units of cm^{-1} . This was calculated for $Cr^{III}OTi^{IV}$ and approximated for $Fe^{III}OTi^{IV}$. The calculated electronic coupling present in $Cr^{III}OTi^{IV}$ was determined to be 5597 cm^{-1} . For the Fe^{III} derivative, the exact distance between the Fe^{III} and Ti^{IV} centers remains unknown due to the lack of an isolated crystal structure, yet can be approximated using the bond lengths measured in the $Cr^{III}OTi^{IV}$. Electronic coupling in $Fe^{III}OTi^{IV}$ is less than that of present in $Cr^{III}OTi^{IV}$ at roughly 2400 cm^{-1} . These values are fairly consistent to those in a recently published material which exhibits MMCT,²² and indicate significant electronic coupling between the ground state and initial Franck-Condon state. Systems that have significantly optical coupling such

as those herein are predicted to have relatively short excited state lifetimes ($< \text{ns}$), indicated by the strong coupling between the ground and initially generated excited state.

In order to further confirm assignments of the MMCT locations, cyclic voltammetry was employed to measure the redox potentials of all electroactive species in solution. In addition to confirming the assignment of the electronic transitions, by obtaining the $E_{1/2}$ potentials of the both the donor and acceptor metals it allows us to determine viability as potential photoredox catalysts. For the heterobimetallic complexes, some degree of electrochemical reversibility of the metals' $E_{1/2}$ needs to be observable for the complexes to be viable catalysts.

Table 3.2 $E_{1/2}$ potentials obtained via cyclic voltammetry. Solutions were prepared in the designated solvent with a supporting electrolyte concentration of 0.1 M

Complex	Solvent	M ^{III/IV} Couple (V)	Ti ^{III/IV} Couple (V)
CrOTi	TFT/ACN	1.75	-2.49
FeOTi	ACN	0.530	-2.31
CoOTi	ACN	-0.545	-2.50

The location of the Cr^{III/IV} couple is also shifted in the heterobimetallic complex when compared to the monomeric Cr^{III} precursor, CrOH. A cathodic shift in the irreversible Cr^{III/IV} redox couple is observed at 1.75 V in trifluorotoluene. The cyclic voltammogram of Cr^{III}OTi^{IV} was also taken in acetonitrile due to its extended reduction potential range when compared to trifluorotoluene. The quasi-reversible Ti^{IV/III} redox couple is evident in the heterobimetallic complex at -2.49 V vs. Fc/Fc⁺. This Ti^{IV/III} couple becomes evident in the heterobimetallic complex due to the stabilization of the unpopulated d-orbitals localized on the Ti^{IV} center through electrostatic interactions with the Cr^{III} donor metal. Following Hush's approach,²³ the difference between the two redox couples of our donor and acceptor metal gives insight into the energy requirements of MMCT. The difference between the Cr^{III/IV} oxidation and Ti^{IV/III} reduction is calculated at 4.24 eV. This value is well within reason for the fitted MMCT curve at 4.32 eV in the spectral difference spectrum as seen in **Figure 3.11B**. While it is noted that both redox potentials were obtained in different solvents,

experimental limitations limits the ability to obtain both $E_{1/2}$ potentials in identical environments. This discrepancy may be the contributing factor to the lower expected Δ between the two redox potentials, as one would expect a calculated value larger than the fitted MMCT curve at 4.32 eV due to the contribution of reorganization energy in the cyclic voltammograms.

When comparing the redox potential of the $\text{Fe}^{\text{III/IV}}$ to that of $\text{Cr}^{\text{III/IV}}$, it is evident the donor oxidation becomes electrochemically reversible (**Appendix D**). The shift of the $\text{Fe}^{\text{III/IV}}$ couple is also cathodic, albeit with a much smaller shift than that of the electron donor in $\text{Cr}^{\text{III}}\text{OTi}^{\text{IV}}$. This $\text{Fe}^{\text{III/IV}}$ redox couple shifts from 0.51 V in FeOH to 0.53 V in $\text{Fe}^{\text{III}}\text{OTi}^{\text{IV}}$. This observable electrochemical reversibility of the donor offers insight into the potential photochemical applications of the iron containing heterobimetallic complex. The oxidative characteristics of Fe^{IV} are much milder than Cr^{IV} , reducing the potential for either solvent or ligand oxidation by the generated transient Fe^{IV} species. If the oxidative process localized on the donor metal is electrochemically reversible, the heterobimetallic complex should be able to undergo many subsequent forward and back electron transfer processes from donor to acceptor without degradation. The $\text{Ti}^{\text{IV/III}}$ reduction is present at -2.31 V in, which resembles a slight cathodic shift in the reduction potential of the acceptor metal. This decrease in potential required to perform a one-electron reduction to the electron acceptor can be attributed to the electronic coupling to a more electron-rich metal center in Fe^{III} when compared to Cr^{III} . Once again by using Hush's approach, we find that the potential difference between the $\text{Ti}^{\text{IV/III}}$ reduction and $\text{Fe}^{\text{III/IV}}$ oxidation is calculated at 2.84 V, also well within experimental reason of the fitted MMCT curve at 2.59 eV depicted in **Figure 3.12**.

The $\text{Co}^{\text{III/IV}}$ oxidation peak in $\text{Co}^{\text{III}}\text{OTi}^{\text{IV}}$ remains relatively unchanged relative to the monomer, assigned to the reversible peak at -0.55 V vs Fc/Fc^+ (**Appendix D**). The quasi-reversible $\text{Ti}^{\text{IV/III}}$ reduction occurs at -2.50 V, which is consistent to the potential of this reduction seen in the previous two heterobimetallic complexes. Once again, utilizing Hush's approach we find that the mathematical difference of these two redox processes is 1.96 V. This deviation from the assigned MMCT band centered at 2.26 eV can be attributed to the signal to noise ratio evident in **Figure 3.13**, in addition to the lack of a fitted Gaussian to this

absorption feature. This degree of uncertainty in the assignment to the MMCT band to 2.26 eV renders it reasonable the assignment of the two respective $E_{1/2}$ potentials for the donor and acceptor metal are accurate. One would expect there to be a larger calculated difference between the two redox processes when compared to the electronic absorption spectra due to reorganization energy, λ .

3.5 Structural Characteristics of Oxido Bridged Heterobimetallic Complexes

X-Ray quality single crystals were grown of $\text{Cr}^{\text{III}}\text{OTi}^{\text{IV}}$ and $\text{Co}^{\text{III}}\text{OTi}^{\text{IV}}$, providing crucial information about the molecular geometry seen in these oxido-bridged molecules. The structure of such complexes are relatively unknown in the literature, as not many single-atom bridged complexes have been reported, especially those with d-electrons. The full crystallography reports with refinement information can be located in **Appendix H**. Crystals

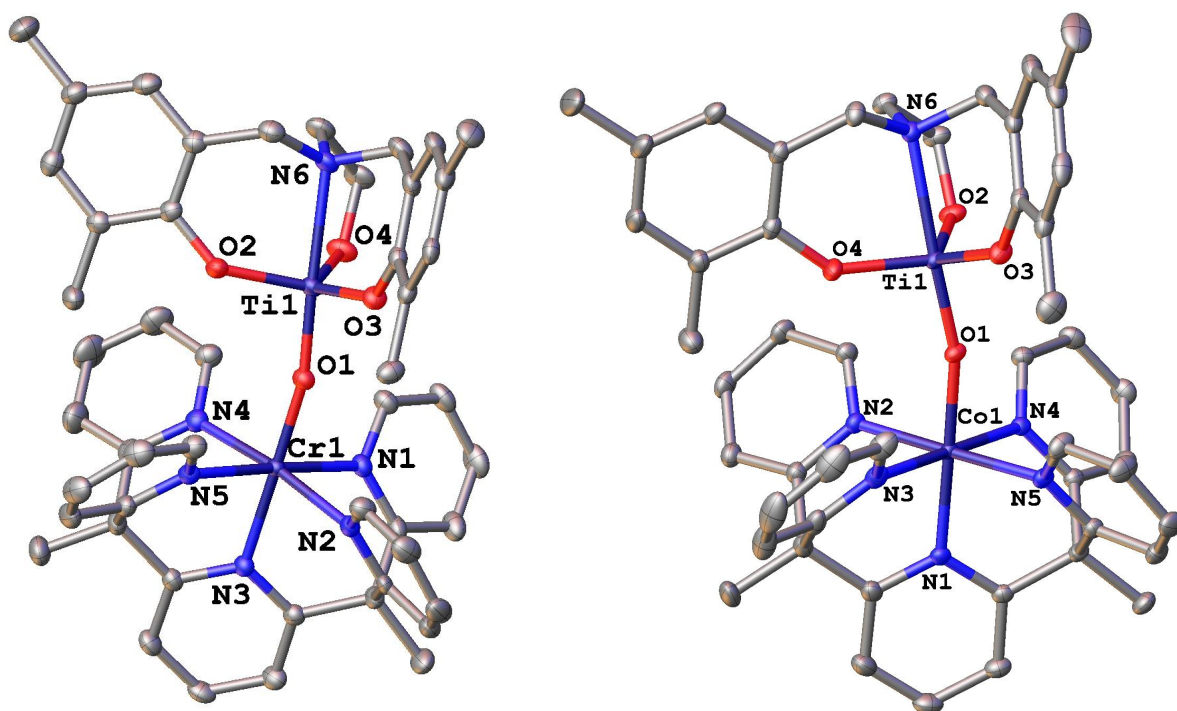


Figure 3.14 X-ray single crystal structures of $\text{Cr}^{\text{III}}\text{OTi}^{\text{IV}}$ and $\text{Co}^{\text{III}}\text{OTi}^{\text{IV}}$ with the omission of hydrogen atoms and counter anions

of $\text{Cr}^{\text{III}}\text{OTi}^{\text{IV}}$ were grown at room temperature under inert conditions via slow vapor diffusion of *n*-pentane into a dichloromethane solution. $\text{Co}^{\text{III}}\text{OTi}^{\text{IV}}$ were grown in a similar fashion, however using acetonitrile as the dissolving solvent.

The covalent bonding interactions through the oxido bridge results in decreased bond lengths and more linear angles than those previously reported from our group.^{24,25} This interaction is largely σ -bonding in nature, however does have a fair amount of π -character, which increases in magnitude as the d-electron count increases (**Figure 3.10**). The coordination environment around each M^{III} center is pseudo- O_h , with a small amount of distortion around each coordinated pyridine. This can largely be attributed to the steric demands of the pentadentate Py_5Me_2 ligand set, and the bridging methylene arms prevent further structural relaxation.

Table 3.3 Select bond lengths and angles obtained through refinement of obtained single crystals for $\text{Cr}^{\text{III}}\text{OTi}^{\text{IV}}$ and $\text{Co}^{\text{III}}\text{OTi}^{\text{IV}}$

Complex	$\text{M}^{\text{III}}\text{-O}$ Bond Length (Å)	$\text{Ti}^{\text{IV}}\text{-O}$ Bond Length (Å)	$\text{M}^{\text{III}}\text{-O-}$ Ti^{IV} Angle (°)	$\text{M}^{\text{III}}\text{-Axial}$ Pyridine Length (Å)	$\text{M}^{\text{III}}\text{-Avg}$ Equatorial Pyridine Length (Å)
$\text{Cr}^{\text{III}}\text{OTi}^{\text{IV}}$	1.850(2)	1.779(2)	166.99(12)	2.076(3)	2.076
$\text{Co}^{\text{III}}\text{OTi}^{\text{IV}}$	1.8513(12)	1.7508(12)	164.13(8)	1.9640(15)	1.975

Table 3.3 displays select bond lengths and angles experimentally obtained for $\text{Cr}^{\text{III}}\text{OTi}^{\text{IV}}$ and $\text{Co}^{\text{III}}\text{OTi}^{\text{IV}}$. The donor $\text{M}^{\text{III}}\text{-oxido}$ bond length remains relatively constant between the two complexes, with a bond length indicative of a covalent interaction between the metal and bridging oxygen. $\text{Ti}^{\text{IV}}\text{-oxido}$ length exhibits a small increase in the Co^{III} complex, however is well within experimental variance and is not of a large enough difference to draw any meaningful conclusions. The same can be said of the $\text{M-O-M}'$ angle across the bridge. With bond angles of 166° and 164° respectively, this linkage is close to a linear 180° angle however does exhibit slight bending. This bend can be seen in previous examples published by Roesky,²⁶ however our molecules exhibit a much smaller effect

compared to their examples. With less sterically demanding ligand sets, Roesky's systems seem to have a larger degree of bending with many molecules exhibiting an approximate angle of 140° across the bridge in their series of molecules. With the Py_5Me_2 and tris-chelate O_3N ligands being much different environments and with the presence of larger and less Lewis acidic transition metals in $\text{Cr}^{\text{III}}\text{OTi}^{\text{IV}}$ and $\text{Co}^{\text{III}}\text{OTi}^{\text{IV}}$, there do not exist many similarities between the two systems aside from the covalent interaction through the oxido bridge. This smaller deviation from linear could be attributed to the strong σ -interactions through the oxido bridge between both metal centers present in both complexes. With both M-O-M' angles of similar values, this small change can be assigned to the increased π -bonding present in $\text{Co}^{\text{III}}\text{OTi}^{\text{IV}}$ due to the increased d-electron count and population of the $d\pi$ orbitals. The contractions of the $\text{M}^{\text{III}}\text{-N}$ bond lengths in the Co^{III} derivative when compared to Cr^{III} can be explain through the expected increase in metal-ligand orbital mixing from the increased electron-richness of the cobalt center when compared to chromium. Although the orbital occupancy of the two metal complexes are similar, the increased stability of electrons on the Co^{III} center are more favorable energetically to mix with the pyridine ligands, resulting in the decrease in observed bond lengths.

It is important to note the spatial distance of each metal center from one another. The through-bond distances between the donor and acceptor metal ions in both $\text{Cr}^{\text{III}}\text{OTi}^{\text{IV}}$ and $\text{Co}^{\text{III}}\text{OTi}^{\text{IV}}$ are measured to be 3.61 and 3.57 Å, respectively. This indicates two covalently linked metal centers through a μ -oxido bridge.²⁷ To our knowledge, molecules containing covalently linked first-row transition metals capable of metal-to-metal charge transfer have never been published prior to our discovery. Revealing a new class of complexes, which have potential applications via harnessing this MMCT chromophore for photochemical reactions.²⁸

3.6 Cited References

- 1) Dunitz, J. D.; Orgel, L. E. *J. Chem. Soc.* **1953**, 2594-2596
- 2) Mathieson, A. M.; Mellor, D. P.; Stephenson, N. C. *Acta Cryst.* **1952**, 5, 185
- 3) Weaver, T. R.; Meyer, T. J.; Adeyemi, S. A.; Brown, G. M.; Eckberg, R. P.; Hatfield, W. E.; Johnson, E. C.; Murray, R. W.; Untereker, D. *J. Am. Chem. Soc.* **1975**, 97, 3039-3048
- 4) Hay, P. J.; Thibeault, J. C.; Hoffman, R. *J. Am. Chem. Soc.* **1975**, 97, 4884-4899
- 5) Veal, J. T.; Jeter, D. Y.; Hempel, J. C.; Eckberg, R. P.; Hatfield, W. E.; Hodgson, D. J., *Inorg. Chem.* **1973**, 12, 2928-2931
- 6) Pedersen, E. *Acta. Chem. Scand.* **1972**, 26, 333-342
- 7) Tatsumi, K.; Hoffman, R. *J. Am. Chem. Soc.* **1981**, 103, 3328-3341
- 8) Burdett, J. K. *Inorg. Chem.* **1978**, 17, 2537-2552
- 9) Reem, R. C.; McCormick, J. M.; Richardson, D. E.; Devlin, F. J.; Stephens, P. J.; Musselman, R. L.; Solomon, E. I. *J. Am. Chem. Soc.* **1989**, 111, 4688-4704
- 10) Kim, Y.; Verkade, J. G. *Organometallics*, **2002**, 21, 2395-2399
- 11) Dargaville, T. R.; De Bruyn, P. J.; Lim, A. S. C.; Looney, M. G.; Potter, A. C.; Solomon, D. H.; Zhang, X. *J. Polym. Sci., Part A: Polym. Chem.* **1997**, 8, 1389
- 12) Sopo, H.; Sviili, J.; Valkonen, A.; Sillanpää, R. *Polyhedron*, **2006**, 25, 1223
- 13) Kol, M.; Shamis, M.; Goldberg, I.; Goldschmidt, Z.; Alfi, S.; Hayut-Salant, E. *Inorg. Chem. Commun.* **2001**, 4, 177
- 14) Lin, W.; Frei, H. *J. Phys. Chem. B* **2005**, 109, 4929
- 15) Lin, W.; Frei, H. *J. Am. Chem. Soc.* **2005**, 127, 1610
- 16) Lin, W.; Frei, H. *C. R. Chimie* **2006**, 9, 207
- 17) Han, H.; Frei, H. *J. Phys. Chem. C* **2008**, 112, 8391
- 18) Han, H.; Frei, H. *J. Phys. Chem. C* **2008**, 112, 16156
- 19) Han, H.; Frei, H. *Microporous Mesoporous Mater.* **2007**, 103, 265
- 20) Kim, W.; Yuan, G.; McClure, B. A.; Frei, H. *J. Am. Chem. Soc.* **2014**, 136, 11034
- 21) Hush, N. S.; Intervalence-Transfer Absorption. Theoretical Considerations and Spectroscopic Data. *Prog. Inorg. Chem.* **1967**, 8, 391

- 22) McClure, B. A.; Frei, H., *J. Phys. Chem. C*, **2014**, *118*, 11601 – 11611
- 23) Hush, N. S. *Trans. Faraday. Soc.* **1961**, *57*, 557
- 24) Goggins, E. M., *Lengthening Charge Transfer Excited States in First Row Transition Metals*. Ph.D. Dissertation, NC State University, Raleigh, NC, **2016**
- 25) Wu, Xinyuan, *Metal-to-Metal Charge Transfer (MMCT) in Heterobimetallic Systems Containing Vanadium (IV)*. Ph.D. Dissertaiton, NC State University, Raleigh, NC, **2016**
- 26) Mandal, S. K.; Roesky, H. W. *Acc. Chem. Res.* **2010**, *43*, 248
- 27) Tielens, F.; Islam, M.; Skara, G.; De Proft, F.; Shishido, T.; Dzwigaj, S. *Microporous Mesoporous Mater.* **2012**, *159*, 66
- 28) Falzone, A. J.; Nguyen, J.; Weare, W. W.; Sommer, R. D.; Boyle, P. D. *Chem. Commun.* **2014**, *50*, 2139-2141

4 Chapter 4: Excited State Dynamics Following Charge Transfer in Oxido Bridged Complexes

4.1 Excited State Dynamics in Six-Coordinate Cr^{III} Complexes

Long-lived excited states in oxido-bridged heterobimetallics have been previously elaborated upon with various examples published by Frei and coworkers. However, there are limited examples of oxido-bridged materials or complexes that contain Cr^{III} as the electron donor and Ti^{IV} as the acceptor.¹ There has been published work extensively investigating the electronic properties of Cr^{III} complexes and their relaxation mechanisms. One of the first examples of this work explored d-d transitions present in various O_h metal complexes, of which many were chromium derived. Most Cr^{III} complexes exist in a quartet (S = 3/2) ground state; with the initial Franck-Condon excited state being the spin-allowed quartet-quartet transition. For d³ O_h complexes without the presence of charge transfer bands, the lowest energy spin-allowed transition is the ⁴A₂ to ⁴T₂ d-d band. Although these complexes do not exhibit charge-transfer character nor do they exhibit a transient species with absorption features, they do undergo spin-crossover to the ²E state, which results in measureable phosphorescence.²

Numerous other reports of investigating additional decay pathways and excited state characteristics have been reported. However, throughout these investigations, phosphorescence from the ²E state remained the dominant feature. Additional non-radiative decay pathways and excited state features have been proposed and explored,³⁻¹³ yet none of them have exhibited strong charge-transfer features and measureable transient features. Changing the stereochemistry of the ligand environment has shown changes in emissive behavior. However, this phenomena has largely been the extent of unique electronic features found in six-coordinate Cr^{III} complexes.

A more recent example has been reported by McDaniel et al. and describes d³ chromium complexes with a hexadentate ligand environment with a large degree of steric tunability. Several of these complexes exhibited characteristic phosphorescence from the ²E state, in addition to strong charge-transfer character and measureable transient absorption

features.¹⁴ These chromium (III) complexes reported revealed μs lifetimes of both phosphorescence and transient components in solution. These complexes do not exhibit strong fluorescence, a characteristic feature for these types of molecules with a saturated coordination environment.

4.2 Charge Transfer Dynamics in CrOH

In order to comprehend excited state dynamics within the heterobimetallic complex $\text{Cr}^{\text{III}}\text{OTi}^{\text{IV}}$, it is important to understand any excited state features present in the monomeric species that comprise these oxido bridged complexes. Chromium (III) complexes should exhibit strong photooxidative properties upon generation of the transient Cr^{IV} species either through electrolysis or photoexcitation, as clarified in **Chapters 2 and 3** in addition to published work by Shores and coworkers.¹³ We propose the photogenerated Cr^{IV} species present in the heterobimetallic complex, $\text{Cr}^{\text{III}}\text{OTi}^{\text{IV}}$, retains the strong redox character, evident by cyclic voltammetry measurements presented earlier. We also propose this heterobimetallic complex exhibits a long-lived charge separated excited state which undergoes relaxation through a non-radiative decay mechanism from a “spin-trapped” MMCT state.

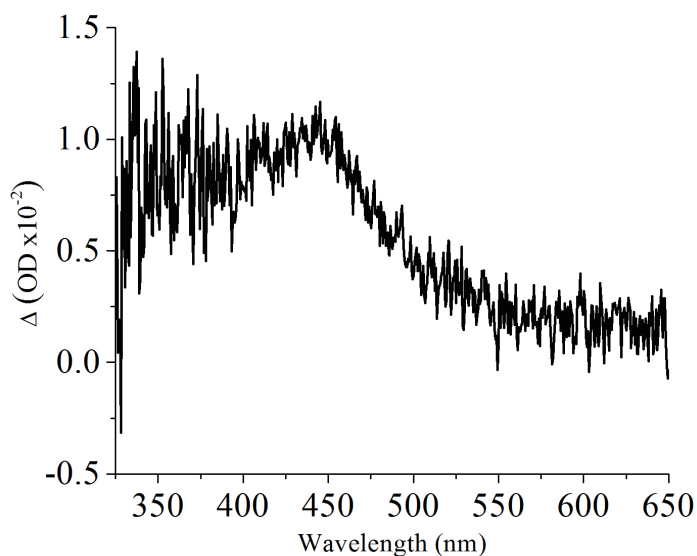


Figure 4.1 Static transient absorption difference spectrum of CrOH taken in DCM following 300 nm excitation at r.t.

Investigation of photophysical properties present in CrOH began with obtaining a transient absorption spectrum in organic solution to further probe any observed properties. Excitation of the blue-edge of the assigned LMCT band present in the CrOH complex was performed at 300 nm on a freshly prepared sample of the complex in dry, spectroscopic grade DCM. **Appendix F** describes the full transient absorption sample preparation and experimental conditions. Following excitation using a ns-laser pulse at 300 nm, there was a measureable transient absorption spectrum with a distinct feature present at 445 nm (**Figure 4.1**). This feature has been tentatively assigned to a transient Cr^{II} charge transfer band to either the oxido ligand or pentadentate Py₅Me₂ ligand. Although the transient signal is noticeably weak with a ΔA of 10^{-2} , its intensity is noticeably stronger than the observed ground state absorption intensity in CrOH due to the absence of a bleach of the broad d-d band present at similar energies. The absence of a ground state bleach signal at higher energies (< 450 nm) is attributed to the lack of absorption features in the ground state complex, as the measured ϵ of the LMCT band at 394 nm is less than $1000 \text{ M}^{-1}\text{cm}^{-1}$.

Fitting the decay signal with nanosecond temporal resolution revealed two distinct time constants, τ_1 and τ_2 , with noticeably different lifetimes. The “short” component of the

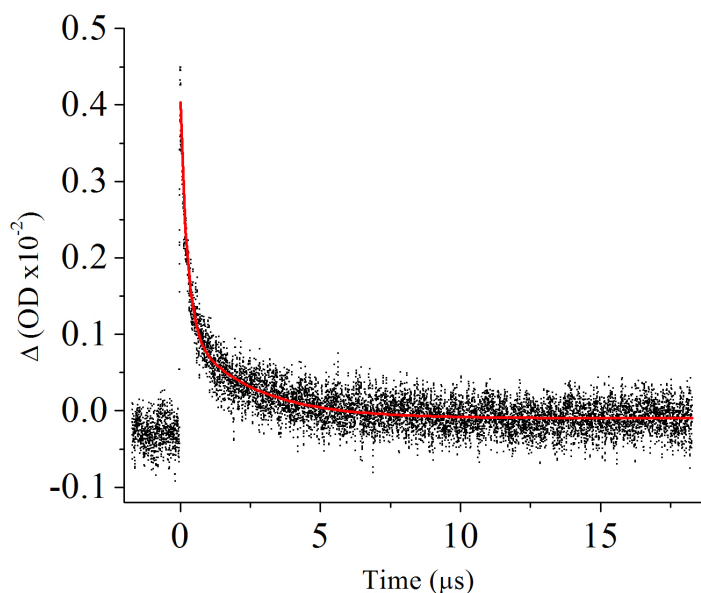


Figure 4.2 Transient decay signal of CrOH at room temperature fitted to a biexponential function. 300 nm excitation wavelength and 475 nm probe wavelength in DCM at room temperature.

decay signal, τ_1 , was found to be 240 ± 6 ns and has a larger pre-exponential A term of the decay fit than the long component. The long-lived state, measured as τ_2 , was found to have a lifetime of 2.3 ± 0.1 μ s in DCM solution at room temperature. Introducing air to the sample did not have a noticeable effect to the transient decay signal intensity or lifetime. Effects from atmospheric oxygen were not anticipated due to the absence of an excited state triplet formation possibility, however for experimental completeness this was a necessity. The relative contributions of each time constant to the decay signal were not equivalent, evident by the difference in signal intensities. Relative contributions of the two excited states can be explored by comparing the pre-exponential A terms of each time constant. The pre-exponential factor of τ_1 was found to be 0.00294, almost twice that of τ_2 (0.00119). Thus, the shorter lived state contributes more to the decay signal than the long-lived 2.3 μ s state.

Pump wavelength variance experiments revealed both the short and long lived components of the transient decay are affected equally when probing the absorption feature (475 nm). Although the intensity of the A term exponential fits do not trace any resolved band in the ground state absorption feature present in CrOH, their consistencies as a result of varying the excitation wavelength are evident. Exciting the resolved LMCT band at 394 nm

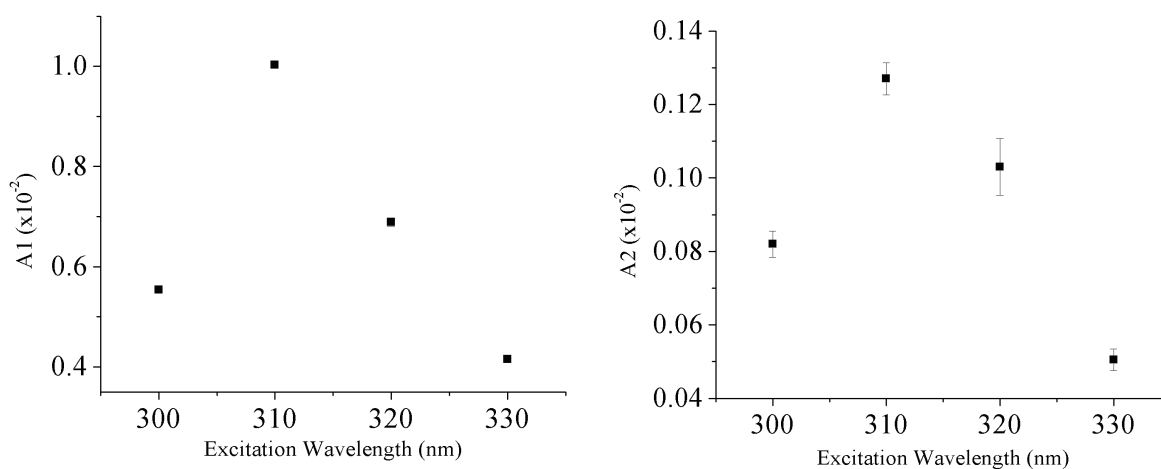


Figure 4.3 Pump wavelength dependence plot of the transient absorption feature in CrOH. Nanosecond component (left) and microsecond features (right) depicted above

did not result in a signal for the decay kinetics, nor did any excitation wavelength below 330 nm. This suggests the internal conversion present in CrOH after the generation of the Franck-

Condon state is nominally efficient. However, this does require a small amount of excess energy in order to access the excited state manifold from which the absorption feature at 445 nm is derived. Due to non-ideal signal-to-noise ratios, variance of the probe wavelength did not provide any useful information. However varying the probe wavelength it was found that a 475 nm setting resulted in data with the best spectral resolution, notwithstanding the

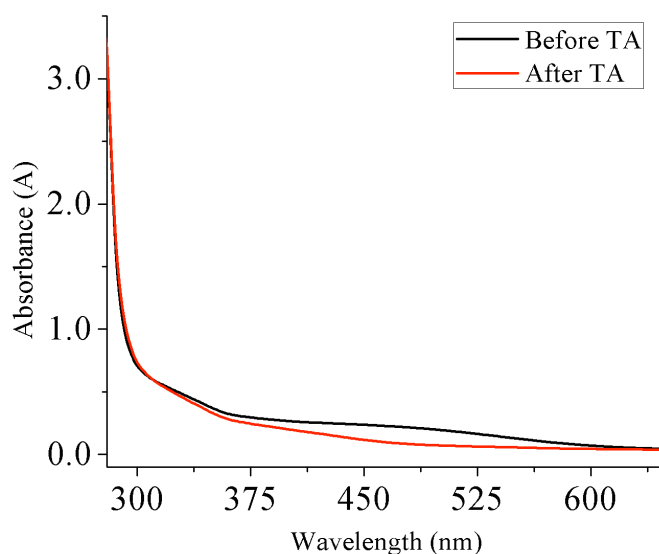


Figure 4.4 EAS of CrOH after 50 excitations to obtain room temperature kinetics

transient absorption feature at 445 nm.

Although a transient absorption feature is evident, and with measureable intensity to obtain kinetic information, the overbearing photodecomposition present in CrOH prevents us from obtaining additional excited state information such as energy of activations or long-term stability studies. **Figure 4.4** depicts the ground state electronic absorption spectrum of the CrOH sample that was utilized to obtain nanosecond kinetics with 300 nm pump and 475 nm probe settings. There is a decrease in the charge transfer bands present from 375 – 500 nm, in addition to the d-d band intensity at 549 nm following 50 excitation scans needed to obtain kinetic data with an acceptable S/N ratio (**Figure 4.4**). The observed photodecomposition in CrOH also prevented the obtainment of a spectral map of the transient absorption feature at

445 nm. Without this data, we are unable to assign the transient absorption feature to a particular component of the bi-exponential decay.

While investigating observed transient absorption features in CrOH and the observation of a μ s-long lifetime at room temperature, there was noticeable emission present

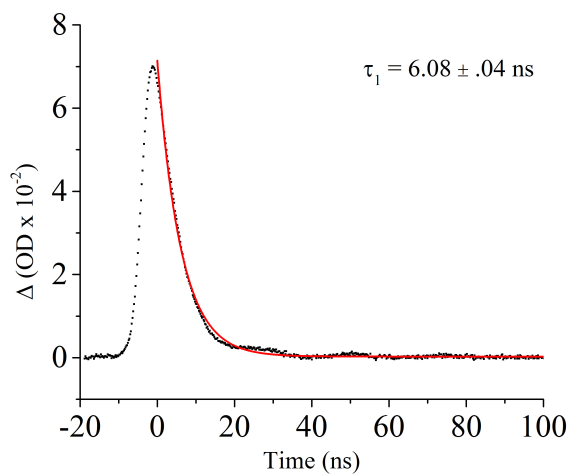


Figure 4.5 Fluorescence decay kinetics of CrOH in a degassed solution of dry DCM at room temperature

following excitation. This was to be expected, as the previously demonstrated examples of Cr^{III} complexes exhibit moderate phosphorescence in addition to measureable fluorescence intensities. Standard fluorescence measurements were taken of CrOH in DCM with a 300 nm excitation wavelength. Due to significant photodecomposition of CrOH, quantitative emission quantum yields were not obtainable. However, a distinct emission peak at 367 nm was evident in the static emission spectrum (**Appendix F**). Following correction of the emission spectrum and varying the excitation wavelength, there were no additional peaks in the fluorescence spectrum. Due to the energy of the emission following 300 nm excitation, this observed peak is unlikely to be the result of phosphorescence. In order to further confirm this assignment of fluorescence from the initially generated ⁴LMCT₁ state, the emission lifetime was obtained. Resolved emission kinetics data was obtainable, which revealed a lifetime of 6.08 ± 0.04 ns at room temperature fitted to a single exponential decay function. This observation further supports our assignment as a spin-allowed emission from the quartet state. Investigation of the TiOⁱPr monomeric complex did not reveal any

measurable emission or transient absorption features with nanosecond temporal resolution. The TiO⁺Pr complex likely exhibits transient kinetics on the ultrafast timescale, however the investigation of these features has yet to be explored.

Utilizing the transient absorption data and emission kinetics allows us to present an approximate relaxation mechanism in CrOH following UV excitation. **Figure 4.6** depicts the proposed Jablonski diagram of measured spectroscopic properties measured of CrOH with nanosecond temporal resolution. Due to the energetic requirements for charge transfer in CrOH, ultrafast transient absorption data could not be obtained as no measurable signal was detected with excitation wavelengths lower than 330 nm. After the population of the initial Franck-Condon state, we propose there exists an intersystem crossing event, which is characteristic of six-coordinate Cr^{III} complexes.²⁻¹⁴ Emission from this ⁴LMCT₁ state competes with the non-radiative decay manifold, evident by the measurable fluorescence with a lifetime of 6.08 ns at room temperature (τ_F). No measurable phosphorescence was detected, therefore non-radiative decay pathways through vibrational relaxation is preferred from the proposed doublet states.

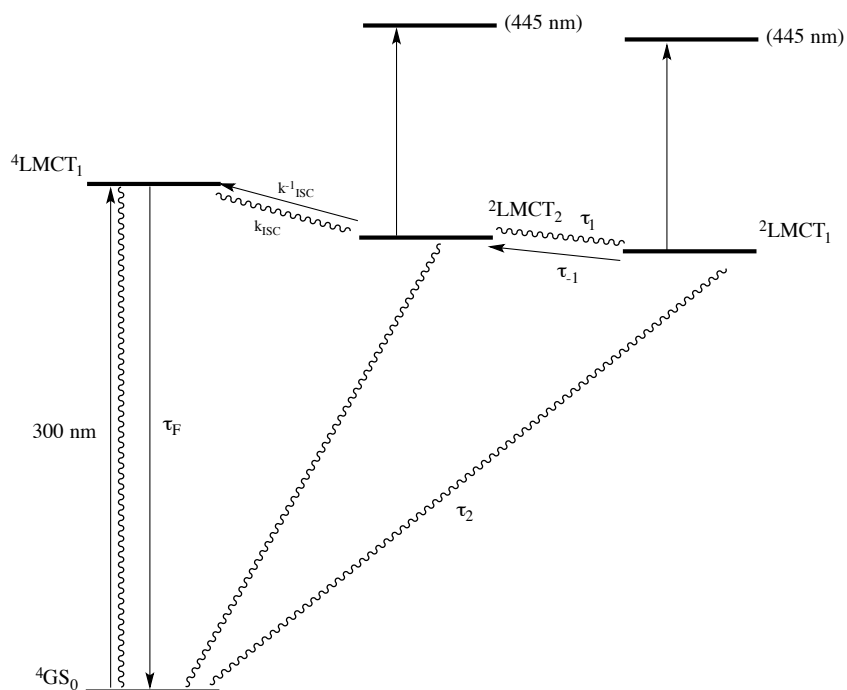


Figure 4.6 Proposed Jablonski diagram of CrOH following 300 nm excitation with nanosecond temporal resolution.

Since intersystem crossing in transition metal complexes occurs on the ultrafast timescale, this component of the relaxation mechanism is unable to be resolved given the available instrumentation. However, due to the strong precedence in analogous systems this assignment can be made with conviction. The transient absorption feature is evident at short time delays, suggesting its feature originates from the initially accessed ${}^2\text{LMCT}_2$ state. While a time-resolved spectral map was not obtained due to the photodecomposition of the transient species, the intensity of this spectral feature is diminished at longer time delays (**Appendix F**). This suggests this absorption feature originates from the relatively short-lived component ${}^2\text{LMCT}_2$, with a lifetime of 240 ns (τ_1). However, lack of resolved transient features means we cannot rule out the possibility of contribution from the long-lived ${}^2\text{LMCT}_1$ state measured at 2.3 μs (τ_2).

While conclusive evidence describing the nature of this long-lived state has proven to be elusive, its likely origin is the initially generated ISC-accessed state due to the rapid kinetics of such an event. Signal-to-noise ratios of the transient absorption spectrum at longer time delays show a noticeable decrease in absorption intensity. However, contributions from the ${}^2\text{LMCT}_1$ state cannot be ruled out. One possible contributor in the formation of this long-lived state is pseudo Jahn-Teller distortion, resulting in additional structural distortions from ${}^2\text{LMCT}_2$. Since both contributions to non-radiative decay have relatively long lifetimes, both are proposed to undergo spin-forbidden relaxation. Also contributing to the excited state lifetime is the poor electronic coupling following excitation, due to relaxation of the excited electron into an orthogonal orbital with different symmetry. We have assigned this transition as hydroxide \rightarrow Cr^{III} charge transfer, which is largely σ -in nature due to the orbitally forbidden nature of a π -manifold transition into the d_{xz}/d_{yz} degenerate set. The d_{z^2} orbital lies higher than the vacant $d_{x^2-y^2}$ orbital, providing a weakly coupled, orthogonal orbital that is accessed through vibronic relaxation. Without ultrafast resolution of the transient species, the conclusive assignment of such an event is absent. However, it is a plausible explanation for the spectroscopically observed long-lived excited states not normally present in first row transition metal complexes.

4.3 Excited State Dynamics in $\text{Cr}^{\text{III}}\text{OTi}^{\text{IV}}$: Evidence for Indirect MMCT

The initial mechanism previously proposed before investigating the photophysics in these heterobimetallic complexes was largely based off those published in Frei's solid-state systems on mesoporous silica. Following direct excitation of the MMCT chromophore, the charge transfer state has little organic ligand contribution (oxido bridge) and almost entirely metal-based. However, upon investigating the CrOH complex and revelation of a long-lived charge transfer state, this proposal of a similar mechanism needed to be revisited. Following our findings of new electronic absorption features in $\text{Cr}^{\text{III}}\text{OTi}^{\text{IV}}$ and the assignment of a newly formed MMCT at 288 nm upon introduction of the donor-bridge-acceptor structure,¹⁵ we now have an absorption feature to probe with nanosecond temporal resolution. Due to experimental limitations, the excitation threshold is confined to 300 nm and will be the wavelength of choice for probing the MMCT band present in the oxido bridged complex. Provided there is sufficient orbital overlap, vibronic coupling should sufficiently populate the MMCT Franck-Condon state. The initially proposed mechanism following MMCT is depicted in **Figure 4.7** in which the ${}^4\text{LMCT}_1$ state present in CrOH is lower-lying in energy

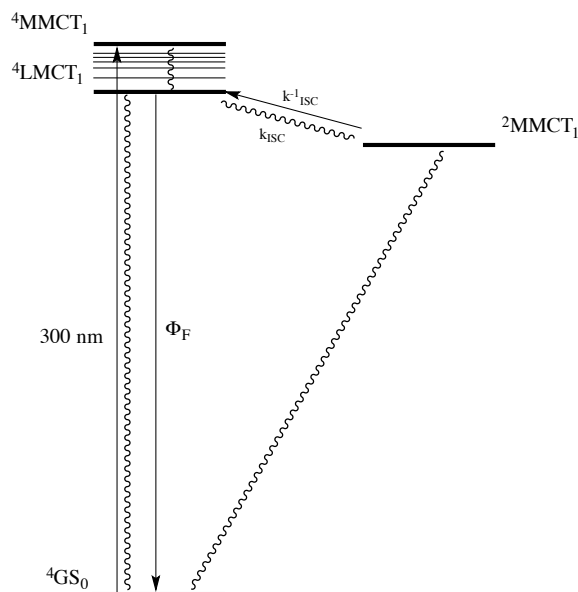


Figure 4.7 Initially proposed mechanism for $\text{Cr}^{\text{III}}\text{OTi}^{\text{IV}}$ following direct MMCT excitation.

than the $^4\text{MMCT}_1$ state due to its lower energetic requirements (312 nm). As a result of weak, but measurable fluorescence in CrOH, we expect there to be weak spin-allowed emission present in the heterobimetallic complex as well. Along with this proposal, we do not expect to observe any phosphorescence from the $^2\text{MMCT}_1$ state following intersystem crossing.

The excited state difference spectra revealed two distinct absorption bands of similar intensities (**Figure 4.8**), one centered at 360 nm and the other at 485 nm. Just as was seen in the CrOH transient absorption spectrum in **Figure 4.1**, the ground state bleach signal is not

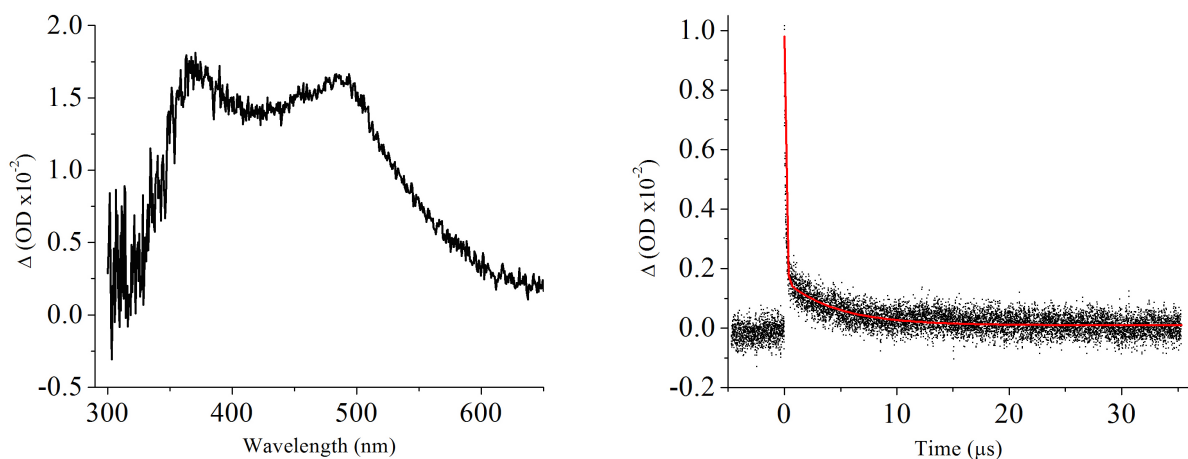


Figure 4.8 Static transient absorption spectrum of $\text{Cr}^{\text{III}}\text{OTi}^{\text{IV}}$ in dichloromethane solution (left) and room temperature transient decay kinetics (right).

observable. This absence can again be attributed by the weak absorption features in the ground state complex at energies greater than 350 nm. The weak signal present at 305 nm in the transient absorption spectrum may be the onset of the ground state bleach. However, due to instrumental limitations this assignment is not conclusive. The assignment of the higher-energy band at 350 nm has been attributed to a charge transfer band that is likely LMCT in nature due to the generation of an assigned transient $\text{Cr}^{\text{IV}}\text{OTi}^{\text{III}}$ species. The absorption feature at 485 nm has been assigned as a transient d-d transition localized on the transient Ti^{III} center, and is consistent with previous reports of electronic characteristics observed in photogenerated d^1 metals.^{16, 17} Fitting the room temperature absorption decay kinetic data with a bi-exponential function revealed two-components signal with distinct time constants (**Figure 4.8**). The shorter component has an excited state lifetime of 103 ± 2 ns, shorter than

the nanosecond-timescale component present in CrOH. The second and long-lived state accessed in this oxido bridged complex was found to have a lifetime of $4.6 \pm 0.1 \mu\text{s}$ at room temperature, again different from that seen in the CrOH parent complex (**Appendix F**).

Analysis of the pre-exponential A term for the bi-exponential decay function revealed a dis-proportionate contribution of the two states, with the short component dominating the signal. This $A_1:A_2$ ratio is almost 6:1 in favor of the short lived state (.0089 to .0015), indicates the decreased accessibility of the long-lived $4.6 \mu\text{s}$ state, measured as τ_2 . Our initial proposal following obtaining this data includes two absorption features in the static difference spectrum each corresponded to a different state, with the lower-energy band at 485 corresponding to the long-lived $4.6 \mu\text{s}$ state. In order to confirm this assignment, it was necessary to obtain the time-dependent spectral map of the transient species to view changes over time with nanosecond resolution.

As seen in **Figure 4.9**, the relative intensity of the two absorption features remains consistent throughout the time delays measured considering the S/N ratio. This would

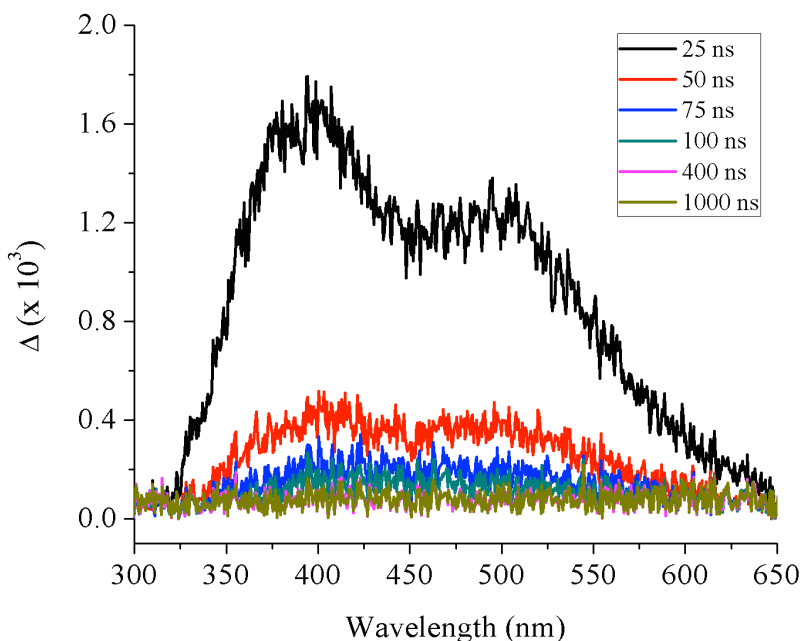


Figure 4.9 Spectral map of $\text{Cr}^{\text{III}}\text{OTi}^{\text{IV}}$ in DCM at room temperature with ns temporal resolution.

suggest the two absorption features originate from the same excited state, given the large difference in lifetimes of the two components. After approximately 100 ns, the transient absorption features seem to be absent, suggesting these two absorption features originate from the short-lived component. However, when taking the S/N ratio into account as well as the relative contribution of each decay constant to the kinetics intensity, it is highly likely that if the long-lived state does have a characteristic absorption band it may be unobservable given the experimental limitations probing such a feature. To probe the presence of any transient absorption features present at each of the decay constants, it was necessary to perform a probe-dependence intensity analysis of each component (**Figure 4.10**).

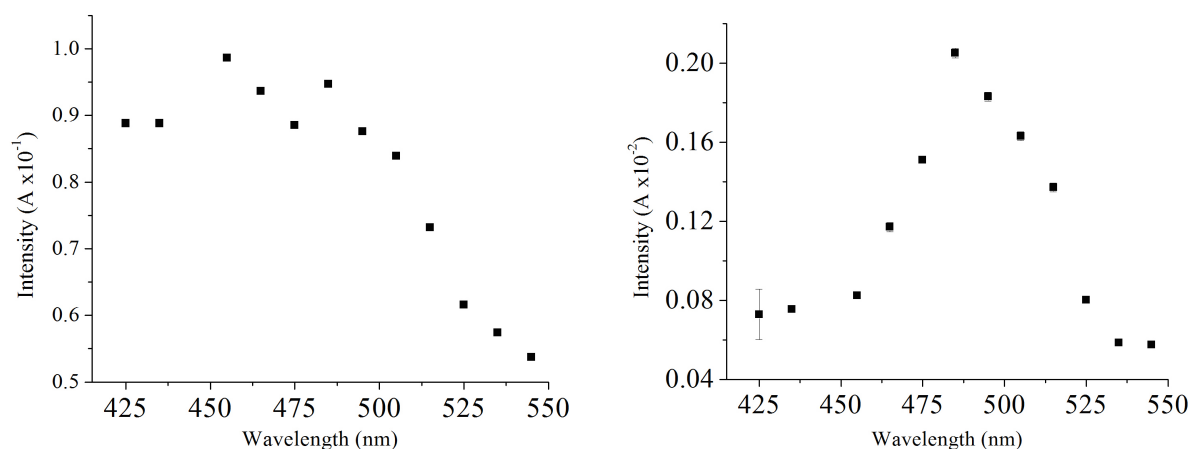


Figure 4.10 Plot of the experimentally obtained decay fit A terms of τ_1 (left) and τ_2 (right) with 300 nm excitation.

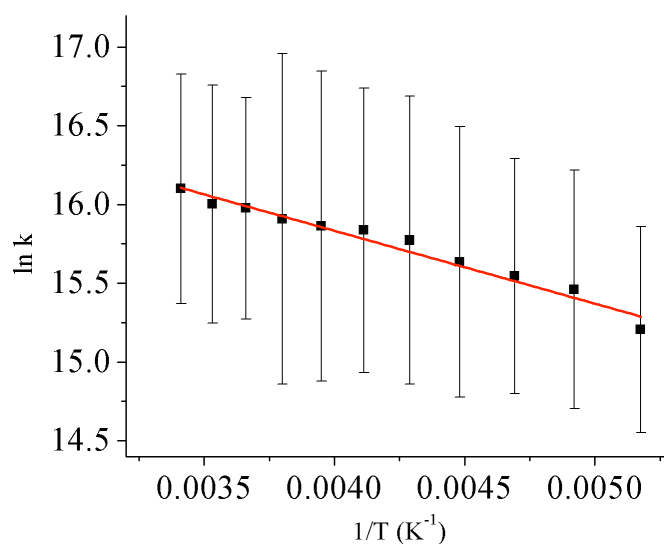


Figure 4.11 Arrhenius plot of the short component, τ_1 , in DCM

In the short-component probe dependence plot, the relative intensity of the pre-exponential A term resembles both the lower energy band at 485 nm in addition to maintain high intensity moving towards the higher energy band at approximately 360 nm. This would suggest that both absorption features are present in the excited state measured by τ_1 at 103 ns. The long-component probe plot has noticeable differences, starting with the relative intensity of the pre-exponential term. Previously demonstrated within this document, the room temperature kinetics data (300 nm pump and 475 nm probe) revealed a significantly smaller τ_2 contribution than τ_1 , which is evident in **Figure 4.10**. Not only is the intensity of the A term significantly lower than that of the shorter component, its contribution decreases moving away from the λ_{max} at 485 nm. Transient decay kinetics with probe wavelengths greater than 545 nm and less than 425 nm resulted in fitted exponential curves with a large degree of error and thus omitted from **Figure 4.10**. As a result of the information obtained from these two probe-dependent plots, it can be reasonably concluded that there does exist a transient feature centered at approximately 485 nm, from which τ_2 is obtained. Due to its weak signal compared to the short component represented by τ_1 , its presence in the static transient absorption spectra is not readily apparent.

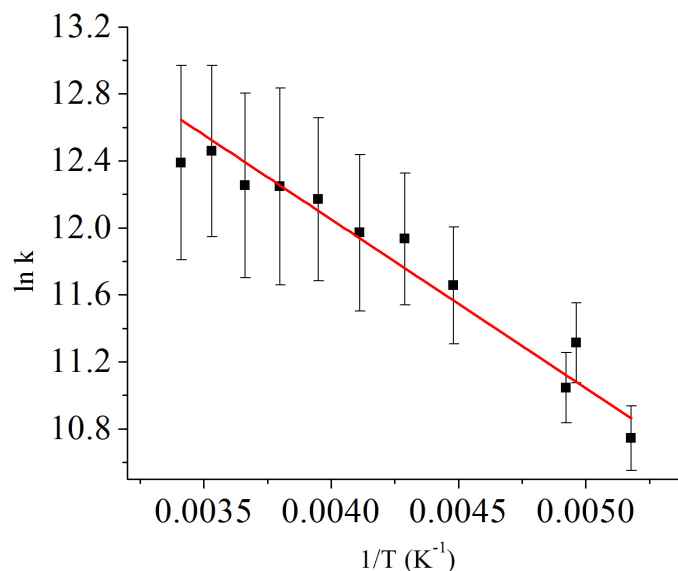


Figure 4.12 Arrhenius plot of τ_2 in $\text{Cr}^{\text{III}}\text{OTi}^{\text{IV}}$ depicting a linear temperature dependence of the long-lived state.

Variable temperature experiments were performed on $\text{Cr}^{\text{III}}\text{OTi}^{\text{IV}}$ on the nanosecond timescale from 20 °C to -80 °C in order to obtain the thermodynamic parameters for back electron transfer. For the short component τ_1 , a linear relationship in the Arrhenius plot was obtained (**Figure 4.11**). However, due to the large error present in the resulting plot, no quantitative conclusions can be made about the E_A for this component. However when comparing the slopes of the linear Arrhenius plots in τ_1 to that of τ_2 , it can be stated that it has a smaller thermal dependence than that seen of τ_2 (**Figure 4.12**). The energy of activation for the long-lived state (τ_2) was found to be 2.09 kcal/mol, relatively small for an excited state with a microsecond lifetime. This suggests the nature of the long-lived state is electronic in nature, and very weakly coupled with the ground state. The initial coupling to the Franck-Condon state presented in **Chapter 3**, was calculated at 5597 cm^{-1} . Due to the modest electronic coupling to this initial excited state and the two-component excited state decay coupled with a proposed spin-crossover event, a weakly coupled excited state is likely to be the lowest-lying state, measured as τ_2 .

$\text{Cr}^{\text{III}}\text{OTi}^{\text{IV}}$ was also found to be emissive, and unlike the parent complex CrOH, exhibits photostability even after hundreds of excitations at 300 nm. Therefore, it was possible to obtain a fluorescence quantum yield unlike that of CrOH. The static emission

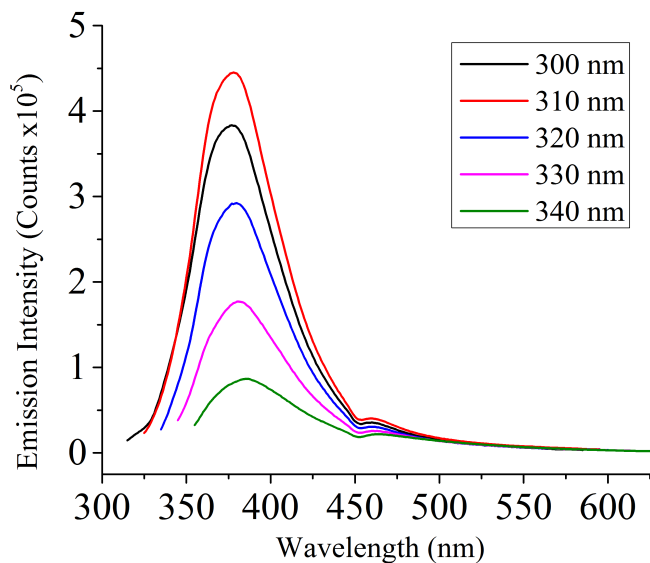


Figure 4.13 Uncorrected static emission spectra of $\text{Cr}^{\text{III}}\text{OTi}^{\text{IV}}$ with a Φ_{F} of .009 (vs. Anthracene)

spectra and obtained quantum yield can be seen in **Figure 4.13**. No shift in the energy of the emission band was seen upon varying the excitation wavelength, eliminating the possibility of the observed emission being solvent-based or Raman scattering. Experimental details and corrected emission spectra can be seen in **Appendix G**. The fluorescence lifetime of this observed emission was found to be 6.67 ns at room temperature, and is centered at 383 nm. Exponential fitting of the emission lifetime can also be found in **Appendix G**. Both of these parameters are in-line with that seen in CrOH , however there is an increased Stokes-shift of the emission band in the heterobimetallic complex in addition to the slightly lengthened emissive lifetime. Due to their similar characteristics it can be reasonably suggested that this emission seen in both complexes originate from the same state. The absence of observed phosphorescence in $\text{Cr}^{\text{III}}\text{OTi}^{\text{IV}}$ in addition to the lifetime obtained suggests this feature to be spin-allowed emission. With these parameters taken into account, an excited state model can be presented keeping in mind the limitations of nanosecond-temporal resolution.

After comparing the data obtained from CrOH and $\text{Cr}^{\text{III}}\text{OTi}^{\text{IV}}$ it is apparent they share some characteristics, yet have significant differences as well. It is likely that exciting the dimer at 300 nm, we are not able to directly excite into the $^4\text{MMCT}_1$ state, even with vibronic

center, which does not have degeneracy due to the asymmetry present in the oxido bridged complex (C_1). This excited state with an $S = 1/2$ electronic configuration is proposed to have a lifetime extension through magnetic superexchange via the diamagnetic oxido bridge between the transient Ti^{III} and Cr^{IV} centers. Such exchange between cationic metals is prevalent in other metal-oxide containing materials such as manganese oxide, and has also been strongly favored in an analogous solid-state system containing a transient Mn^{III}/Ti^{III} following direct MMCT.¹⁷ This proposed mechanism supported by our nanosecond temporal resolution transient absorption data is depicted in **Figure 4.14**.

In order to confirm our proposal for a weakly coupled long-lived excited state, it is necessary to calculate the electronic coupling constant for the long-lived state, H_{ABkin} .¹⁷ Calculating the reorganization energy, λ , from the $E_{1/2}$ for the redox processes at each metal center must be done initially. ΔG° is approximated as the difference in eV between the $Cr^{III/IV}$ oxidation and $Ti^{IV/III}$ reduction, obtained by cyclic voltammetry, at 4.24 eV. This can then be substituted into **Equation 4.1**, which relates the E_A obtained by the Arrhenius plot to the reorganization energy, λ .

$$\text{Equation 4.1 } E_A = \frac{\lambda}{4} \left(1 + \frac{\Delta G^\circ}{\lambda} \right)^2$$

Solving for λ gives a value of 130 kcal/mol using the energy of activation for the long-lived state, τ_2 . The overall reorganization energy of the system is larger than the short-lived component is not taken into account. However, due to the uncertainty resulting from such a calculation this cannot be quantitatively factored into calculated parameters, however must be acknowledged. Once the reorganization energy has been calculated, it is now possible to calculate H_{ABkin} (**Equation 4.2**) by substituting in the pre-exponential A-term from the Arrhenius plot ($9.69 \times 10^6 \text{ s}^{-1}$).

$$\text{Equation 4.2 } H_{ABkin} = \sqrt{\frac{A\hbar\sqrt{4\pi\lambda RT}}{2\pi}}$$

Solving for H_{ABkin} results in a coupling constant of $1.21 \times 10^{-12} \text{ cm}^{-1}$ which is much smaller than reported by Frei et al.,¹⁸ and is an order of magnitude less than that seen in other molecular systems which have μs -lifetimes at room temperature.¹⁶ This extremely small coupling constant value confirms our assignment of a weakly coupled long-lived excited state, evident by the $4.6 \mu\text{s}$ lifetime in dichloromethane.

4.4 Excited State Characterization of $\text{Fe}^{\text{III}}\text{OTi}^{\text{IV}}$: An Iron-Based Molecule with a Nanosecond Lifetime

Due to the difference in electronic structure of the iron heterobimetallic derivative, we expected to observe an excited state lifetime much different than that seen in $\text{Cr}^{\text{III}}\text{OTi}^{\text{IV}}$. With the $\text{Fe}^{\text{III}}\text{OTi}^{\text{IV}}$ containing two additional d-electrons in an $S = \frac{1}{2}$ ground state, the intersystem crossing following excitation as described in **Section 4.3** is not to be expected. We propose the lack of a spin-forbidden relaxation pathway could result in a shorter lifetime following excitation of the MMCT transition in $\text{Fe}^{\text{III}}\text{OTi}^{\text{IV}}$. The fitted MMCT band in this complex is 478 nm, which we are able to directly excite. This is unlike the increased energy requirements in $\text{Cr}^{\text{III}}\text{OTi}^{\text{IV}}$, which may have affected the accessed excited state manifold.

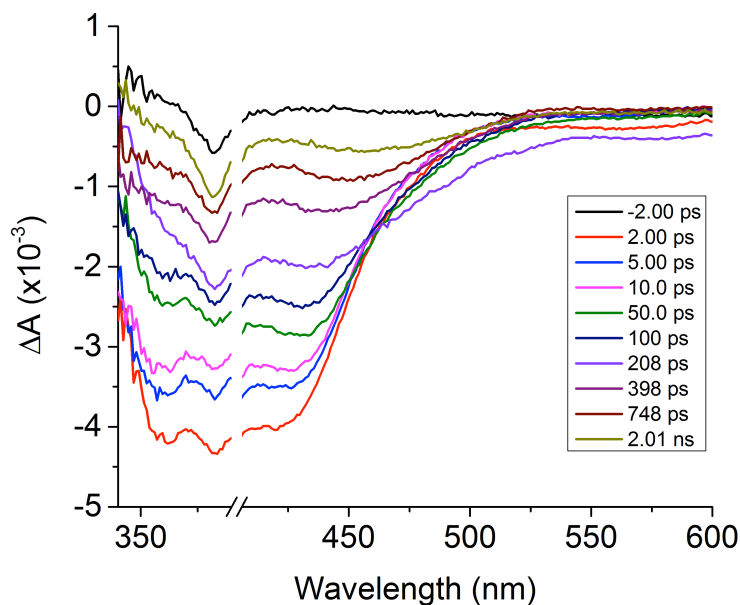


Figure 4.15 Spectral Map of $\text{Fe}^{\text{III}}\text{OTi}^{\text{IV}}$ with picosecond temporal resolution. No transient features were observed however the ground state bleach is evident.

Excitation with picosecond temporal resolution of $\text{Fe}^{\text{III}}\text{OTi}^{\text{IV}}$ was at 400 nm in dry, spectroscopic grade dichloromethane.

Figure 4.15 depicts the changes in the transient spectrum over time, and did not reveal any measureable excited state absorption features. However, there is a strong ground state bleach signal, which allows a kinetic analysis of the transient species. The defined shoulder at approximately 380 nm is signal attributed to the laser, evident before time zero in addition to the relative intensity remaining constant over time. Strong contribution from the excitation source is evident from 390 nm to 406 nm and has been omitted from **Figure 4.15**. As seen in the ground state absorption spectrum of $\text{Fe}^{\text{III}}\text{OTi}^{\text{IV}}$ (**Appendix B**), there are broad overlapping absorption bands from 350 – 550 nm in solution. This characteristic manifests itself in the observed ground state bleach in the ΔA spectrum in **Figure 4.15**. The bleach recovery is complete, suggesting there is no measureable intensity from any photogenerated side-products. The lack of a transient absorption feature can be attributed to the strong absorption features in $\text{Fe}^{\text{III}}\text{OTi}^{\text{IV}}$ at wavelengths greater than 350 nm, which is contrary to that seen in $\text{Cr}^{\text{III}}\text{OTi}^{\text{IV}}$. Due to the MMCT character of the fitted absorption feature at 478 nm, a transient Ti^{III} species is to be expected and has a characteristic band near 485 nm.

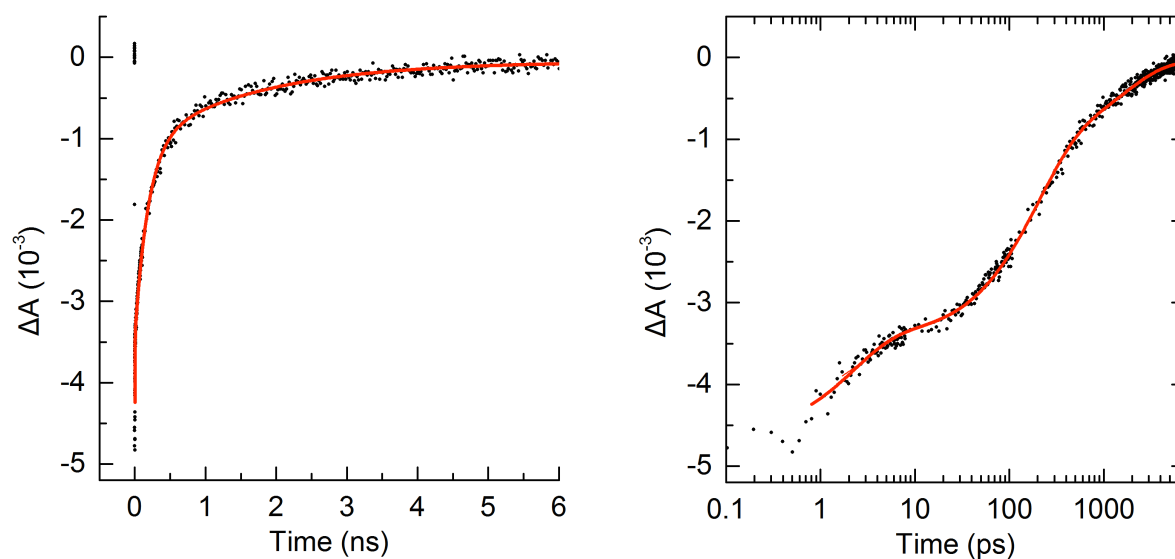


Figure 4.16 Bleach recovery kinetics with picosecond temporal resolution depicted with both linear (left) and log (right) plots. The overall decay signal contains three components, with the long-lived stated having a lifetime of 1.8 ns.

Despite the potential presence of this transient absorption feature, it is expected to be weaker than the ground state absorption intensity in $\text{Fe}^{\text{III}}\text{OTi}^{\text{IV}}$, which may explain the lack of any transient features in this complex. Nevertheless, excited state lifetimes were obtained for the transient $\text{Fe}^{\text{IV}}\text{OTi}^{\text{III}}$ species using the bleach recovery signal (**Figure 4.16**).

The bleach recovery data was fitted to a triexponential function with a large degree of confidence ($R^2 = .99762$), and is depicted in **Figure 4.16** with both linear and log plots to reveal the goodness of fit. The small amount of oscillating signal at times shorter than 1 ps could be included with an additional time constant fit. However, due to the possibility of over parameterizing the excited state dynamics this was not included. The shortest component of the decay signal, τ_1 , has a lifetime of 2.86 ± 0.29 ps and can be attributed to ultrafast vibrational relaxation following the Franck-Condon state generation. A longer lived state, τ_2 , is then accessed and has lifetime of 196 ± 6 ps. This then relaxes to the long-lived MMCT state, $\tau_3 = 1.8 \pm 0.2$ ns. This short excited state lifetimes in $\text{Fe}^{\text{III}}\text{OTi}^{\text{IV}}$ is accredited to the lack of a spin-forbidden relaxation pathway, as the excited state conserves the $S = 1/2$ electronic configuration. Although the lifetime of $\text{Fe}^{\text{III}}\text{OTi}^{\text{IV}}$ is significantly shorter than the chromium derivative, it is a rare example of an iron-containing molecule with a long-lived transient species (> 1 ns). This long-lived excited state is attributed to the MMCT nature of the complex, which avoids ligand field deactivation of the excited state through the localization of the excited electron on the transient Ti^{III} center.

4.5 Cited References

- 1) Han, H.; Frei, H., *J. Phys. Chem. C*, **2008**, *112*, 8391 - 8399
- 2) Castelli, F.; Forster, L. S., *J. Phys. Chem.* **1977**, *81*, 403 – 408
- 3) Lessard, R. B.; Endicott, J. F., *Inorg. Chem.* **1992**, *31*, 3091 - 3103
- 4) Grisenti, D. L.; Smith, M. B.; Fang, L.; Bishop, N.; Wagenknecht, P. S., *Inorg. Chim. Acta*, **2010**, *363*, 157 -1 62
- 5) Asano, M.; Koningstein, J. A.; Nicollin, D., *J. Chem. Phys.*, **1980**, *73*, 688 – 696
- 6) Brown, K. N.; Geue, R. J.; Moran, G.; Ralph, S. F.; Riesen, H.; Sargeson, A. M., *Chem. Commun.*, **1998**, 2291 – 2292
- 7) Neshvad, G.; Hoffman, M. Z.; Bolte, M.; Sriram, R.; Serpone, N., *Inorg. Chem.*, **1987**, *26*, 2984 – 2988
- 8) Ryu, C. K.; Endicott, J. F., *Inorg. Chem.*, **1987**, *27*, 2203 – 2214
- 9) Vagnini, M. T.; Kane-Maguire, N. A. P.; Wagenknecht, P. S., *Inorg. Chem.*, **2006**, *45*, 3789 – 3793
- 10) Grisenti, D. L.; Thomas, W. W.; Turlington, C. R.; Newsom, M. D.; Priedemann, C. J.; VenDerveer, D. G.; Wagenknecht, P. S., *Inorg. Chem.*, **2008**, *47*, 11452 – 11454
- 11) Linck, N. J.; Berens, S. J.; Magde, D.; Linck, R. G., *J. Phys. Chem.*, **1983**, *87*, 1733 – 1737
- 12) Endicott, J. F.; Tamilarasan, R.; Lessard, R. B., *Chem. Phys. Lett.*, **1984**, *112*, 381 – 386
- 13) Ramasami, T.; Endicott, J. F.; Brubaker, G. R., *J. Phys. Chem.*, **1983**, *87*, 5057 – 5059
- 14) McDaniel, A. M.; Tseng, H. W.; Hill, E. A.; Damrauer, N. H.; Rappe, A. K. Shores, M. P., *Inorg. Chem.*, **2013**, *52*, 1368 – 1378
- 15) Falzone, A. J.; Nguyen, J.; Weare, W. W.; Sommer, R. D.; Boyle, P. D., *Chem. Commun.*, **2014**, *50*, 2139 – 2141
- 16) Goggins, E. M., *Lengthening Charge Transfer Excited States in First Row Transition Metals*. Ph.D. Dissertation, NC State University, Raleigh, NC, **2016**
- 17) Cuk, T.; Weare, W. W.; Frei, H., *J. Phys. Chem. C*, **2010**, *114*, 9167

18) McClure, B. A.; Frei, H., *J. Phys. Chem. C*, **2014**, *118*, 11601 - 11611

5 Chapter 5: Advancements in the Understanding of Atom Transfer Reactivity in Manganese (III) Porphyrin Complexes

5.1 An Introduction to Oxygen Atom Transfer Chemistry in Mn (III) Complexes

This work presented herein aims to expand on developments made by previous group member, Dr. Tao Huang.¹ In his thesis, it was discovered that cationic metalloporphyrins, specifically Mn^{III} TPP-based porphyrins, catalyze oxygen-atom transfer reactions in the formation of epoxides. Not only do these catalysts transform most substrate (> 90%), but when the parent olefin exhibits *cis* stereochemistry, these manganese porphyrins favor the corresponding *cis*-epoxide. This ability to perform oxygen-atom transfer chemistry with an Earth-abundant metal such as manganese in addition to a ligand set that offers a large degree of tunability reveals the immense potential for such a system.

Oxygen atom transfer chemistry utilizing Manganese-based catalysts is not a new area of interest, with Mn (III) salen complexes being extensively studied by Jacobsen et al.²⁻⁴ The epoxidation of alkenes using metalloporphyrins has been demonstrated previously, with Mn, Fe, and Cr based complexes all exhibiting tunable reactivity.⁵ This work aims to use tetraphenylporphyrin (TPP) as the supporting ligand environment around the Mn^{III} center due to its biological relevance and large degree of tunability. Varying the electronic characteristics of the porphyrin itself was not explored, but has been studied previously.¹ Axial ligand substitution of Mn^{III} porphyrins has been shown to vary reactivity immensely in oxygen atom transfer catalysis, and will be the focus of this report.⁶⁻¹²

Due to the electrophilic nature the epoxidation of alkenes, it would be expected that cationic catalysts might exhibit increased reactivity compared to neutral analogs. This realization lead to the development of the four-coordinate [MnTPP][SbF₆] complexes,¹ which not only increased the electrophilicity of the metal center but also offer two open coordination sites. Neutral “L” type ligands can now be introduced to one of the open coordination sites, which is *trans* to the active site that binds the molecular oxidant used in catalysis. Prior to our work on these 5-coordinate Mn^{III} porphyrins, there have been few

published examples of such compounds, with little known of their utility in oxygen atom transfer chemistry.^{13, 14} Varying the ligand *trans* to the active site changes the observed molecular geometry in the complex and the redox potential of the Mn^{III} center, causing a direct effect on observed reactivity. We hypothesize that electrochemistry, more specifically cyclic voltammetry, can be utilized as a tool to investigate reactivity trends and help target desired ligand environment. Epoxidation reactivity in these complexes involves accessing a transient Mn^V reactive species, which is not observable within our experimental conditions. However, the ability to measure the M^{III/IV} couple provides useful insight of the relative electrophilicity of the catalytically active metal.^{6, 15-17}

In addition to the axial ligand's effects on the metal's electrophilicity, we also propose that the donor number (DN) of the ligand provides an additional variable to explore in these complexes. The concept of a molecule's donor number was introduced by Gutman,¹⁸ and is representative of a molecule's combined σ and π donating ability. Based on results obtained thus far, it is proposed that axial ligands with a stronger π donating ability relative to σ strength, offer optimized epoxidation reactivity.¹ With this hypothesis in hand, we targeted MnTPP(DMF) as the ideal candidate to add to the library of MnTPP-based molecules already reported by Huang et al.¹

5.2 Synthesis and Ground State Characterization of MnTPP(DMF)

Complete synthetic details for the preparation of the cationic, four coordinate MnTPP[SbF₆] complex and corresponding DMF analogue can be found in **Appendix A**. A modified synthesis for the TPP ligand was implemented as reported previously.¹ Following salt exchange with NaSbF₆, the four coordinate MnTPP was isolated in high yield (87.9%) with minimal purification necessary. Introduction of neutral axial ligands can be performed with relative ease, with the only design parameter necessary being a non-coordinating solvent to avoid formation of the six-coordinate complex. The reaction scheme for the formation of MnTPP(DMF) is depicted in **Figure 5.1**, with these reaction conditions applicable for any neutral donor ligand which is soluble in dichloromethane.

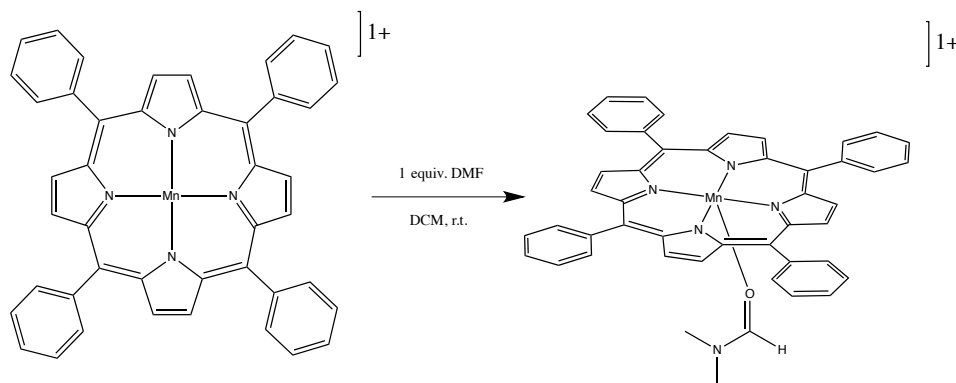


Figure 5.1 Synthesis of the 5-coordinate MnTPP(DMF) catalyst is obtained after the addition of 1 equivalent of DMF in a non-coordinating solvent such as dichloromethane

Introducing one equivalent of coordinating ligand results in the desired pentacoordinate MnTPP(DMF) catalyst, whereas the hexacoordinate metalloporphyrin can be obtained with the addition of excess ligand. Due to the need of an open coordination site for catalysis, the six coordinate complexes lack further interest despite their unique molecular geometry. FTIR measurements of the MnTPP(DMF) complex shows a slight decrease in the $\nu_{C=O}$ stretching frequency (1641 cm^{-1}) compared to free DMF (1661 cm^{-1}).¹⁹ This decrease in the $\nu_{C=O}$ stretching frequency is indicative of measurable π -backbonding between the Mn^{III} center and DMF ligand. A previous example of backbonding between datively bonded DMF ligands and Mn center has been reported, and indicates a similar degree of backbonding (1649 cm^{-1}).²⁰ Although a crystal structure has not been obtained, the molecular geometry of these types of MnTPP cationic complexes have been studied at length.¹ The presence of the pentacoordinate species has been confirmed through HR-ESIMS in addition to reactivity comparisons to previously reported MnTPP(L) complexes.¹

As stated earlier in this chapter, cyclic voltammetry can be utilized to measure the M^{III/IV} couple in these Mn^{III} complexes, and is directly related to the electrophilicity of the metal center for catalysis. The CV of MnTPP(DMF) was measured in dry DCM in a 0.1 M solution of tetrabutylammonium hexafluorophosphate at a scan rate of 100 mV/s (**Appendix D**). There were three reversible one electron redox processes within the experimental limits of DCM, characteristic of Mn^{III} metalloporphyrins. The TPP/TPP⁺ $E_{1/2}$ was found to be 0.89 V (vs. Fc/Fc⁺), consistent with previous measurements of this type of coordination

environment.¹ The Mn^{III/II} reversible reduction was experimentally determined to be -0.80 V (vs. Fc/Fc⁺), also within the range of analogous complexes. The more catalytically important redox process, measuring the oxidative potential of the Mn^{III/IV} E_{1/2}, was found to be 0.67 V. This is consistent with other measured oxygen donor ligands, and is indicative of increased electron density on the metal center compared to the four-coordinate MnTPP complex lacking an axial donor ligand.¹

5.3 Epoxidation Trials of *cis*- β -Methyl Styrene with MnTPP(DMF)

As it has been demonstrated from our group prior to this work, cationic MnTPP-based complexes exhibit faster kinetics and a higher percent conversion of alkene-substrates compared to the neutral MnTPP(Cl) complex.¹ This increased reactivity can be attributed to the increased electrophilicity of the charged complex, in addition to the presence of cooperative axial donor ligands *trans* to the active coordination site. The aim of studying this MnTPP(DMF) complex was to see if an increased *cis:trans* ratio could be achieved through this ligand modification.

The epoxidation of *cis*- β -Methyl styrene results in the formation of many products, with the corresponding *cis* and *trans* epoxides being the major products. Formation of carbonyl-containing molecules are observed, and included in the overall percent conversion of substrate total. Although the amount of carbonyl-isomerization related products is quantifiable, their presence is minimal compared to that of the desired epoxides. Huang et al. discovered that the amount of carbonyl-containing products could be increased through the use of triphenylphosphine oxide as the axial donor ligand.¹ **Table 5.1** displays the obtained data from the average of three epoxidation trials using MnTPP(DMF) as the catalyst, and *cis*- β -methyl styrene as the substrate.

Table 5.1 The molar ratio of Catalyst:Substrate:Oxidant is 5:100:200 with a substrate concentration of .10 M in CDCl₃. All reagents are added to a sealed NMR tube and sonicated for 30 seconds prior to the first measurement. The reaction mixture was vortexed for 30s every 30 minutes between ¹H NMR measurements.

Time (h)	Cis:Trans Ratio	Conversion (%)
0.25	5.19:1	71.9
2	5.26:1	90.1
8	5.38:1	94.5

Iodosobenzene has been identified as the optimum stoichiometric oxidant for the epoxidation of *cis*- β -methyl styrene, however does have some experimental limitations. Due to the insolubility of the reagent, sonication of the reaction mixture is necessary to obtain acceptable conversion of substrate. It was determined that a sonication period of 30 seconds was sufficient to decrease the particle size for optimized reaction conditions. We substituted an ultravortex mixing step of the sealed NMR tube for manual agitation of the reaction mixture. This resulted in a slight increase in overall percent conversion of substrate and a visibly more homogeneous reaction mixture than what has been previously observed.¹

Compared to other oxygen-donor neutral ligands investigated by Huang et al., the MnTPP(DMF) analogue offers a much higher *cis:trans* ratio and a percent conversion similar to what has been seen previously.¹ While a higher *cis:trans* ratio has been observed in the MnTPP(OPPh₃) analogue, it also results in the increased generation of the isomerized carbonyl products. Due to these observations, this catalyst containing the DMF axial ligand warrants increased investigation due to its increased diastereoselectivity and efficient substrate turnover.

5.4 NIR Measurements of d-d Bands in Select MnTPP(Porphyrin)(L) Catalysts

Our initial hypothesis was that epoxidation reactivity in these Mn^{III}TPP complexes could be modified with neutral donor ligands with varying degrees of σ and π basicity. However, a method of directly measuring the σ and π basicity of these ligands proved to be elusive. Following our analysis of observed catalysis, we propose that π basicity has a larger effect on reactivity than σ basicity does. This π basicity has a direct effect on the molecular orbital energetics of the d_{xz} and d_{yz} orbitals, which have the ability to π bond with the axial

ligand. Recent work published by Leto et al. aimed to investigate reactivity trends in molecular Mn^{IV} -oxo complexes using various spectroscopic techniques.²¹ Their approach utilized both ground state electronic absorption in addition to magnetic circular dichroism (MCD) spectroscopies to explore their proposed excited state reactivity model.

As described in **Chapter 2**, metal complexes containing pseudo C_{4v} symmetry contain a degenerate “e” molecular orbital set of the d_{xz} and d_{yz} orbitals of which can undergo axial π -bonding. **Figure 5.2** depicts the electronic configuration of the d-orbital manifold in these $\text{Mn}^{\text{III}}\text{TPP}(\text{L})$ complexes. The relative energies of the d orbitals in this figure are not drawn to scale. Pentacoordinate Mn^{III} complexes are known to have a high-spin electronic configuration, which results in the singly occupied d_{z^2} orbital as the HOMO.^{1, 22-24}

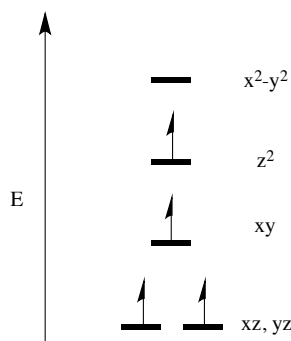


Figure 5.2 Orbital occupancy in pentacoordinate Mn^{III} complexes results in a $S = 2$ configuration and the lowest-lying orbitals being the degenerate d_{xz}/d_{yz} set.

Due to experimental limitations, we are unable to implement MCD spectroscopy to investigate the nature of orbitally forbidden d-d transitions in these complexes. However, if d-d bands in these $\text{Mn}^{\text{III}}\text{TPP}(\text{L})$ complexes have measureable intensity, they would be observable in the NIR region and could be measured using standard ground state EAS. Due to the lowest lying d-orbitals in these complexes being $d\pi^*$ in character, any effects of the π -basicity of the axial donor ligand can be seen in the energetics of spectroscopically observable d-d transitions. Table 5.2 displays the measured d-d bands in select $\text{MnTPP}(\text{L})$ complexes and their characteristics. Ongoing efforts in collaboration with the Dr. Jennifer Roizen Group at Duke University aim to characterize analogous Fe^{III} -based porphyrins in a similar way in order to identify reactivity trends in other atom transfer catalysts.

Table 5.2 Lowest energy d-d band and their approximate extinction coefficients of select Mn^{III}(L) complexes. The lowest energy occurs in the square planar MnTPP and the highest in complexes with TiOTMTAA as the donor ligand.

Complex	d-d Band Location (nm)	ϵ (M ⁻¹ cm ⁻¹)
[Mn(TPP)][SbF ₆]	789	1840
[Mn(TPP)(DMF)][SbF ₆]	766	950
[Mn(TPP)(OPPh ₃) ₂][SbF ₆]	770	975
[Mn(TFP)(Im)][SbF ₆]	779	1006
[Mn(TPP)(VOL ₃)][SbF ₆]	785	992
[Mn(TPP)(TiOTMTAA)][SbF ₆]	755	423
[Mn(TMP)(TiOTMTAA)][SbF ₆]	755	819
[Mn(TPP)(TEA)][SbF ₆]	765	1434

In addition to the energies of these transitions, the small extinction coefficients ($< 10^3$) suggest these absorption bands are in fact d-d bands. Due to previous work in our group, TiOTMTAA is known to be a strong base, resulting molecules with interesting molecular geometries and electronic characteristics.^{1, 25, 26} Strong donor ligands such as triethylamine (TEA) and TiOTMTAA result in the highest energy d-d bands. Complexes that have stronger π -donating axial ligands (DMF, OPPh₃, etc.) have d-d bands that are at neither the upper or lower limit of the complexes measured thus far. **Table 5.3** seeks to compare the measured d-d band energies of MnTPP(L) complexes and their explored epoxidation reactivity. As predicted, changing the electronic structure of the porphyrin does not have a strong effect on the d-orbital splitting. This is evident when comparing the d-d band energies in Mn(TPP)(TiOTMTAA) and Mn(TMP)(TiOTMTAA).

Table 5.3 Measured d-d band energies and catalytic data for MnTPP(L) and MnTPP(L)₂ complexes

Complex	d-d Band Location (nm)	Conversion (%)	cis/trans Ratio
[Mn(TPP)(TiOTMTAA)][SbF ₆]	755	96	3.03
[Mn(TPP)(DMF)][SbF ₆]	766	95	5.38
[Mn(TPP)(OPPh ₃) ₂][SbF ₆]	770	94	6.72
[Mn(TFP)(Im)][SbF ₆]	779	100	7.11
[Mn(TPP)][SbF ₆]	789	93	4.64

All of the complexes presented in **Table 5.3** have similar enough percent conversions of the *cis*- β -methyl styrene substrate to develop any meaningful discussion about axial donor ligand effects. However, there does seem to be a correlation between d-d band energies and obtained *cis:trans* ratio for oxygen atom transfer reactivity. Both the imidazole and triphenylphosphine oxide complexes have the lowest d-d band energies and highest observed diastereoselectivity. Conversely, the DMF and TiOTMTAA analogues are considered to have significant π -donating character that results in the increased d-d band energies. These two complexes also exhibit decreased diastereoselectivity in these epoxidation reactions. These findings suggest that NIR measurements of MnTPP(L) complexes and their d-d band energies is a useful spectroscopic handle in the investigation of these complexes and aid in the target of new ligand modifications.

5.5 Cited References

- 1) Huang, T., *Synthesis, Structure, Magnetic and Electronic Properties of Heterometallic Complexes Containing First-Row Transition Metals*. PhD Dissertation, NC State University, Raleigh, NC, **2016**
- 2) Zhang, W.; Loebach, J. L.; Wilson, S. R.; Jacobsen, E. N., *J. Am. Chem. Soc.*, **1990**, *112*, 2801-2803
- 3) Palucki, M.; Finney, N. S.; Pospisil, P. J.; Güler, M. L.; Ishida, T.; Jacobsen, E. N., *J. Am. Chem. Soc.*, **1998**, *120*, 948-954
- 4) Pospisil, P. J.; Carsten, D. H.; Jacobsen, E. N., *J. Eur. Chem.*, **1996**, *8*, 974-980
- 5) Traylor, T. G.; Miksztal, A. R., *J. Am. Chem. Soc.*, **1989**, *111*, 7443-7448
- 6) Groves, J. T.; Lee, J.; Marla, S. S., *J. Am. Chem. Soc.*, **1997**, *119*, 6929
- 7) Mohajer, D.; Karimipour, G.; Bagherzadeh, M., *New. J. Chem.*, **2004**, *28*, 740
- 8) Song, W. J.; Seo, M. S.; George, S. D.; Ohta, T.; Song, R.; Kang, M. J.; Tosha, T.; Kitagawa, T.; Solomon, E. I.; Nam, W., *J. Am. Chem. Soc.*, **2007**, *129*, 1268
- 9) Banfi, S.; Montanari, F.; Quici, S., *J. Org. Chem.*, **1989**, *54*, 1850
- 10) Takahashi, A.; Kurahashi, T.; Jufi, H., *Inorg. Chem.*, **2009**, *48*, 2614
- 11) Lai, T. S.; Lee, S. K. S.; Yeung, L. L.; Liu, H. Y.; Williams, I. D.; Chang, C. K., *Chem. Commun.*, **2003**, 620
- 12) Collman, J. P.; Zeng, L.; Brauman, J., *Inorg. Chem.*, **2004**, *43*, 2672
- 13) Williamson, M. N.; Hill, C. L., *Inorg. Chem.*, **1987**, *26*, 1602
- 14) Munro, O. Q.; Camp, G. L., *Acta Crystallogr. Sect. C: Cryst. Struct. Commun.*, **2003**, *59*, m132
- 15) Neu, H. M.; Yang, T.; Baglia, R. A.; Yosca, T. H.; Green, M. T.; Quesne, M. G.; de Visser, S. P.; Goldberg, D. P., *J. Am. Chem. Soc.*, **2014**, *136*, 13845
- 16) Mesbahi, E.; Safari, N.; Gheidi, M., *J. Porphyrins Phthalocyanines*, **2014**, *18*, 354
- 17) Arasasingham, R. D.; He, G. X.; Bruice, T. C., *J. Am. Chem. Soc.*, **1993**, *115*, 7985
- 18) Gutmann, V., *Coord. Chem. Rev.*, **1976**, *18*, 225-255

- 19) Coblenz Society, Infrared Spectrum, *In NIST Chemistry WebBook*; Dow Chemical Company, NIST Standard Reference Database 69: *NIST Chemistry WebBook*, (December) **1966**, N,N-Dimethylformamide (<http://webbook.nist.gov>)
- 20) Neofotistou, E.; Malliakas, C. D.; Trikalitis, P. N., *Inorg. Chem.*, **2007**, *46*, 8487 - 8489
- 21) Leto, D. F.; Massie, A. A.; Rice, D. B.; Jackson, T. A., *J. Am. Chem. Soc.*, **2016**, *138*, 15413-15424
- 22) Lieb, D.; Zahl, A.; Shubina, T. E.; Ivanovic-Burmazovic, I., *J. Am. Chem. Soc.*, **2010**, *132*, 7282
- 23) Krzystek, J.; Yeagle, G. J.; Park, J. H.; Britt, R. D.; Meisel, M. W.; Brunel, L. C.; Tesler, J., *Inorg. Chem.*, **2003**, *42*, 4610
- 24) Burdett, J. K., *Inorg. Chem.*, **1975**, *14*, 931
- 25) Goggins, E. M., *Lengthening Charge Transfer Excited States in First Row Transition Metals*. Ph.D. Dissertation, NC State University, Raleigh, NC, **2016**
- 26) Wu, X.; Huang, T.; Lekich, T. T.; Sommer, R. D.; Weare, W. W. *Inorg. Chem.* **2015**, *54*, 5322-5328

Appendix A Supporting Information for Reported Molecules

All reactions were carried out under a nitrogen atmosphere using standard Schlenk and drybox techniques. Chemicals were purchased from Sigma-Aldrich, Strem Chemicals Inc., Oakwood Products, or Alfa-Aesar. They were used as received unless otherwise noted. Dry acetonitrile (ACN) was obtained via distillation over CaH₂. Dichloromethane, pentane, toluene and tetrahydrofuran were dried and purified in a nitrogen atmosphere while using a Grubbs-type, two-column purification system (Innovative Technologies) and stored over activated 3 Å molecular sieves.⁵⁵ Deuterated NMR solvents (CDCl₃, C₆D₆, and CD₂Cl₂) were purchased from Cambridge Isotope Laboratories and used as internal standards for all measurements [(CDCl₃, ¹H at 7.26 and ¹³C at 77.16) (C₆D₆, ¹H at 7.16) and (CD₂Cl₂, ¹H at 5.32 and ¹³C at 53.84)].⁵⁶ The Fe^{II}(ACN)₂(OTf)₂ and Co^{II}(ACN)₂(OTf)₂ were obtained through collaboration with former group members Dr. Eric Goggins and Travis Lekich.

¹H, ¹³C NMR, and magnetic susceptibility measurements were taken at ambient temperatures on a 400 MHz Varian Unity Inova spectrometer. ATR/FT-IR measurements were obtained on a Bruker Vertex 80v FT-IR spectrometer using a Platinum ATR accessory or a Bruker Alpha ATR. Electronic absorbance spectra were recorded on a Shimadzu UV-3600 UV-Visible spectrophotometer.

[(Py₅Me₂)CrOH][BAr₄']₂ (CrOH)

Py₅Me₂ (0.499 g, 1.12 mmol) was dissolved in 40.0 mL of dry acetonitrile, which further degassed by three freeze-pump-thaw cycles. CrCl₂ (0.138 g, 1.12 mmol) was then added to the flask. The solution turned dark green immediately and was stirred at room temperature for 72 hours. The solvent was removed under reduced pressure to yield a dark green solid, which yields 0.486 g of crude [CrCl(Py₅Me₂)]Cl (76.3%). Excess deionized water was then added to this solid (20.0 mL) and allowed to stir for 48 hours. This yielded a dark pink solution before the water was removed *in vacuo*. Crude yield of [CrOH(Py₅Me₂)]Cl₂ is 0.578 g (90.1% based on [CrCl(Py₅Me₂)]Cl), overall yield of 68.7% for two steps). This was used without further purification for the synthesis of **3**. To perform the counter ion exchange, BAr₄' (0.743 g) was dissolved in 20.0 mL of diethyl ether. Crude Cr^{II}Cl (0.254 g) was separately dissolved in 15.0 mL of deionized water. These two

solutions were then combined in a round bottom flask and stirred rigorously for 30 seconds, then slowly stirred for an additional hour. The purple organic product was extracted (3x30 mL) with diethyl ether and removed through rotary evaporation. The obtained purple powder was concentrated in diethyl ether and layered with pentane to yield 0.341 g (44.5%) of dark purple crystals. Absorption spectrum: (DCM): λ_{max} (nm), ϵ ($\text{M}^{-1}\text{cm}^{-1}$); 549, 698; 394, 624. ATR/FTIR: $\tilde{\nu}_{\text{OH}}$: 3647 cm^{-1} , $\tilde{\nu}_{\text{OD}}$: 2690 cm^{-1} . Anal. Calc'd for $\text{C}_{93}\text{H}_{50}\text{B}_2\text{CrF}_{48}\text{N}_5\text{O}$: C, 49.89; H, 2.25; N, 3.13. Found: C, 49.53; H, 2.57; N, 2.96. HR ESIMS (M^+) m/z calc'd for $\text{C}_{29}\text{H}_{26}\text{CrN}_5\text{O}$ 256.075, found 256.0766. Magnetic susceptibility (CD_2Cl_2): $\mu_{\text{eff}} = 3.42\ \mu_{\text{BM}}$ via Evan's method.

$[(\text{Py}_5\text{Me}_2)\text{CrCl}][\text{BAr}_4']_2(\text{CrCl})$

CrOH (0.400g, 0.180 mmol) was quantitatively dissolved in 15.0 mL of dry THF. To this mixture, excess chlorotrimethylsilane (TMS-Cl) (24.0 μL , 0.180 mmol) was added dropwise. This was kept stirring for 24 hours which yielded a fine, pink powder after repeated washing with hexanes. Yield 0.299 g (73.2%). Absorption spectrum: (DCM): λ_{max} (nm), ϵ ($\text{M}^{-1}\text{cm}^{-1}$); 517, 101; 327, 832. Anal. Calc'd for $\text{C}_{93}\text{H}_{49}\text{B}_2\text{ClCrF}_{48}\text{N}_5$: C, 49.48; H, 2.19; N, 3.10. Found: C, 47.73; H, 1.10; N, 2.89. HR-ESIMS (M^+) m/z calc'd for $\text{C}_{29}\text{H}_{25}\text{ClCrN}_5$ 265.060, found 265.0600. Magnetic susceptibility (CD_2Cl_2): $\mu_{\text{eff}} = 3.44\ \mu_{\text{BM}}$ via Evan's method.

$[(\text{Py}_5\text{Me}_2)\text{FeOH}][\text{OTf}]_2(\text{FeOH})$

$\text{Fe}(\text{ACN})_2(\text{OTf})_2$ (0.500 g, 1.20 mmol) was dissolved in 100 mL of dry acetonitrile. This was placed in a 250 mL round bottom flask and let dissolve at room temperature. To this, the Py_5Me_2 ligand (0.559 g, 1.26 mmol) was added in small increments, which resulted in the formation of a dark, burnt orange solution. This was let stir for 24 hours at room temperature prior to solvent removal *in vacuo* which resulted in the isolation of a fine, burnt orange powder. The obtained powder was triturated three times with THF. Yield 0.764 g (75.8%). The uncharacterized orange product (0.550 g, 0.655 mmol) was then dissolved in 75 mL of dry acetonitrile, to which iodosobenzene (0.144 g, 0.655 mmol) was added in small increments. This was let stir for 2 hours, after which the solution was filtered through a fine fritted funnel to remove unreacted iodosobenzene. The obtained orange solution was then

stirred, to which diethyl ether was added to precipitate the desired product. Yield 0.411 g (77.0%). Absorption spectrum: (ACN): λ_{max} (nm), ϵ ($\text{M}^{-1}\text{cm}^{-1}$); 422, 145; 394, 3872; 350, 3834. ATR/FTIR: $\tilde{\nu}_{\text{OH}}$: 3535 cm^{-1} . HR-ESIMS (M^+) m/z calc'd for $\text{C}_{29}\text{H}_{26}\text{FeN}_5\text{O}$ 258.07379, found 258.07330.

$[(\text{Py}_5\text{Me}_2)\text{MnOH}][\text{OTf}]_2$ (MnOH)

$\text{Mn}(\text{ACN})_2(\text{OTf})_2$ (0.735 g, 1.69 mmol) was dissolved in 80 mL of dry acetonitrile. This was placed in a 150 mL round bottom flask and let dissolve at room temperature. To this, the Py_5Me_2 ligand (0.750 g, 1.69 mmol) was added in small increments, which resulted in the formation of a light yellow solution. This was let stir for 24 hours at room temperature prior to solvent removal *in vacuo* which resulted in the isolation of a fine, whitish yellow powder. The obtained powder was triturated three times with THF. Yield 1.16 g (85.9%). The uncharacterized orange product (0.250 g, 0.298 mmol) was then dissolved in 15 mL of dry acetonitrile and .50 mL of deionized water, to which iodosobenzene (0.066 g, 0.298 mmol) was added in small increments. This was let stir for 2 hours, after which the solution was filtered through a (F) fritted funnel to remove unreacted iodosobenzene. The obtained light brown solution was then stirred, to which diethyl ether was added to precipitate the desired product. MnOH was isolated as a fine, tan powder after placed under vacuum to dryness. Yield .221 g (91.3%). ATR/FTIR: $\tilde{\nu}_{\text{OH}}$: 3599 cm^{-1} . HR-ESIMS (M^+) m/z calc'd for $\text{C}_{29}\text{H}_{26}\text{MnN}_5\text{O}$ 257.57534, found 257.57447.

$[(\text{Py}_5\text{Me}_2)\text{CoOH}][\text{OTf}]_2$ (CoOH)

Py_5Me_2 (4.092 g, 9.24 mmol) was added to a previously dried 250 mL round bottom flask and dissolved in 100 mL 10:1 mixture of acetone and water. This was then sparged with $\text{N}_{2(\text{g})}$ for 30 minutes. Solid $\text{Co}(\text{ACN})_2(\text{OTf})_2$ (3.78 g, 9.24 mmol) was then added quickly to this solution, and kept stirring for 24 hours. The water and acetone were removed under reduced pressure resulting in an orange solid. This was then dissolved in a minimum amount of acetonitrile, and precipitated with the addition of diethyl ether. The product was then filtered through a fine fritted funnel and washed with diethyl ether. Residual solvent was removed *in vacuo*. Yield 5.97 g (79.0%). Following this, the obtained $[(\text{Py}_5\text{Me}_2)\text{CoOH}_2][\text{OTf}]_2$ (0.300 g, 0.366 mmol) was dissolved in 25 mL of dry acetonitrile in

a previously dried 100 mL round bottom flask. This was then kept open to atmospheric conditions at a stir rate of 1200 rpm for 48 hours. After which the reaction resulted in the formation of a heterogeneous red solution. The product was precipitated out of solution with the addition of diethyl ether. The mixture was then filtered through a fine fritted funnel to yield a fine, dark red powder. Residual solvent was removed under reduced pressure. Yield 0.218g (73.0%). ^1H NMR (400 MHz, CD_3CN): δ 9.65 (d, $J = 5.6$ Hz, 4H), 8.27 (m, 3H), 8.04 (m, 4H), 7.97 (m, 4H), 7.70 (m, 4H), 2.80 (s, 6H, CCH_3). ^{13}C NMR (400 MHz, CD_3CN): δ 158.62, 157.97, 153.45, 143.49, 141.99, 125.69, 124.55, 123.61, 118.26 (aryl), 56.68 (CF_3), 30.82 (C-CH_3), 22.55 (C-CH_3). Absorption spectrum: (ACN): λ_{max} (nm), ϵ ($\text{M}^{-1}\text{cm}^{-1}$); 519, 189; 413, 270. ATR/FTIR: $\tilde{\nu}_{\text{OH}}$: 3521 cm^{-1} . HR-ESIMS (M^+) m/z calc'd for $\text{C}_{29}\text{H}_{26}\text{CoN}_5\text{O}$ 259.5729, found 259.5735

Asymmetric Methyl [O_3N]Ti(O^iPr) (TiO^iPr)

N,N-bis(2-hydroxy-3,5-dimethylbenzyl)-2-aminoethanol (1.45 g, 4.39 mmol) was dissolved in dry toluene (15.0 mL) in a drybox. To this solution, titanium isopropoxide (1.25 g, 4.39 mmol) was added dropwise at room temperature to yield an orange/yellow solution, which was stirred for an additional 48 hrs. Solvent was removed under reduced pressure and washed with petroleum ether, yielding 0.962 g (54.1%) of a fine, yellow powder. ^1H NMR (400 MHz, CD_2Cl_2): δ 6.90 (s, 2H, arom), 6.74 (s, 2H, arom), 4.86 (bs, 1H, $\text{CH}(\text{CH}_3)_2$), 4.30 (bs, 2H, $\text{OCH}_2\text{CH}_2\text{N}$), 3.90 (bs, 2H, NCH_2Ar), 3.61 (bs, 2H, $\text{OCH}_2\text{CH}_2\text{N}$), 3.06 (bs, 2H, NCH_2Ar), 2.23 (s, 12H, CH_3Ar), 1.17 (m, 6H, $\text{CH}(\text{CH}_3)_2$). ^{13}C NMR (400 MHz, CD_2Cl_2): δ 159.13, 131.21, 128.65, 127.90, 125.02, 123.84 (aryl), 78.96 (CHO), 70.91 (CH_2O), 59.92 (OCH_2N), 57.50 (CH_2N), 25.77 ($(\text{CH}_3)_2\text{CHO}$), 20.70 (aryl- CH_3), 16.70 (aryl- CH_3). Absorption spectrum: (DCM): λ_{max} (nm), ϵ ($\text{M}^{-1}\text{cm}^{-1}$); 332, 2810; 261, 15121. Anal. Calc'd for $\text{C}_{23}\text{H}_{31}\text{NO}_4\text{Ti}$: C, 63.74; H, 7.21; N, 3.23. Found: C, 64.10; H, 7.97; N, 2.95.

Asymmetric *t*-Butyl [O_3N]Ti(O^iPr)

6,6'-(((2-hydroxyethyl)azanediyl) bis(methylene)) bis(2,4-di-*tert*-butylphenol) (2.65 g, 5.32 mmol) was dissolved in dry toluene (20 mL) in a drybox. To this, titanium isopropoxide (1.44 g, 5.07 mmol) was added dropwise at room temperature to yield a golden yellow solution after stirring for 72 hours. The toluene was removed under reduced pressure,

and washed with petroleum ether yielding a fine, yellow powder. Yield 1.59 g (52.1%). ^1H NMR (300 MHz, C_6D_6): δ 7.56 (s, 2H), 6.89 (s, 2H), 4.10 (bs, 1H, $\text{CH}(\text{CH}_3)_2$), 2.11 (s, 2H), 1.83 (s, 6H, $\text{CH}(\text{CH}_3)_2$), 1.70 (m, 2H), 1.37 (s, 36H, aryl- $\text{C}(\text{CH}_3)_3$). Absorption spectrum: (DCM): λ_{max} (nm), ϵ ($\text{M}^{-1}\text{cm}^{-1}$); 349, 5527; 265, 30332. To be submitted for elemental analysis.

Symmetric Methyl $[\text{O}_3\text{N}]\text{Ti}(\text{O}^i\text{Pr})$

The previously synthesized 6,6',6''-(nitrilotris(methylene))tris(2,4-dimethylphenol) (3.07 g, 7.31 mmol) was dissolved in 30 mL of dry toluene in a previously dried 100 mL round bottom flask. To this solution, titanium isopropoxide was added dropwise (2.08 g, 7.32 mmol) to yield a yellow solution. This was let stir for 48 hours to yield a fine, yellow powder after toluene removal under reduced pressure. After repeated washing with petroleum ether, the yellow powder was placed under reduced pressure to remove residual solvent. Yield 3.69 g (53.3%). ^1H NMR (400 MHz, C_6D_6): δ 6.60 (s, 2H), 6.47 (s, 2H) (aryl), 4.03 (bs, 1H, $\text{OCH}(\text{CH}_3)_2$), 2.28 (s, 6H, $\text{CH}(\text{CH}_3)_2$), 2.10 (s, 12H). Absorption spectrum: (DCM): λ_{max} , ϵ ($\text{M}^{-1}\text{cm}^{-1}$); 374, 8035; 270, 51597. To be submitted for elemental analysis.

$\text{Cr}^{\text{III}}\text{OTi}^{\text{IV}}$

TiO^iPr (23.5 mg, 0.057 mmol) was dissolved in 9.00 mL of dry THF. CrOH (0.125 g, 0.057 mmol) was dissolved separately in 9.00 mL of dry THF. The solution of TiO^iPr was added dropwise to the solution of CrOH over 5 minutes at room temperature. This immediately yielded a burnt orange solution, which was kept stirring for 48 hours. The THF was removed under reduced pressure to yield a waxy, burnt orange solid. This was washed with pentane (2x15 mL) to yield a fine, burnt orange powder. Large, burnt orange crystals were obtained through vapor diffusion of pentane into a dichloromethane solution. Yield 0.110 g (74.6%). Absorption spectrum: (DCM): λ_{max} (nm), ϵ ($\text{M}^{-1}\text{cm}^{-1}$); 525, 61; 261, 54093. Anal. Calc'd for $\text{C}_{113}\text{H}_{73}\text{B}_2\text{CrF}_{48}\text{N}_6\text{O}_4\text{Ti}$: C, 51.96; H, 2.82; N, 3.22. Found: C, 52.30; H, 2.23; N, 3.14. HR-ESIMS (M^+) m/z calc'd for $\text{C}_{49}\text{H}_{49}\text{CrN}_6\text{O}_4\text{Ti}$ 442.635, found 442.6350. Magnetic susceptibility (CD_2Cl_2): $\mu_{\text{eff}} = 3.10 \mu_{\text{BM}}$.

Fe^{III}OTi^{IV}

TiOⁱPr (.100 g, 0.247 mmol) was dissolved in 12 mL of dry THF in a previously dried vial. FeOH(.553 g, 0.247 mmol) was dissolved separately in 6 mL of distilled acetonitrile. To the yellow solution of TiOⁱPr, the acetonitrile solution of FeOH was added in a single aliquot. This immediately resulted in the formation of a dark burnt orange solution, which was let stir for 48 hours. The solvent was removed under reduced pressure to yield a dark burnt orange powder. The obtained solid was washed repeatedly with dry THF (3x 15 mL) and residual solvent was removed under reduced pressure. The product was isolated as a fine, burnt orange powder. Yield 0.599g (92.7%). Absorption spectrum: (ACN): λ_{\max} , ϵ ($M^{-1}cm^{-1}$); 417, 4651; 387, 6103; 346, 7711. HR-ESIMS (M^+) m/z calc'd for C₄₉H₄₉FeN₆O₄Ti 444.6316, found 444.6305. To be submitted for elemental analysis.

Co^{III}OTi^{IV}

TiOⁱPr (66.2 mg, 0.163 mmol) was dissolved in 10 mL of dry THF in a previously dried vial. Separately, CoOH (0.134g, 0.163 mmol) was dissolved in 8 mL of distilled acetonitrile. The solution containing CoOH was then added in a single aliquot and kept stirring for 48 hours. This immediately yielded a dark, purple-red solution. The solvent was removed under reduced pressure to yield a dark, red solid. The obtained solid was washed repeatedly with THF (3x 15 mL) and residual solvent was removed under reduced pressure. The product was isolated as a fine, dark purple-red powder. Yield 0.181g (93.3%). Absorption spectrum: (ACN): λ_{\max} , ϵ ($M^{-1}cm^{-1}$); 536, 160. HR-ESIMS (M^+) m/z calc'd for C₄₉H₄₉CoN₆O₄Ti 446.1307, found 446.1315. To be submitted for elemental analysis.

1,1-bis(2-pyridyl)ethane

This polypyridyl molecule was synthesized as previously reported.⁴⁵ To a previously oven dried 1 L round bottom flask, 2-ethylpyridine (30.0 mL, 262 mmol) was dissolved in THF (250 mL) at room temperature and let stir until the solution appeared homogeneous. This solution was then cooled to -78 °C using a dry ice/acetone bath at a stir rate of 380 rpm. N-butyllithium (250 mmol, 1.6 M in hexanes) was added to a dropping funnel prior to dropwise addition. Upon dropwise addition the solution turned a bright orange color initially, and dark red after complete addition. To this, 2-fluoropyridine (10.8 mL, 125 mmol) was

added dropwise at $-78\text{ }^{\circ}\text{C}$ prior to being brought to room temperature. This was then brought to reflux for one hour prior to workup. This was poured over ice to quench any potential reactive intermediates. Organics were extracted with dichloromethane (2x 200 mL) to yield a dark yellow/orange solution. This was dried using anhydrous sodium sulfate, then filtered to yield a transparent yellow/orange solution. Solvent was removed using rotary evaporation followed by high vacuum to remove residual solvent. Vacuum distillation of the crude 1,1-bis(2-pyridyl)ethane mixture was then performed, using a collection flask cooled with dry ice to accelerate product collection and also to prevent the loss of distilled product. The collection occurred at a temperature of $92\text{ }^{\circ}\text{C}$ at 820 mTorr. Collected product was a golden oil. Yield 15.6 g (33.9%). ^1H NMR (300 MHz, CDCl_3): δ 8.51 (m, 2H), 7.57 (m, 2H), 7.24 (m, 2H), 7.07 (m, 2H) (aryl), 4.45 (q, $J = 6.9\text{ Hz}$, 1H, CHCH_3), 1.74 (d, $J = 7.2\text{ Hz}$, 3H, CHCH_3).

Py₅Me₂ Ligand

This polypyridyl molecule was synthesized as previously reported.⁴⁵ 1,1-bis(2-pyridyl)ethane (14.2 g, 76.9 mmol) was dissolved in 215 mL of dry THF in a previously oven-dried 1L round bottom flask at room temperature. This was then brought down to $-78\text{ }^{\circ}\text{C}$ using a dry ice/acetone bath. To an addition funnel, n-butyllithium was added for the subsequent dropwise addition (46.6 mL, 74.6 mmol, 1.6 M in hexanes). This was performed at a rate of 2 drops per second for the first 5 minutes, with the rest added over the course of the next 20 minutes. This was then brought up to room temperature before the next step. To this reaction mixture, 2,6-difluoropyridine was added (1.8 mL, 19.2 mmol) dropwise which yielded a dark red/orange solution. This was let stir for 30 minutes at room temperature, then brought to reflux for 48 hours. This mixture was then brought down to room temperature prior to work up. The reaction was quenched with water (350 mL) followed by removal of the THF via rotary evaporation. The organics were extracted using a 6:1 mixture of THF to hexanes (4x 120 mL) and dried using anhydrous sodium sulfate. The organics were isolated following rotary evaporation of the solvent mixture. The obtained thick, golden oil was then dissolved in the minimum amount of dichloromethane and layered with diethyl ether to induce crystallization. After 12 hours, large golden crystals were obtained as the product.

Yield 6.59g (77.4%). ^1H NMR (300 MHz, CDCl_3): δ 8.51 (m, 4H), 7.56 (m, 2H), 7.40 (m, 4H), 7.05 (m, 4H), 6.83 (m, 4H), 2.20 (s, 6H). Absorption spectrum: (DCM): λ_{max} (nm), ϵ ($\text{M}^{-1}\text{cm}^{-1}$); 269, 42262; 263, 42026; 257, 35768.

(N,N-bis(2-hydroxy-3,5-dimethylbenzyl)-2-aminoethanol)

2,4-dimethylphenol (25.3 g, 207 mmol), 37% formaldehyde solution (6.22 g, 207 mmol), ethanolamine (6.33 g, 104 mmol), and *n*-pentanol (10.0 mL) were added to a previously dried 100 mL round bottom flask. This was then set to reflux for 72 hours, which yielded a biphasic yellow oil. This was washed with a saturated solution of NaCl and extracted in toluene (2x 75 mL). The combined organic extractions were then rotary evaporated to yield a yellow oil with a white precipitant. The obtained solids were recrystallized from hot toluene to yield a white product. Yield 1.97 g (5.8%). ^1H NMR spectrum (400 MHz, CDCl_3): δ 6.86 (s, 2H, arom), 6.70 (s, 2H, arom), 3.87 (t, $J = 5.2\text{Hz}$, 2H, $\text{HOCH}_2\text{CH}_2\text{N}$), 3.75 (s, 4H, NCH_2Ar), 2.71 (t, $J = 4.8\text{Hz}$, 2H, $\text{HOCH}_2\text{CH}_2\text{N}$), 2.20 (s, 12H, ArCH_3).

6,6',6''-(nitrilotris(methylene))tris(2,4-dimethylphenol)

Hexamine (2.50 g, 17.8 mmol) and p-formaldehyde (3.21 g, 107 mmol) were added to a previously dried 100 mL round bottom flask. 2,4-dimethylphenol (25.8 mL, 214 mmol) was added to the solid mixture via syringe. Deionized water (2.50 mL) was also added to the mixture as a condensation catalyst. This was set to reflux for 72 hours. After 24 hours, the solution appeared brown with a white solid visible in the flask. After the 72 hour period, the reaction mixture is a waxy, yellow solid. Following repeated washings with hexanes to remove starting material and side-products, a white powder was obtained and placed under high vacuum to dryness. Yield 23.3 g (78.0%). ^1H NMR (300 MHz, CDCl_3): δ 6.85 (s, 3H, aryl- CH_3), 6.72 (s, 3H, aryl- CH_3), 3.62 (s, 6H, N- CH_2), 2.20 (s, 18H).

6,6'-(((2-hydroxyethyl)azanediyl)bis(methylene))bis(2,4-di-*tert*-butylphenol)

2,4-di-*tert*-butylphenol (41.3 g, 200 mmol) was first warmed with a heat gun to obtain a viscous liquid and added to a previously dried 100mL round bottom flask. To this, 37% v/v formaldehyde solution (25.0 mL, 200 mmol) and ethanolamine (6.11 g, 100 mmol) was added to the flask. This reaction apparatus was placed in an open vessel μ -wave reactor.

This was performed using a procedure developed by Aaron Francis, which is soon to be published in collaboration with Prof. Tanja Cuk of UC-Berkeley. The reaction settings were set to a reaction temperature of 110 °C for 10 hours at 200 W using a ramp-up time of 20 minutes. This reaction mixture was then dissolved in the minimum amount of toluene crystallized via slow evaporation. After 72 hours, a white solid was observed which was then washed repeatedly with petroleum ether to yield a fine, white powder after mortar and pestle grinding. Yield 10.1 g (10.1%). ¹H NMR (300 MHz, CDCl₃): δ 7.22 (s, 2H), 6.90 (s, 2H), 3.89 (t, J = 5.4 Hz, 2H, HOCH₂CH₂), 3.77 (s, 4H, NCH₂), 2.74 (t, J = 5.1 Hz, HOCH₂CH₂), 1.40 (s, 18H, aryl-C(CH₃)₃), 1.27 (s, 18H, aryl-C(CH₃)₃).

Sodium tetrakis[3,5-bis(trifluoromethyl)phenyl]borate

Sodium BA₄' was synthesized as previously reported.⁵⁷ 300 mL of dry THF was added to a previously dried 1 L 3-neck round bottom flask with magnesium turnings (7.72 g, 317 mmol). After activating the magnesium with the addition of dichloroethane (0.1 mL), 1,3-bis(trifluoromethyl)-5-bromobenzene (66.4 g, 227 mmol) was added to an addition funnel. This arene was then added dropwise to the THF/Mg mixture over 1 hour to form the Grignard reagent. This resulted in the formation of a black solution and let stir for one additional hour prior to the next reaction step. An excess of N_{2(g)} backpressure in the reaction flask was created, which allowed for the direct addition of solid sodium tetrafluoroborate (4.98 g, 45.3 mmol). This was let stir at room temperature for 48 hours, followed by refluxing for 2 hours. This was then cooled to room temperature and then neutralized with sodium carbonate (79.0 g) in a 1 L aqueous solution. This reaction mixture was then filtered using a coarse fritted funnel to remove all solids. The solution was extracted with diethyl ether (3x 200 mL) and combined organic extractions dried over anhydrous sodium sulfate overnight. This organic layer was then heated with activated charcoal for 2 hours to remove additional impurities resulting in a more transparent, tan solution. Solvent was then removed via rotary evaporation to yield a tan, oily solid. This was dissolved quantitatively in the minimum amount of dichloromethane and set to crystallize via slow evaporation, which yielded an off-white solid after 72 hours. The obtained solid was then washed repeatedly with hexanes to yield a fine, off-white powder. Yield 22.7 g (58.7%). ¹H NMR (300 MHz,

CDCl₃): δ 7.64 (s, 4H), 7.56 (s, 8H).

Tetrabutylammonium tetrakis[3,5-bis(trifluoromethyl)phenyl]borate

Sodium tetrakis[3,5-bis(trifluoromethyl)phenyl] borate (10.0 g, 113 mmol) was dissolved in 150 mL of dry THF. To this, tetrabutylammonium chloride (3.14 g, 113 mmol) was added in small increments over a 2 hour period. This solution was let stir for 48 hours, with a white precipitant observed after 10 minutes. This was recrystallized repeatedly from hot dichloromethane after the removal of the sodium chloride precipitant. The product was observed as a waxy, yellow solid. Yield 11.9 g (95.6%). ¹H NMR (300 MHz, CDCl₃): δ 7.69 (s, 4H), 7.53 (s, 8H), 3.00 (m, 8H), 1.53 (m, 8H), 1.31 (m, 8H), .93 (m, 12H).

5,10,15,20-Tetraphenylporphin (TPP)

A 500 mL 3-neck round bottom flask was charged with 90 mL of glacial acetic acid, 45 mL of propionic acid, and 60 mL of *p*-nitrotoluene. This was then affixed with two 250 mL addition funnels and a water condenser and placed under N₂(g) for 30 minutes. In one addition funnel, benzaldehyde (3.18 g, 30.0 mmol) was dissolved in 60 mL of *p*-nitrotoluene. In the other addition funnel, freshly distilled pyrrole (2.02 g, 30.0 mmol) was dissolved in 45 mL of propionic acid. The flask was then heated to 110 °C for 10 minutes, after which the contents of the two addition funnels were added at a fast dropwise pace. Complete addition was finished after 1 hour, after which the reaction mixture was set to reflux for 5 hours. This was then gradually cooled to room temperature and placed in a freezer overnight. The precipitated product was filtered through a (F) fritted funnel and washed with cold methanol until the solvent was colorless. Isolated product was a fine, purple crystalline solid and was placed under vacuum overnight to removed residual methanol. Yield 1.54 g (33.5%).

[(TPP)(Cl)(Mn)] (MnTPP(Cl))

The previously synthesized TPP ligand (.500 g, .813 mmol) was dissolved in 150 mL of anhydrous N,N-dimethylformamide (DMF) in a glovebox inside a 250 mL round bottom flask. This was the affixed with a water condenser and placed under N₂(g). To this, MnCl₂*4H₂O (.161 g, .813 mmol) was added in three equivalent aliquots in 10 minute increments. After complete addition, the reaction mixture was then set to reflux for 24 hours under aerobic conditions. The reaction mixture was then slowly cooled to room temperature,

then placed in a freezer overnight. The product precipitated from solution and was filtered through a (F) fritted funnel followed by repeated washings of cold diethyl ether until colorless. The product was isolated as a crystalline green solid without further purification. Yield .405 g (70.9%).

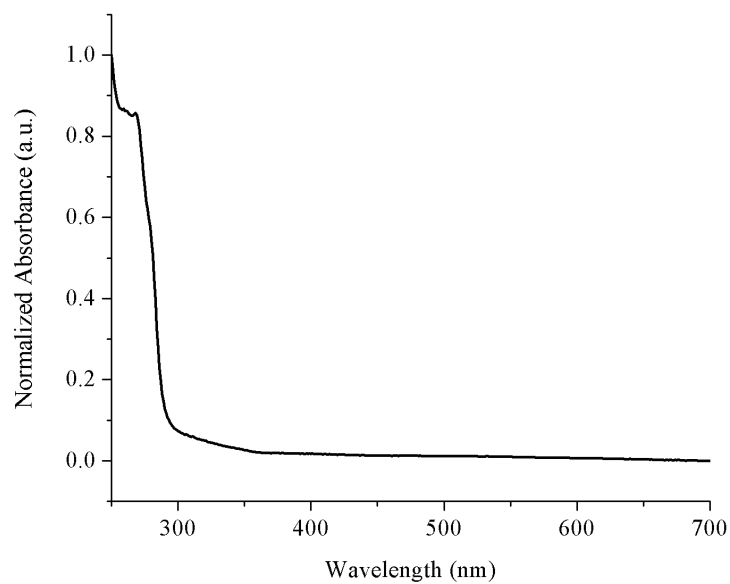
[(TPP)(Mn)][SbF₆] (MnTPP)

In a glovebox, the previously synthesized MnTPP(Cl) (.405 g, .576 mmol) was placed in a 100 mL Schlenk bomb in addition to NaSbF₆ (.149 g, .576 mmol). To these solid reagents, 15 mL of a 1:1 mixture of toluene:acetonitrile was added and the flask sealed. This was taken out of the glovebox and heated to 80 °C for 18 hours in an oil bath followed by gradual cooling to room temperature. The solution was then passed through a (F) fritted funnel to remove precipitated sodium chloride, which resulted in the isolated of a homogeneous, dark green solution. This was placed under vacuum to remove all solvent, then dissolved in a minimum amount of dichloromethane and layered with *n*-pentane. This was placed in a freezer overnight which yielded a green crystalline powder after filtration and repeated washings with cold *n*-pentane. Yield .458 g (87.9%).

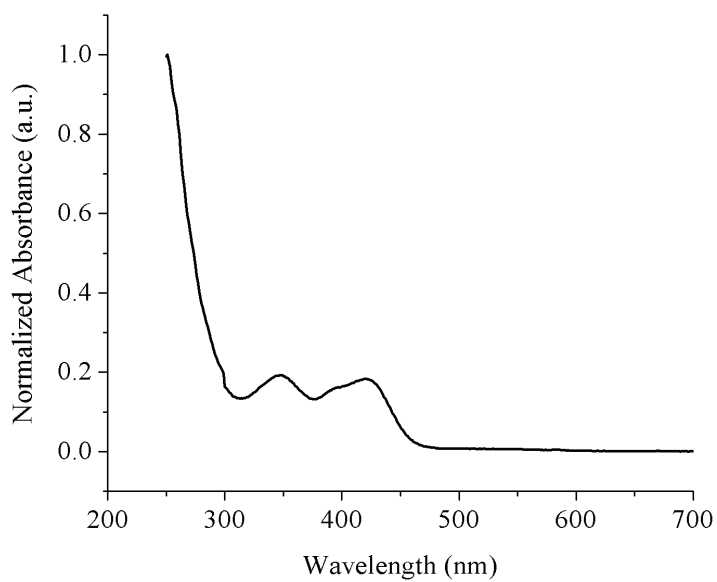
[(TPP)(DMF)(Mn)][SbF₆] (MnTPP(DMF))

A 1.0 M solution of anhydrous N,N-dimethylformamide in dry dichloromethane was prepared in a glovebox. The previously synthesized MnTPP (.100 g, .111 mmol) was dissolved in 5 mL of dry dichloromethane. To this, 1 equivalent of DMF was added and let stir under inert conditions for 15 minutes. Following the coordination, this solution was layered with *n*-pentane and placed in a freezer overnight. The product precipitated from solution and the solvent was removed *in vacuo* to dryness. Product was isolated as a crystalline green solid without additional purification. Yield .103 g (95.5%). ATR/FTIR: $\tilde{\nu}_{\text{C=O}}$: 1641 cm⁻¹. Absorption spectrum: (DCM): λ_{max} , ϵ (M⁻¹cm⁻¹); 378, 80481; 478, 133822; 580, 14550; 617, 14798. HR-ESIMS (M⁺) *m/z* calc'd for C₄₇H₃₅MnN₅O 740.22166, found 740.21940.

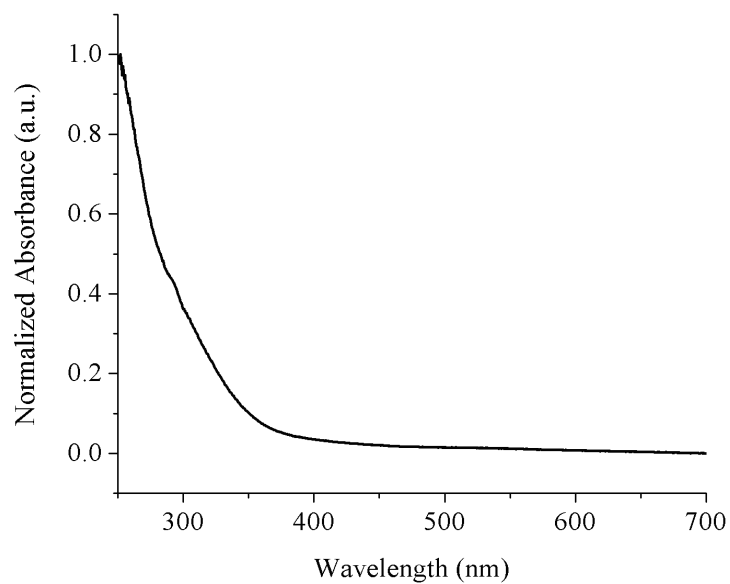
Appendix B Electronic Absorption Spectra



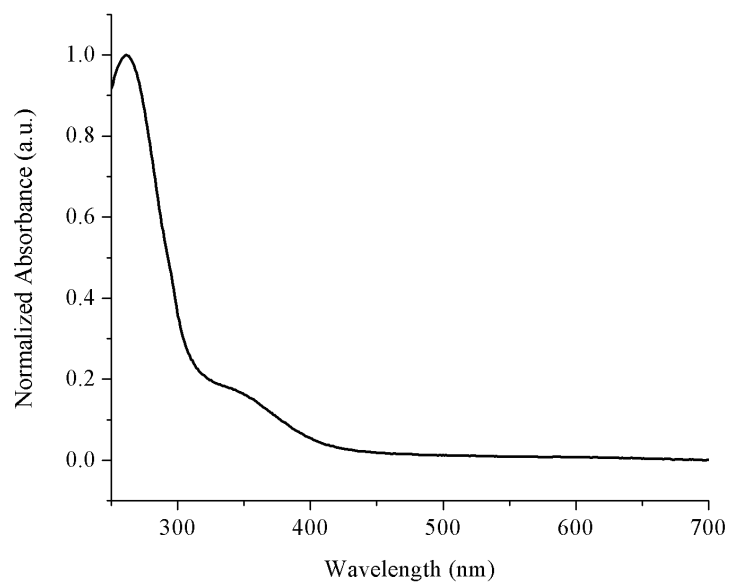
CrOH taken in dichloromethane at a concentration of $1.0\text{E-}4$ M



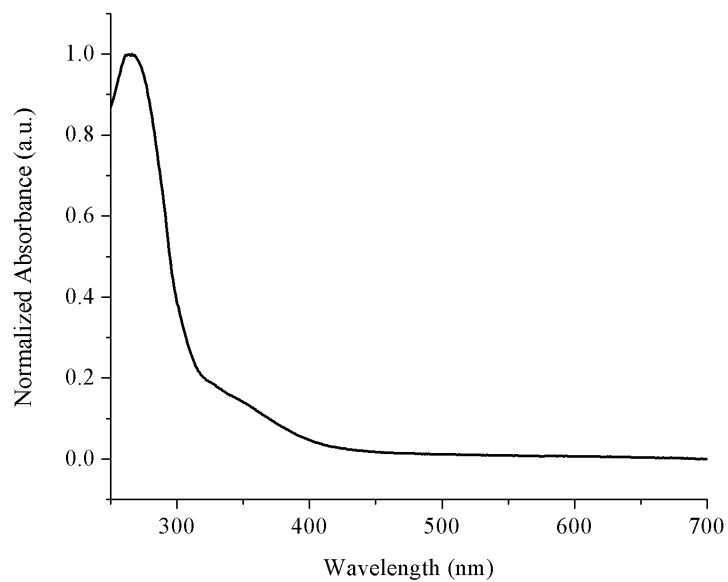
FeOH taken in acetonitrile at a concentration of $7.5\text{E-}5$ M



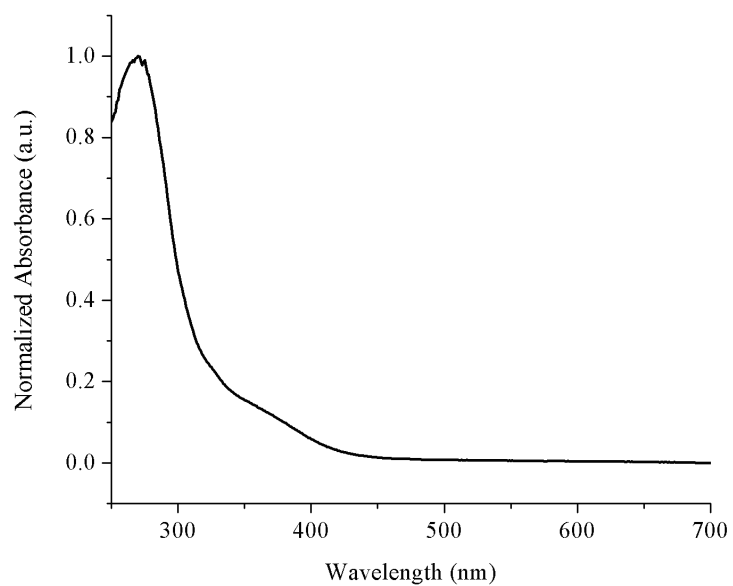
CoOH taken in acetonitrile at a concentration of $5.0E-5$ M



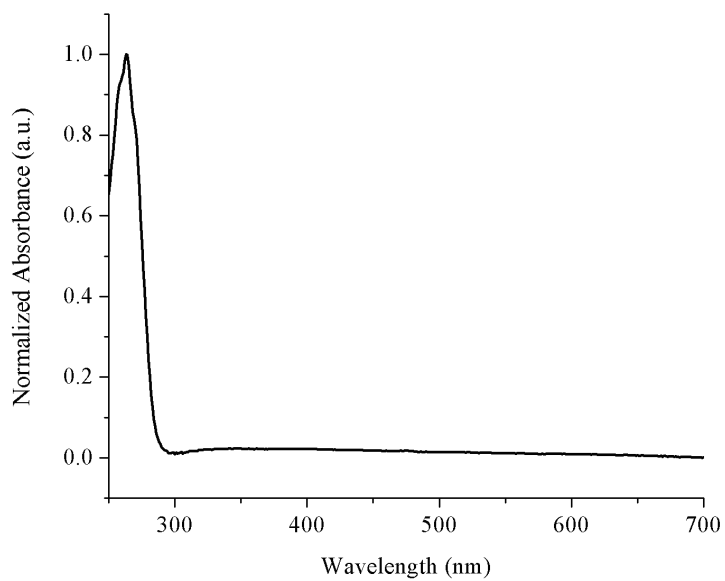
Asymmetric Methyl TiOⁱPr taken in dichloromethane at a concentration of $1.0E-4$ M



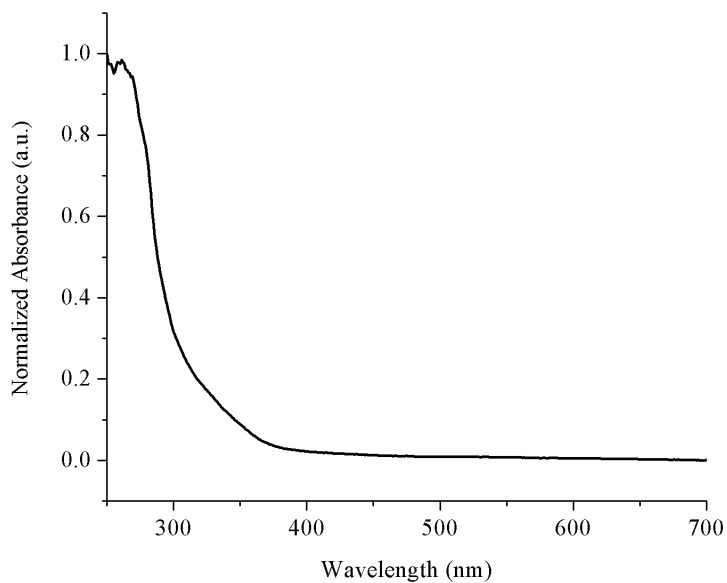
Asymmetric t-Butyl TiOⁱPr taken in dichloromethane at a concentration of 5.0E-5 M



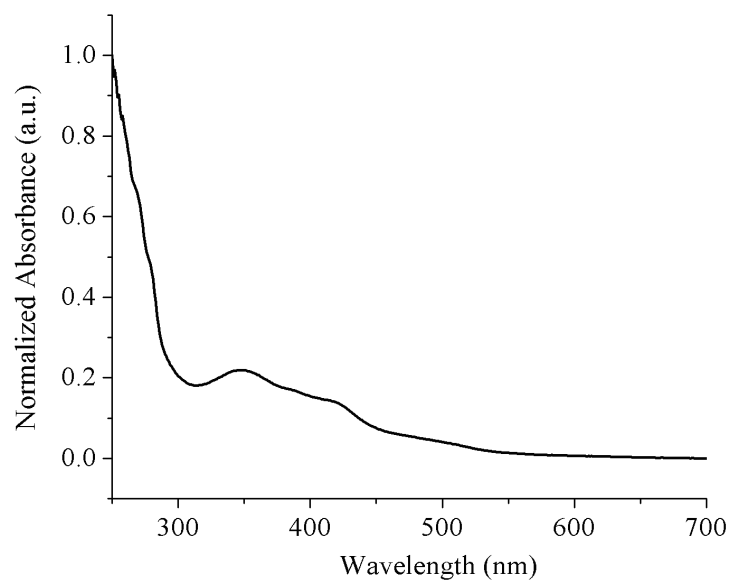
Symmetric Methyl TiOⁱPr taken in dichloromethane at a concentration of 5.0E-5 M



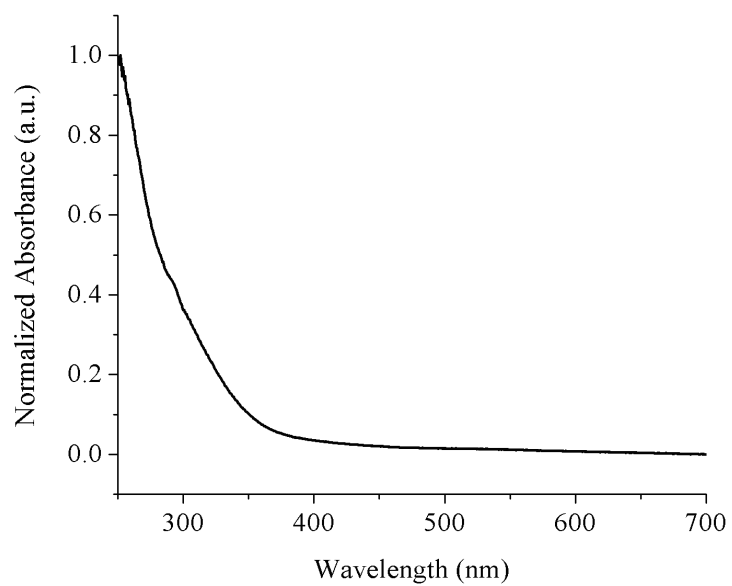
Py_5Me_2 taken in dichloromethane at a concentration of $1.0 \times 10^{-4} \text{ M}$



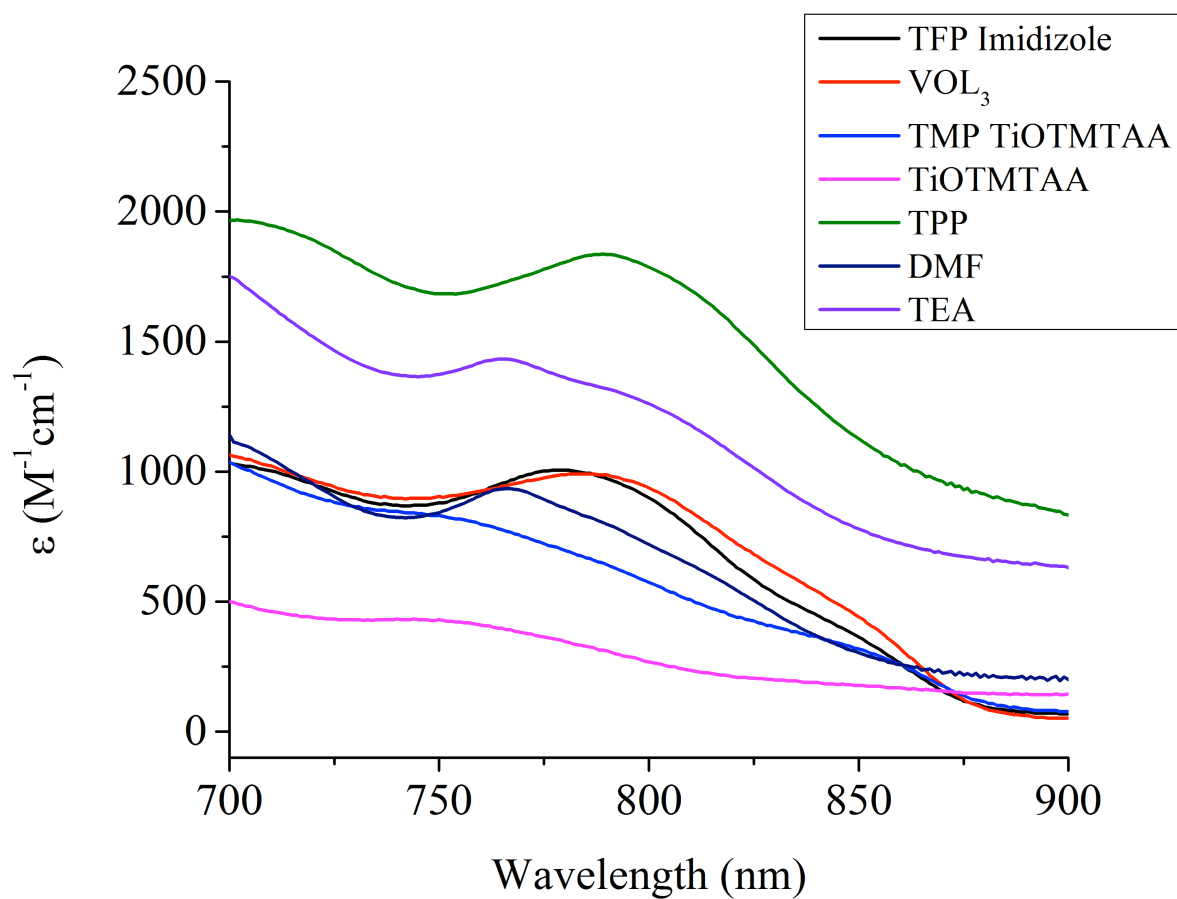
$\text{Cr}^{\text{III}}\text{OTi}^{\text{IV}}$ taken in dichloromethane at a concentration of $5.0 \times 10^{-5} \text{ M}$



$\text{Fe}^{\text{III}}\text{OTi}^{\text{IV}}$ taken in dichloromethane at a concentration of $8.0\text{E-}5$ M

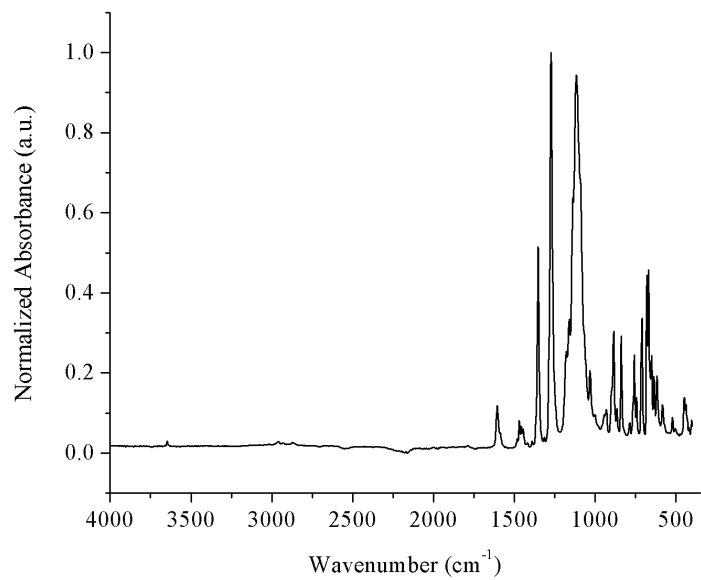


$\text{Co}^{\text{III}}\text{OTi}^{\text{IV}}$ taken in acetonitrile at a concentration of $7.0\text{E-}5$ M

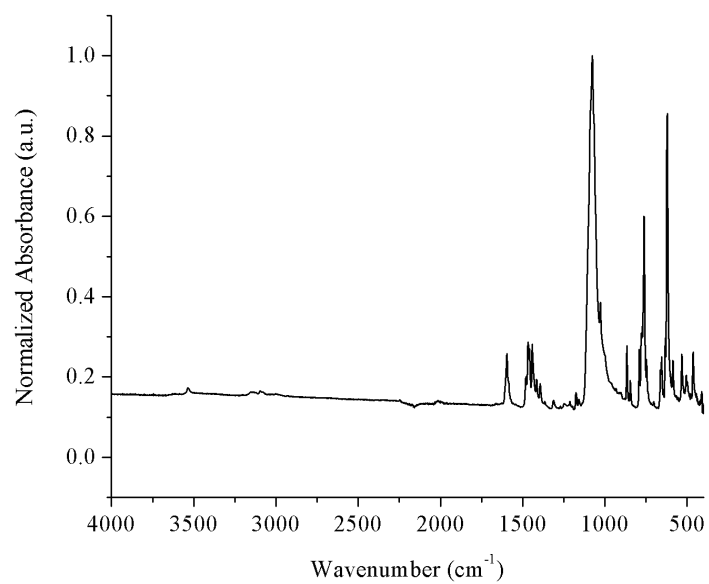


EAS of various Mn^{III}-Porphyrin(L) complexes with all spectra obtained in dichloromethane at room temperature.

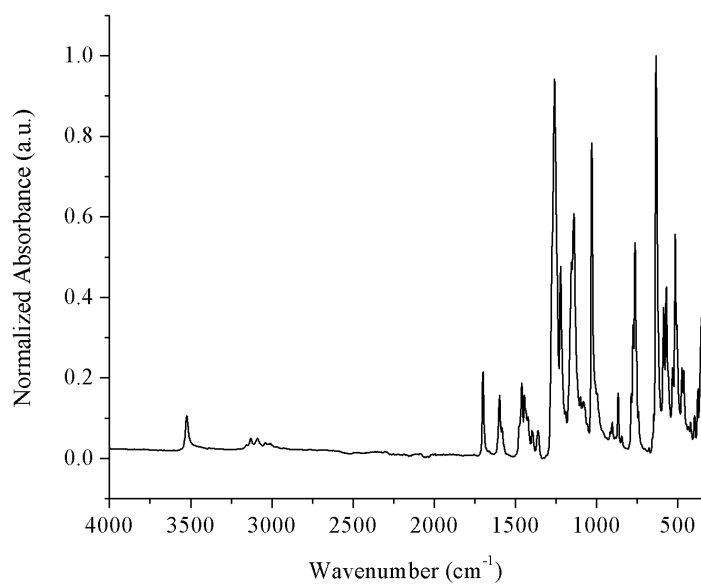
Appendix C Fourier Transform Infrared Spectra



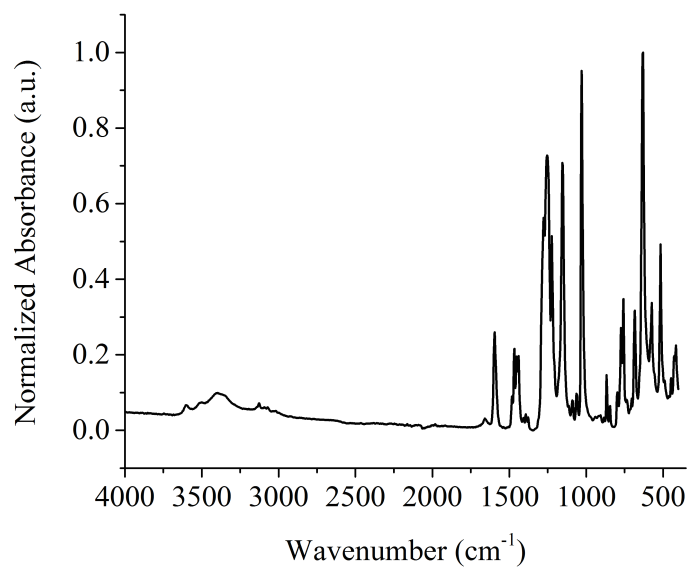
CrOH Solid state ATR spectrum



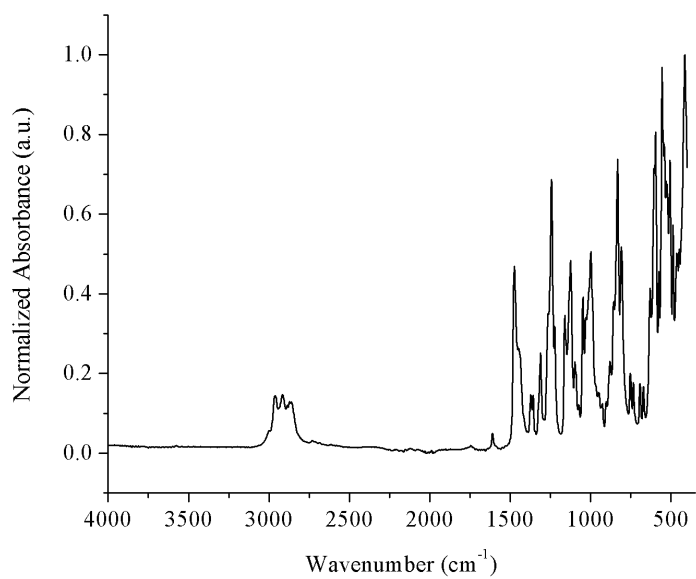
FeOH Solid state ATR spectrum



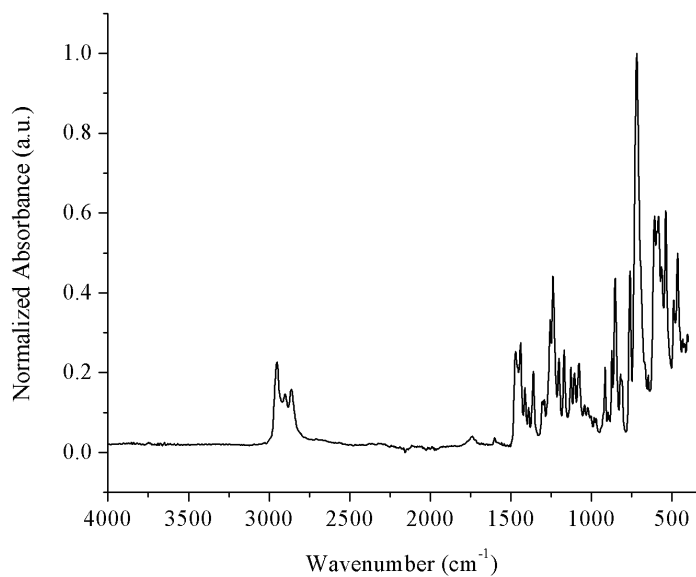
CoOH Solid state ATR spectrum



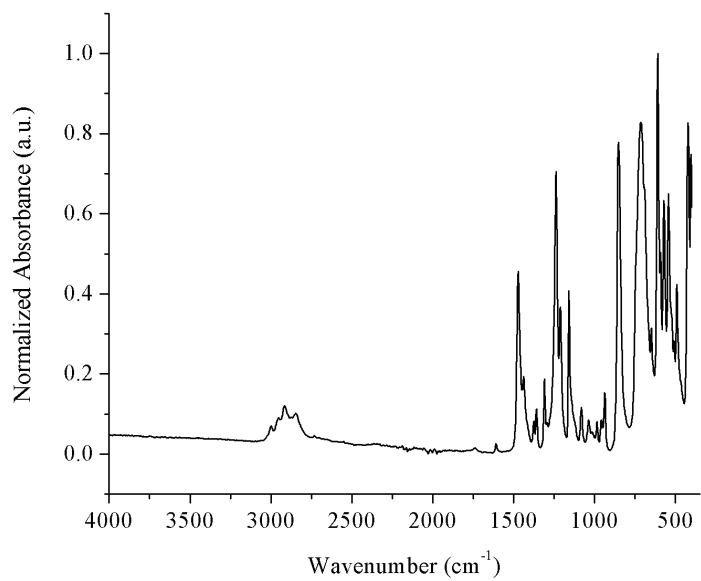
MnOH Solid state ATR spectrum



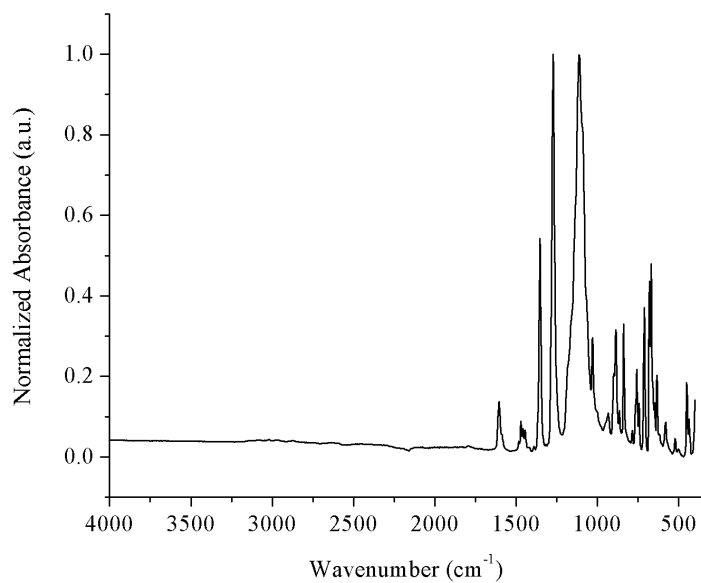
Asymmetric Methyl TiO^iPr Solid state ATR spectrum



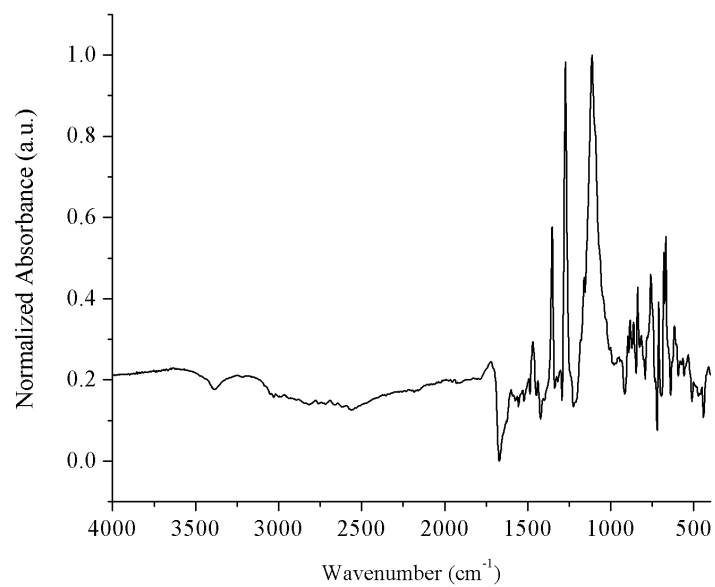
Asymmetric t-butyl TiO^iPr Solid state ATR spectrum



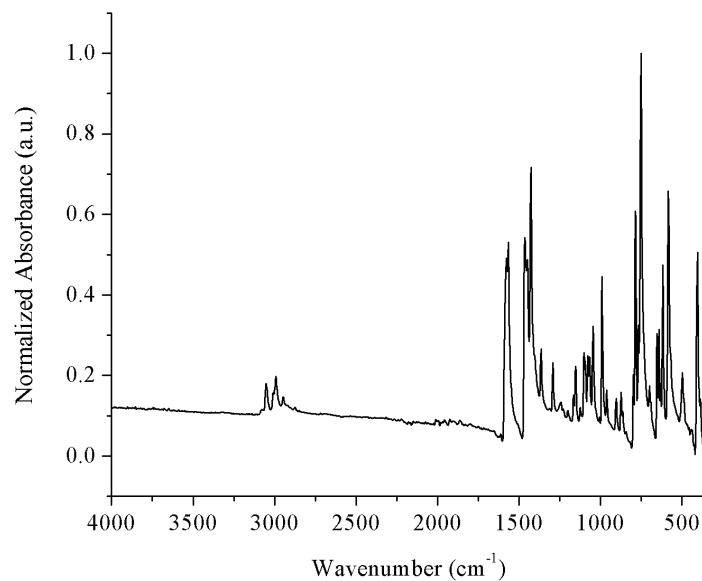
Symmetric Methyl TiOⁱPr Solid state ATR spectrum



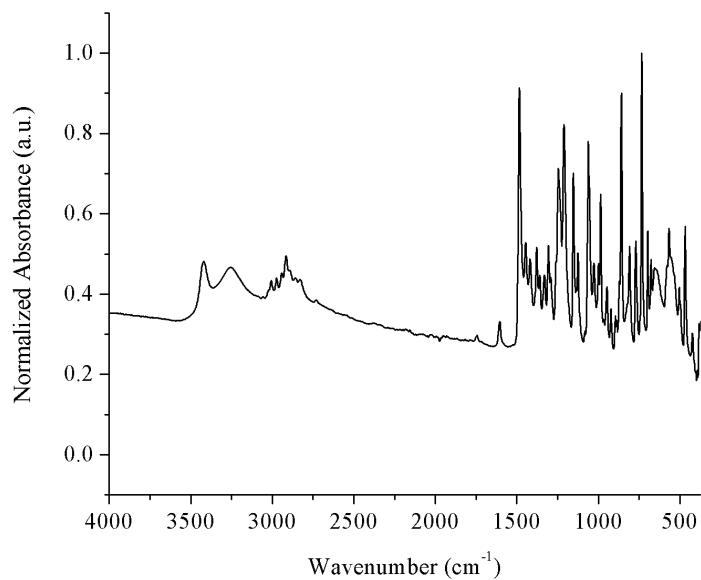
Cr^{III}OTi^{IV} Solid state ATR spectrum



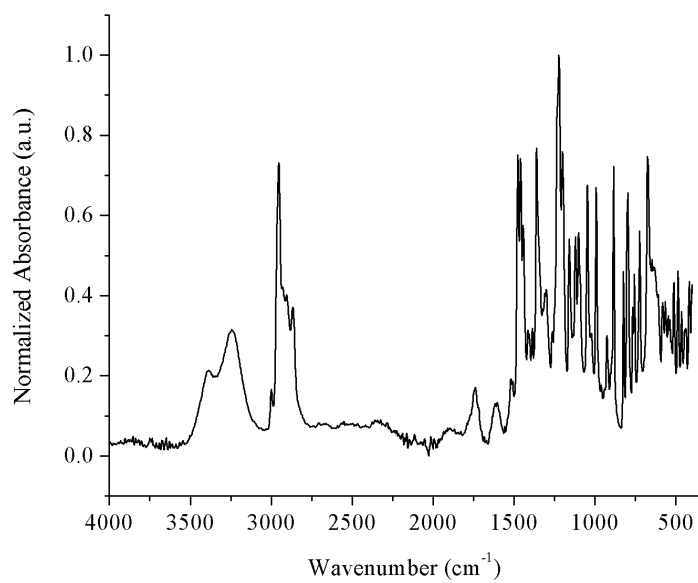
$\text{Fe}^{\text{III}}\text{OTi}^{\text{IV}}$ Solid state ATR spectrum



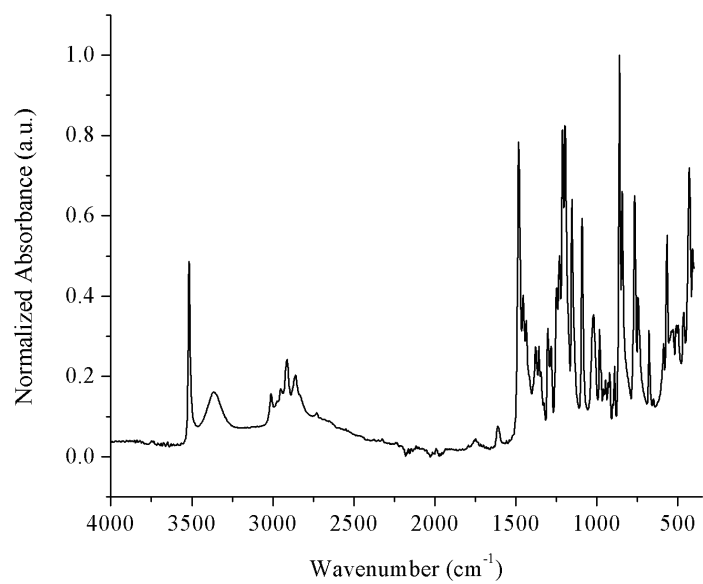
Py_5Me_2 Solid state ATR spectrum



***N,N*-bis(2-hydroxy-3,5-dimethylbenzyl)-2-aminoethanol**
Solid state ATR spectrum



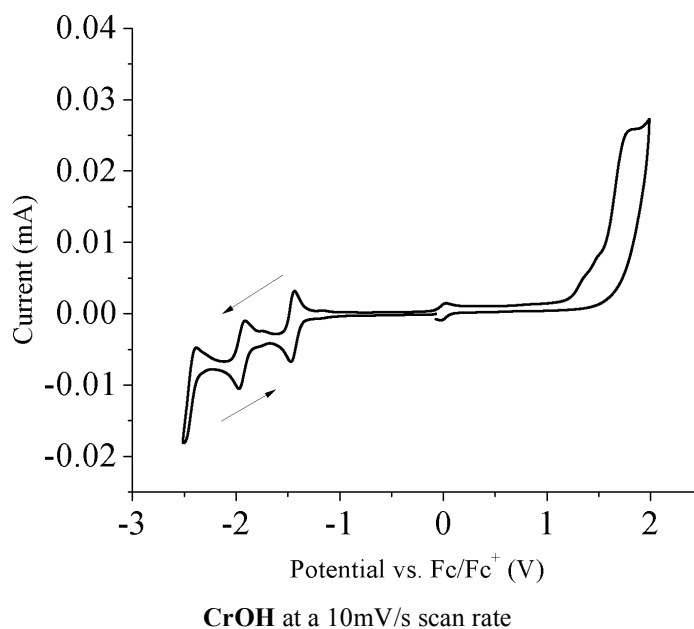
6,6'-(((2-hydroxyethyl)azanediy)bis(methylene))bis(2,4-di-*tert*-butylphenol) Solid state ATR spectrum

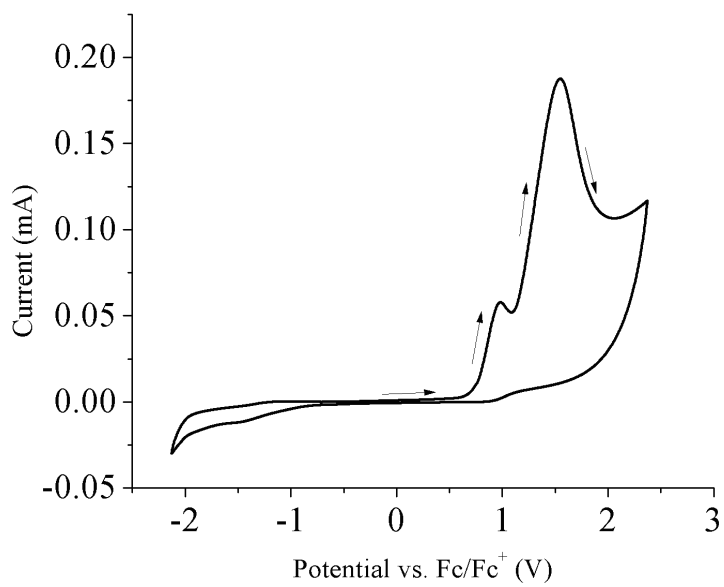


6,6',6''-(nitrilotris(methylene))tris(2,4-dimethylphenol)
Solid state ATR spectrum

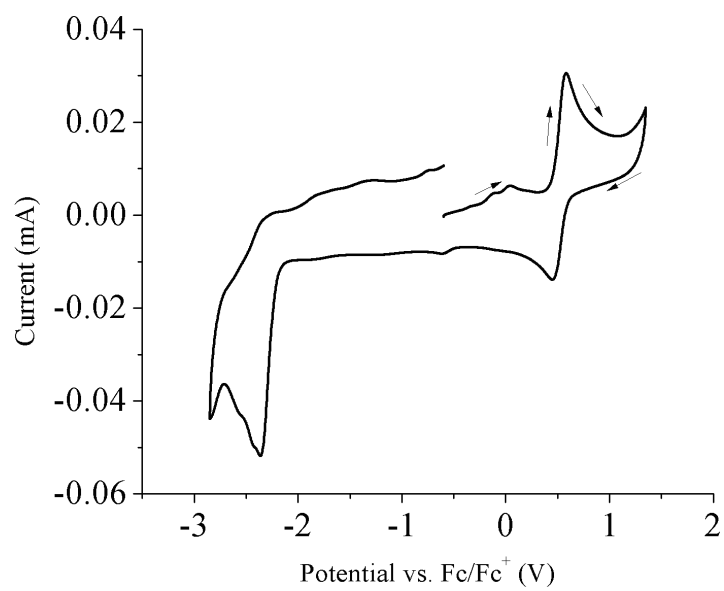
Appendix D Electrochemistry Supplemental Information and Voltammograms

Cyclic voltammetry experiments were performed using a BioLogic SP-200 potentiostat/galvanostat employing a glassy carbon working electrode, a silver wire reference electrode, and a platinum wire auxiliary electrode. Crystalline Ferrocene was added as an internal standard to which all CV's are referenced to ($\text{Fc}/\text{Fc}^+ = 0 \text{ eV}$). Unless otherwise noted, all CV's were taken in a .10 M solution of tetrabutylammonium hexafluorophosphate in freshly distilled acetonitrile under aerobic conditions. The scan rate for all CV's was 100 mV/s unless otherwise stated. Tetrabutylammonium hexafluorophosphate was recrystallized from unstabilized, 200 proof hot ethanol four times prior to use in electrochemical experiments.

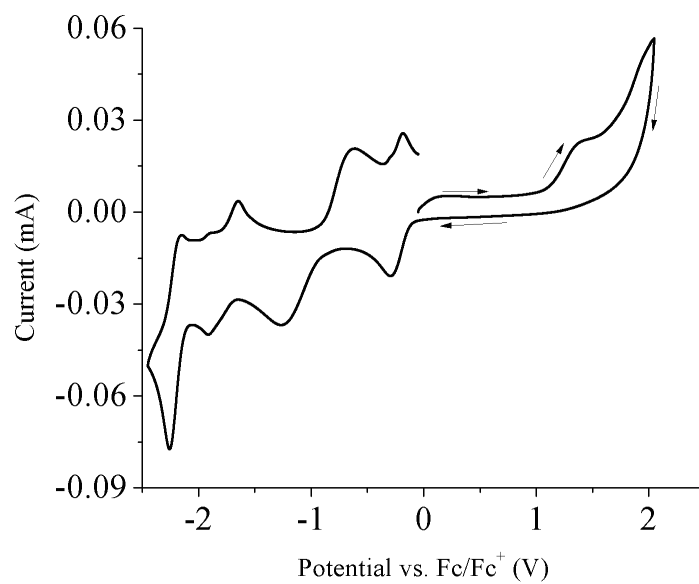
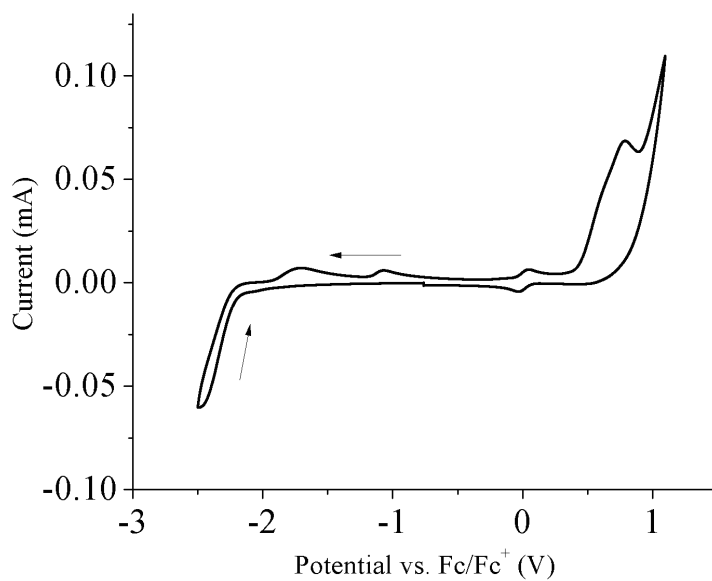


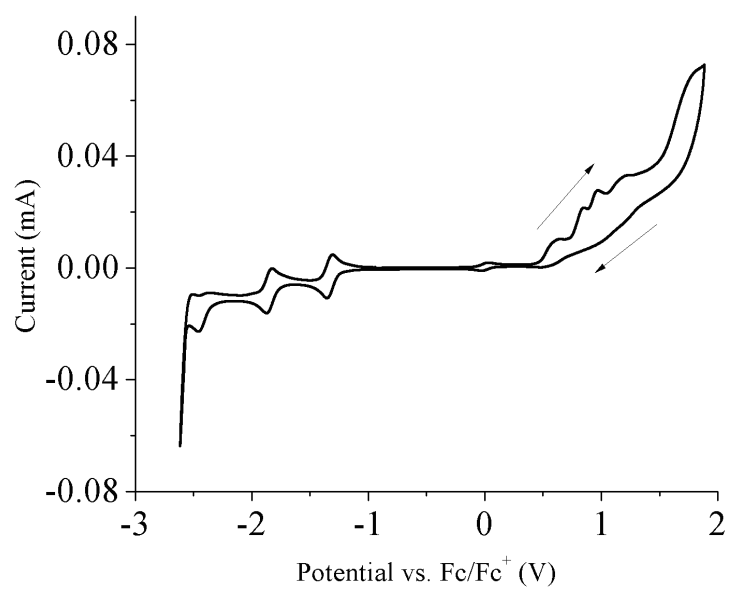


CrOH in trifluorotoluene in a .10 M solution of tetrabutylammonium BAr₄⁻

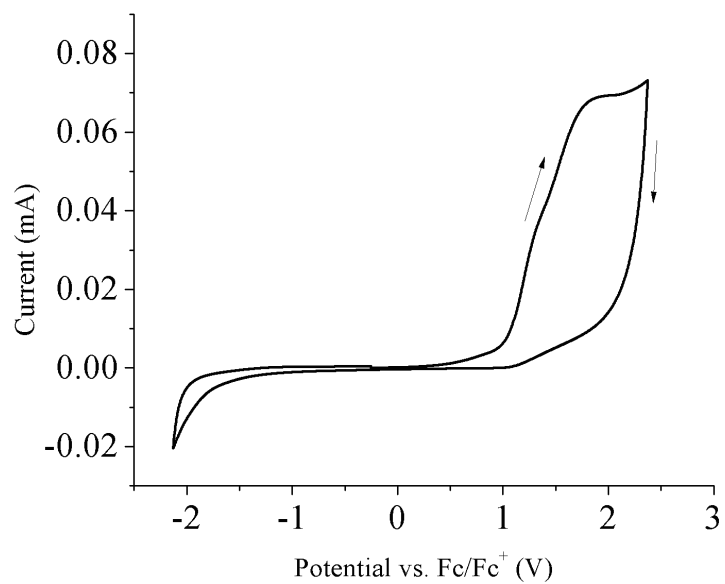


FeOH

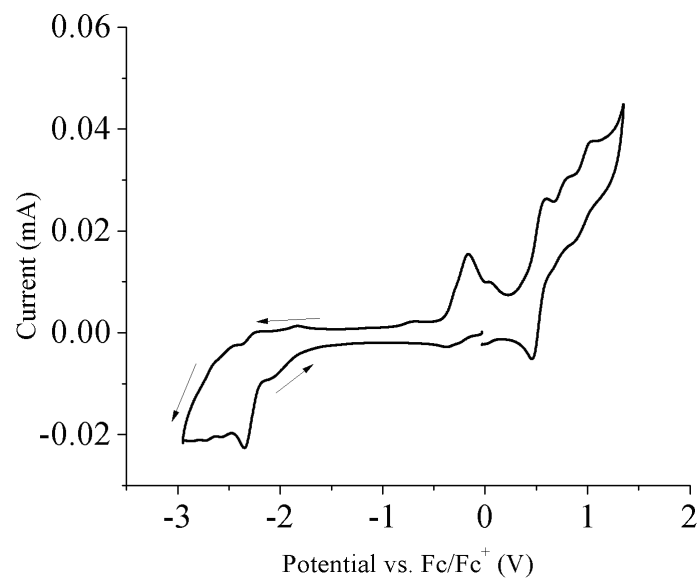
**CoOH****Asymmetric Methyl TiOⁱPr in dichloromethane**



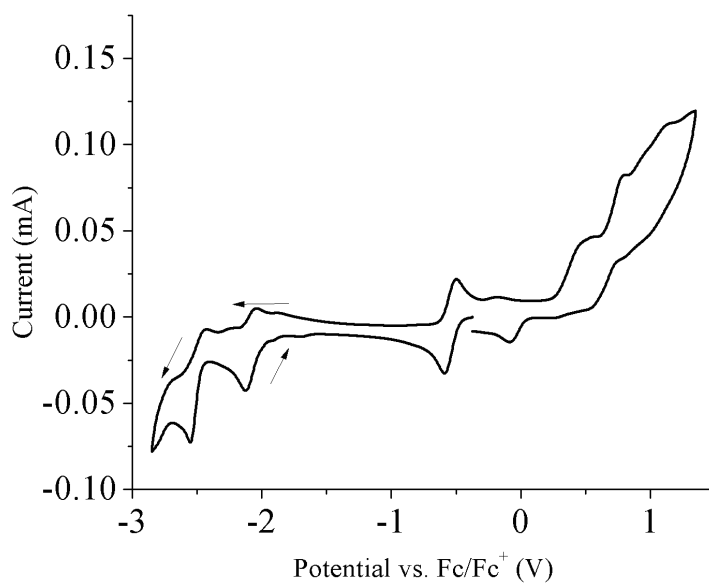
$\text{Cr}^{\text{III}}\text{OTi}^{\text{IV}}$ at a scan rate of 10 mV/s



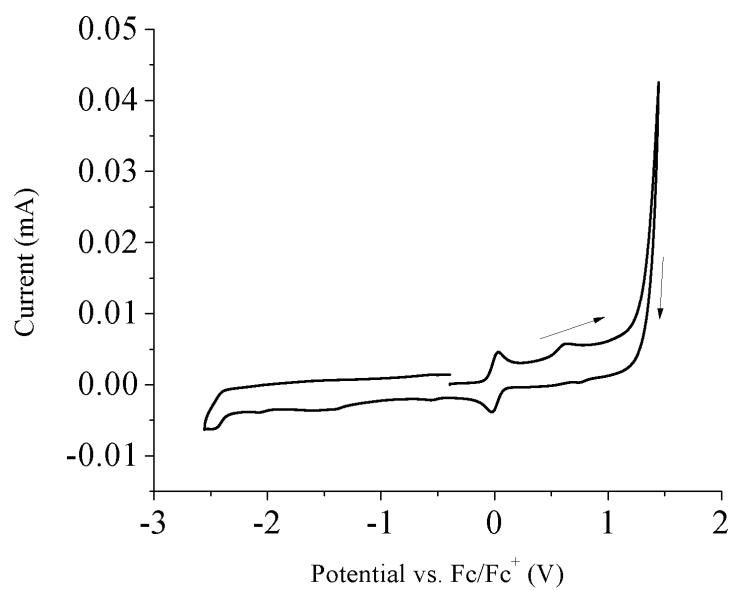
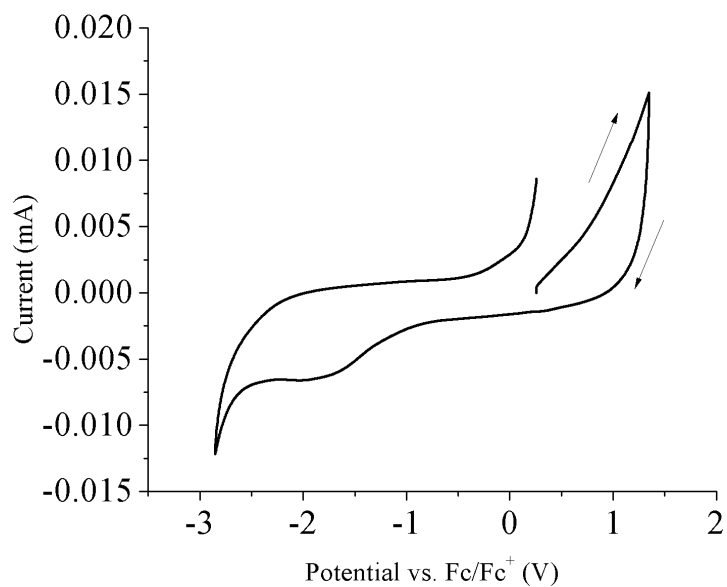
$\text{Cr}^{\text{III}}\text{OTi}^{\text{IV}}$ in trifluorotoluene in a .10 M solution of tetrabutylammonium BAR_4^+ at a 50 mV/s scan rate

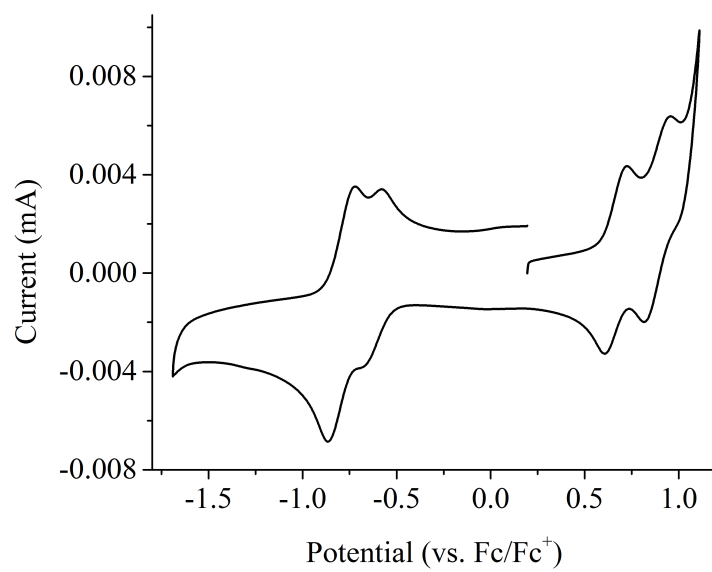


Fe^{III}OTi^{IV} at a 10 mV/s scan rate



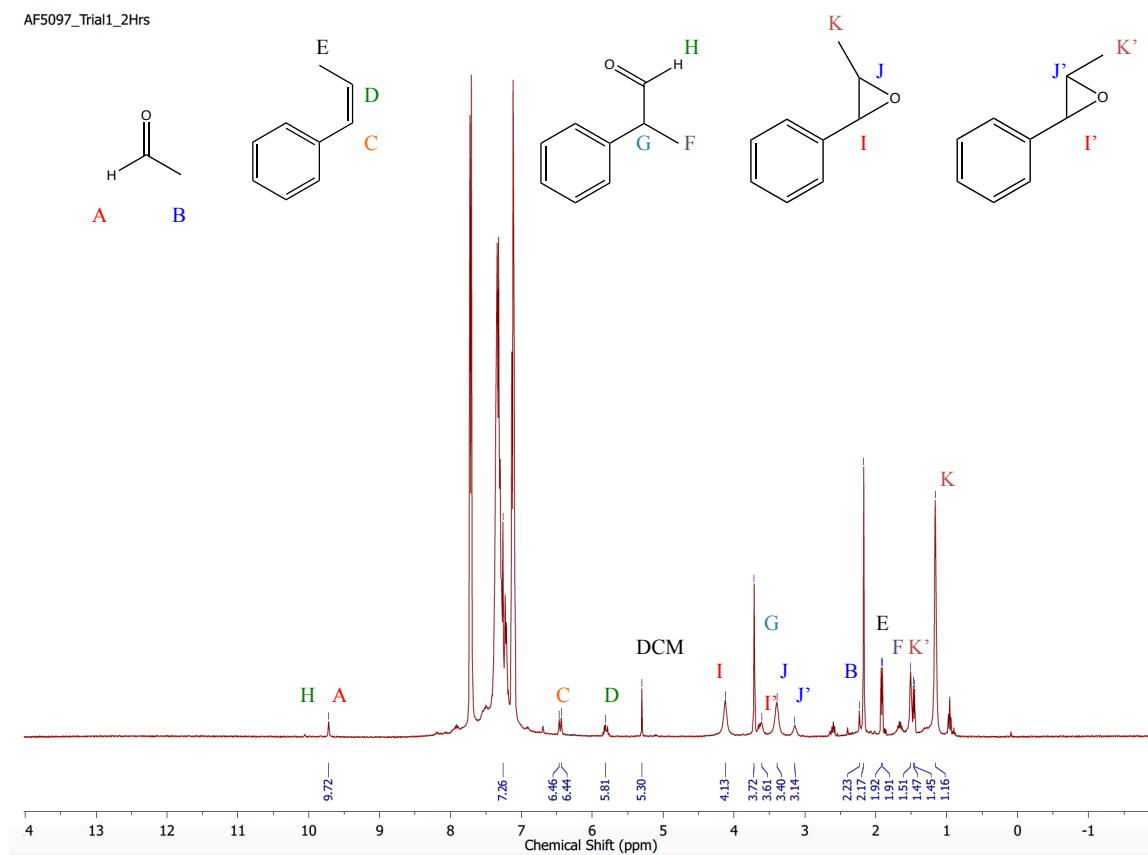
Co^{III}OTi^{IV} at a 50 mV/s scan rate

**Py₅Me₂****N,N-bis(2-hydroxy-3,5-dimethylbenzyl)-2-aminoethanol**



MnTPP(DMF) in dichloromethane

Appendix E Nuclear Magnetic Resonance Spectra



Representative ^1H NMR of the epoxidation of *cis*- β -methyl styrene in CDCl_3 . The reaction temperature throughout this trial was 22.3 $^\circ\text{C}$ and performed under aerobic conditions.

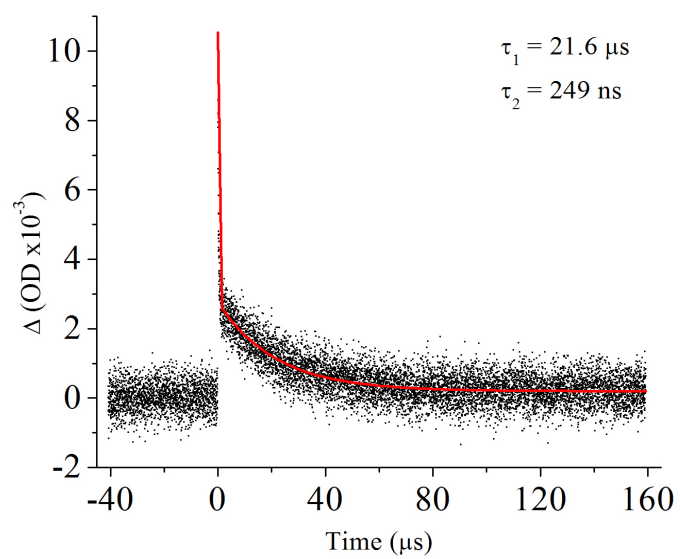
Appendix F Transient Absorption and Emission Spectra

Nanosecond Pump-Probe Measurements

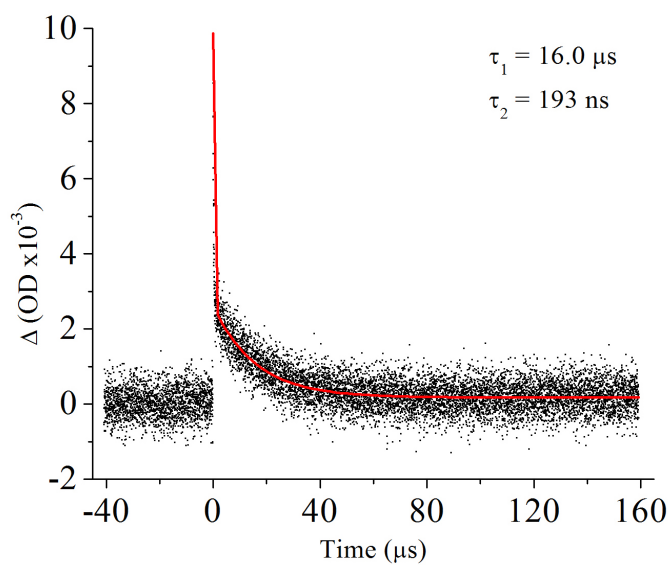
Solutions for all measurements were prepared in an inert atmosphere glovebox (Innovative Technologies) filled with nitrogen gas in an Schlenk-valve sealed fluorescence cuvette with an extended neck and freeze-pump-thaw chamber. All transient absorption measurements and emission lifetimes were obtained on an LP920 laser flash photolysis system (Edinburgh Instruments). The excitation source was the Vibrant 355 LD-UVM Nd:YAG/OPO system at a frequency of 1 Hz (Opotek). Data acquisition controlled by the L900 software program (Edinburgh Instruments). A bandpass filter was used on the excitation beam prior to introduction to the sample (380 nm) to filter out visible light. In the visible region, kinetic traces were collected with a PMT (R928 Hamamatsu) and spectra were collected with an iStar ICCD camera (Andor Technology). Each data point is the result of 20 averages in addition to a probe and emission background. The excitation wavelength was set to 300 nm and probed at 475 nm unless otherwise noted. A 6.6×10^{-5} M $\text{Cr}^{\text{III}}\text{OTi}^{\text{IV}}$ solution in dichloromethane was prepared prior to each measurement to give an optical density of approximately 0.7 absorbance units at the excitation wavelength. The excitation power was set to 2.4 mJ/pulse and measured prior to each experiment using a NovaII/PD300-UV power meter/detector (Ophir). Kinetic traces of $\text{Cr}^{\text{III}}\text{OTi}^{\text{IV}}$ and $\text{Cr}^{\text{III}}\text{OH}$ were fit to bi-exponential decay functions using OriginPro 8 software.

Temperature Dependence

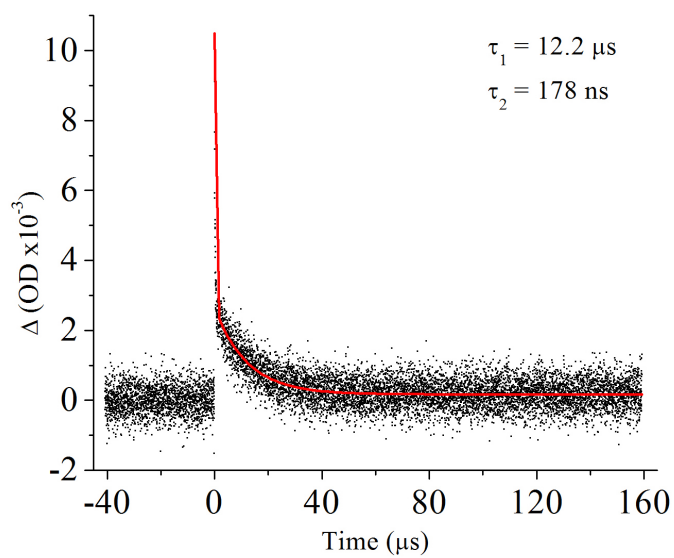
Variable temperature measurements were obtained CoolSpeK UV/CD and cooled with liquid nitrogen (Unisoku). Samples were loaded into a Schlenk-valve sealed 1 cm path length fluorescence cuvette equipped with an extended neck and freeze-pump-thaw chamber. Measurements were taken in 10 °C increments starting at the lower-limit. The sample was let equilibrate for 15 minutes at each temperature interval before data was acquired.



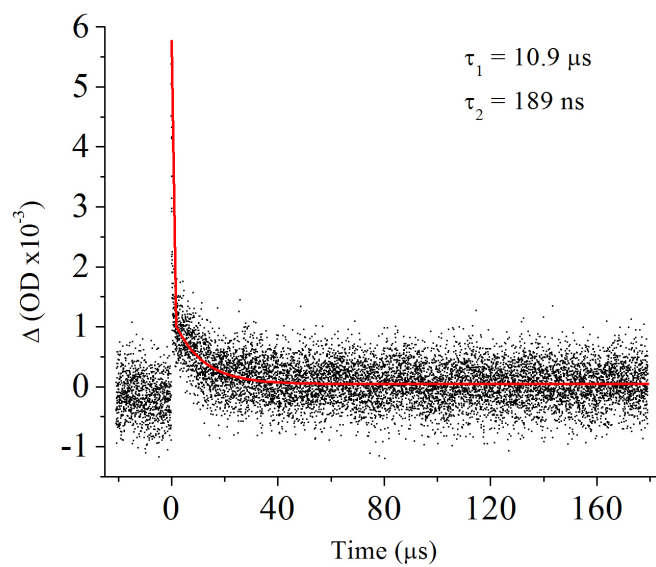
$\text{Cr}^{\text{III}}\text{OTi}^{\text{IV}}$ at $-80\text{ }^{\circ}\text{C}$ in DCM with a 300 nm Pump and 475 nm Probe



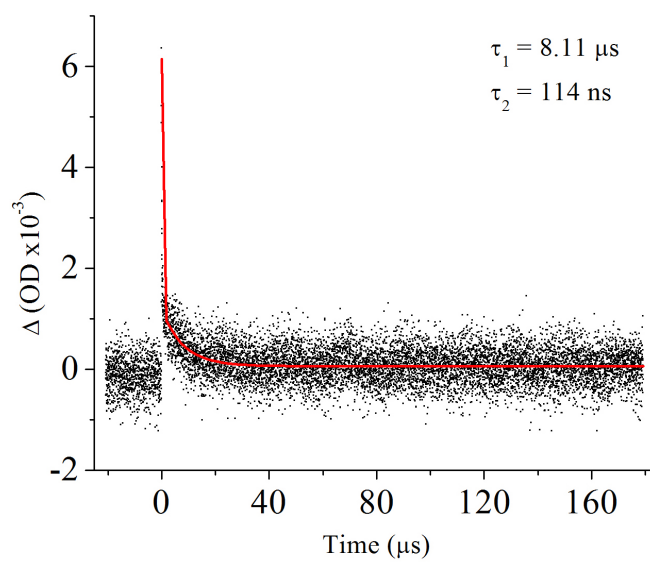
$\text{Cr}^{\text{III}}\text{OTi}^{\text{IV}}$ at $-70\text{ }^{\circ}\text{C}$ in DCM with a 300 nm Pump and 475 nm Probe



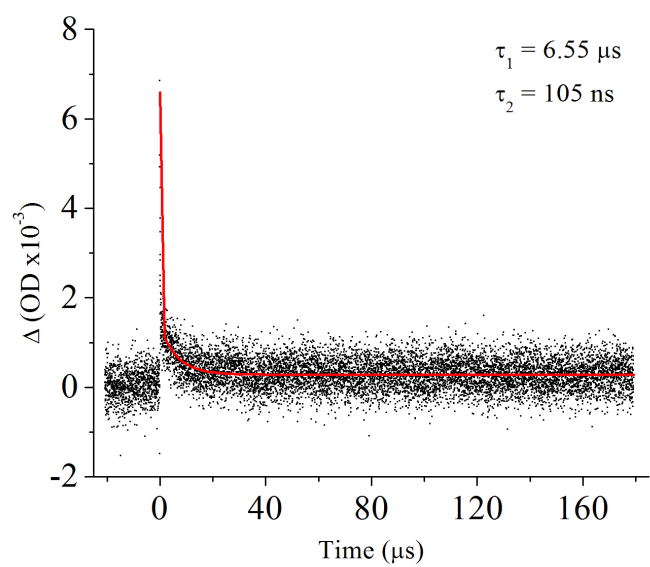
$\text{Cr}^{\text{III}}\text{OTi}^{\text{IV}}$ at $-60\text{ }^{\circ}\text{C}$ in DCM with a 300 nm Pump and 475 nm Probe



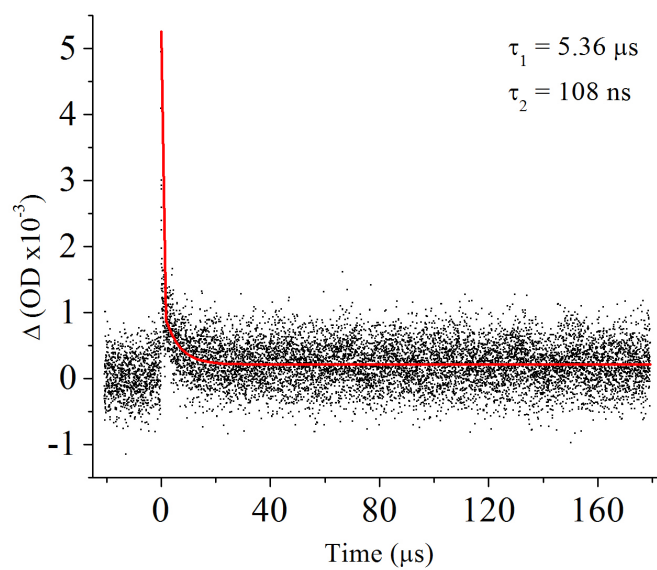
$\text{Cr}^{\text{III}}\text{OTi}^{\text{IV}}$ at $-50\text{ }^{\circ}\text{C}$ in DCM with a 300 nm Pump and 475 nm Probe



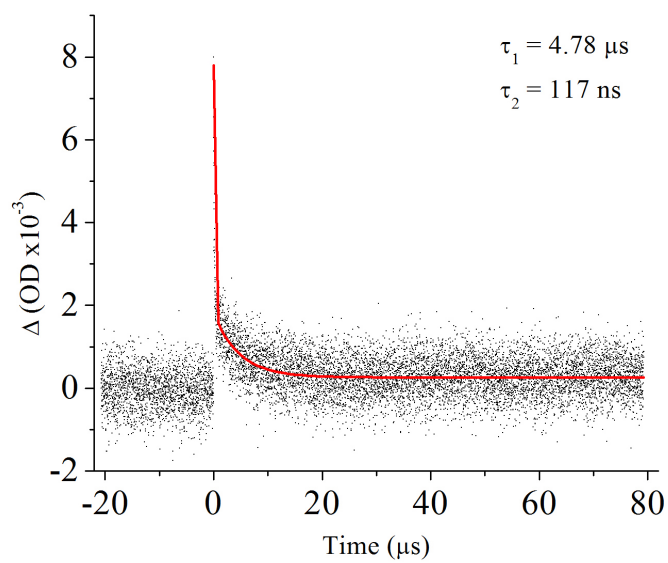
$\text{Cr}^{\text{III}}\text{OTi}^{\text{IV}}$ at $-40\text{ }^{\circ}\text{C}$ in DCM with a 300 nm Pump and 475 nm Probe



$\text{Cr}^{\text{III}}\text{OTi}^{\text{IV}}$ at $-30\text{ }^{\circ}\text{C}$ in DCM with a 300 nm Pump and 475 nm Probe



$\text{Cr}^{\text{III}}\text{OTi}^{\text{IV}}$ at $-20\text{ }^{\circ}\text{C}$ in DCM with a 300 nm Pump and 475 nm Probe



$\text{Cr}^{\text{III}}\text{OTi}^{\text{IV}}$ at $-10\text{ }^{\circ}\text{C}$ in DCM with a 300 nm Pump and 475 nm Probe

Ultrafast Pump-Probe Transient Absorption Measurements

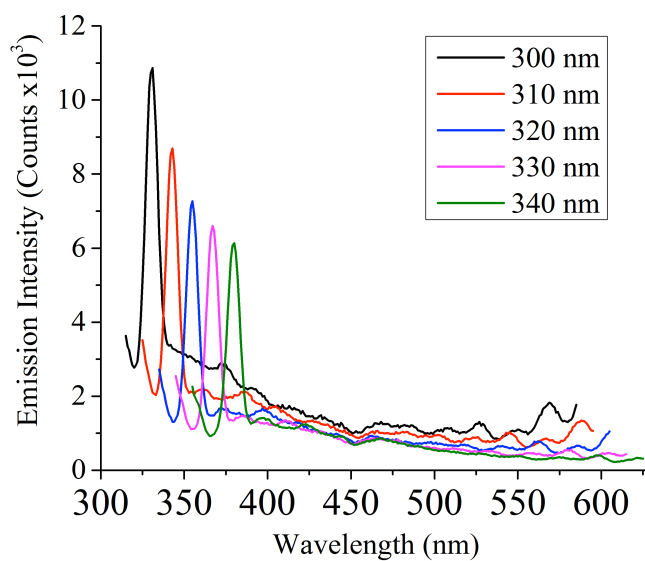
Ultrafast pump-probe measurements on $\text{Fe}^{\text{III}}\text{OTi}^{\text{IV}}$ were performed using a Helios transient absorption instrument produced by Ultrafast Systems. Not all of the laser power was used for measurements, as a portion of the outputted intensity from the 1 kHz Ti:Sapphire regenerative amplifier (4 mJ, 100 fs fwhm) was split into the excitation and probe beam lines. The probe beam has a 6 nanosecond optical stage delay while the excitation beam was directed into the optical parametric amplifier (Coherent OPerA Solo) for 380/400 nm excitation. Transient absorption measurements were performed in the UV/Visible region of the spectrum using white light producing crystals. The excitation beam was focused into a 800 μm spot on the sample cuvette and overlapped with the probe beam. The sample of $\text{Fe}^{\text{III}}\text{OTi}^{\text{IV}}$ was prepared in spectroscopic grade dichloromethane that was freeze-pump-thawed and dried over 4 \AA molecular sieves prior to use. Measurements were taken in a 1 mm pathlength quartz cuvette affixed with a Schlenk valve to preserve an inert atmosphere throughout the experiment. An optical density of approximately .4 absorbance units at 400 nm was prepared to obtain an optimized spectrum. Data was analyzed and presented using Origin Pro8. Ground state EAS was taken before and after obtaining the ultrafast data, which revealed no measureable photodecomposition.

Static Emission Spectra and Fluorescence Quantum Yield of $\text{Cr}^{\text{III}}\text{OTi}^{\text{IV}}$

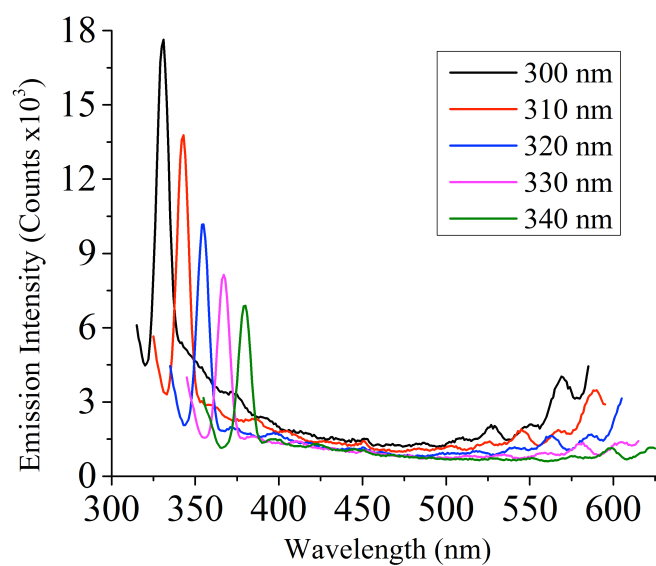
The fluorescence quantum yield of $\text{Cr}^{\text{III}}\text{OTi}^{\text{IV}}$ was compared to that of Anthracene with an excitation wavelength of 310 nm. Anthracene's fluorescence measurements were taken in spectroscopic grade ethanol (190 proof) whereas $\text{Cr}^{\text{III}}\text{OTi}^{\text{IV}}$ was measured in spectroscopic grade dichloromethane. Both solvents were degassed with four cycles of freeze-pump-thaw in a sealed Schlenk flask. It was determined using the comparative method using the same experimental conditions and on the same day. The quantum yield was calculated using equation F.1. Where Φ_A is the measured quantum yield of the analyte and Φ_S is the reported quantum yield of the standard. ∇_A and ∇_S are the slopes obtained of the linear fit for the absorbance versus integrated fluorescence intensity plot at the excitation

wavelength. η are the refractive indices for the solvents used in the emission and absorbance experiments (1.3614 for ethanol and 1.4241 for dichloromethane).

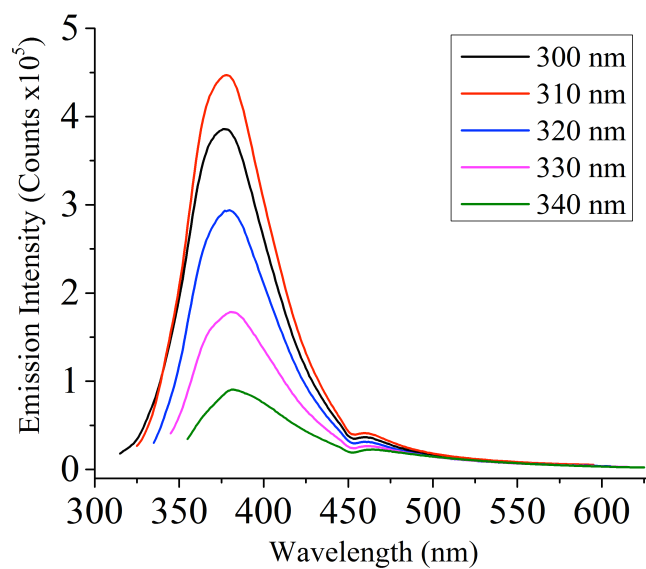
$$\text{Equation F.1 } \Phi_A = \frac{\nu_A \eta_A^2}{\nu_S \eta_S^2}$$



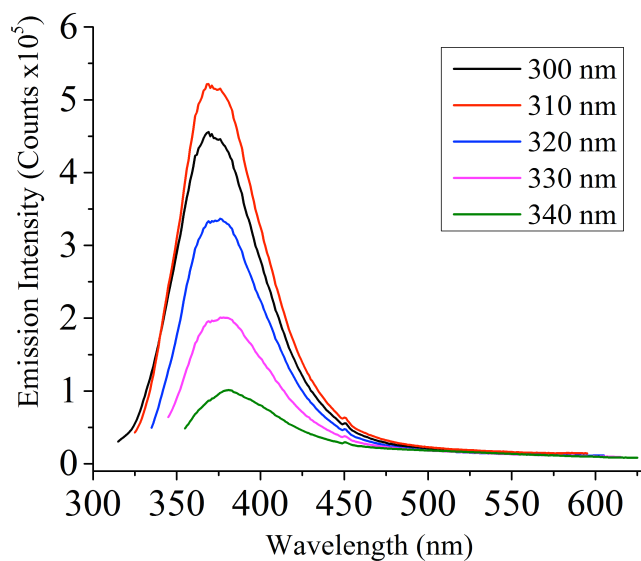
Uncorrected emission spectrum of the DCM used for static emission experiments with excitation wavelength designated. An intense Raman band is visible.



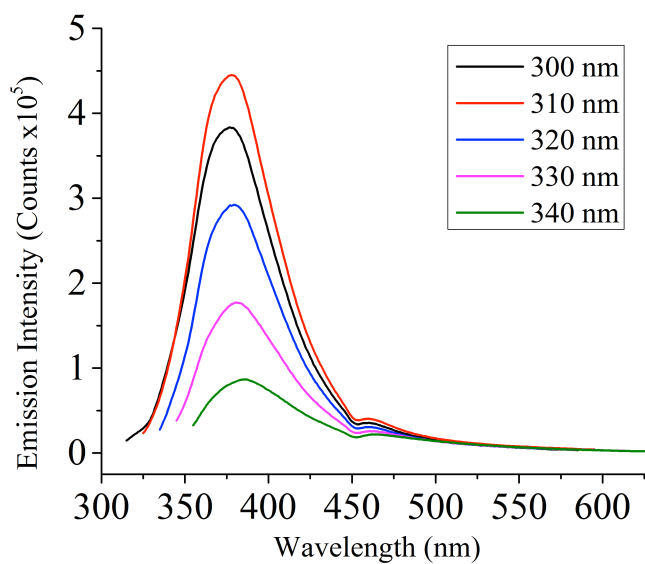
Corrected emission spectrum of the DCM used for static emission experiments with excitation wavelength designated. An intense Raman band is visible.



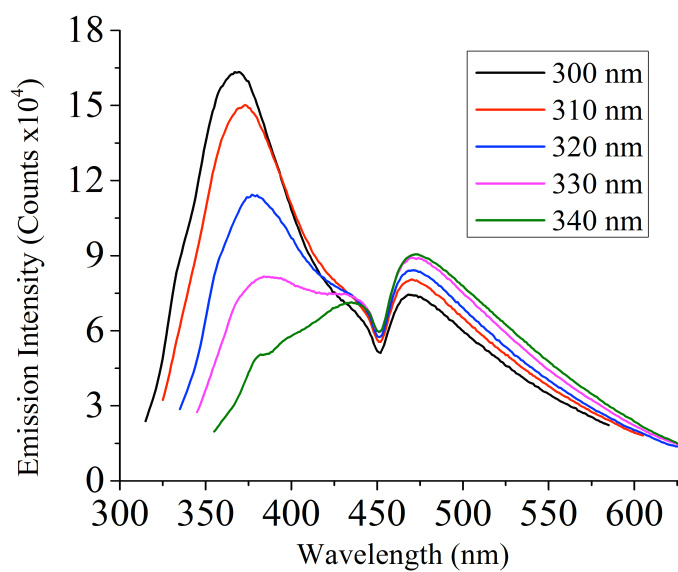
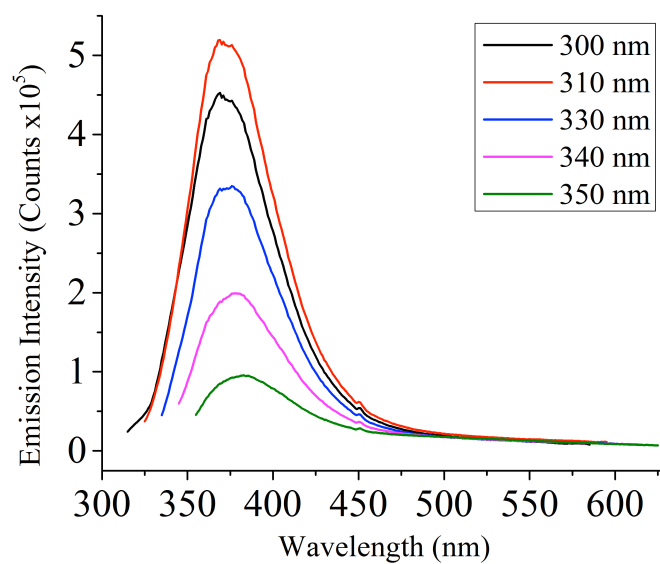
Uncorrected emission spectrum of Cr^{III}OTi^{IV} in DCM with excitation wavelength designated. Without DCM subtracted.

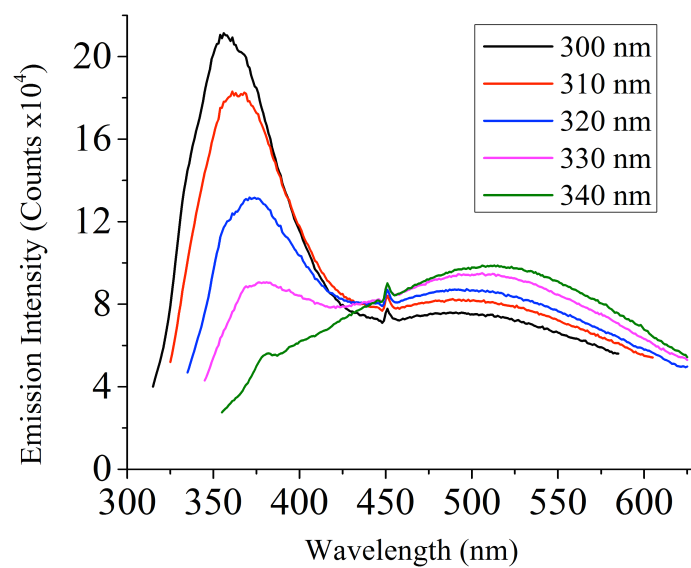


Corrected emission spectrum of Cr^{III}OTi^{IV} in DCM with excitation wavelength designated. Without DCM subtracted.

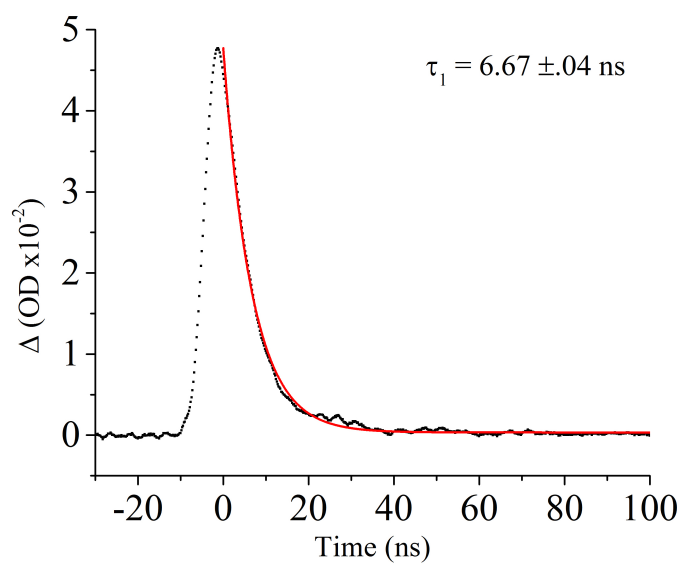


Uncorrected emission spectrum of Cr^{III}OTi^{IV} in DCM with excitation wavelength designated. With DCM subtracted.

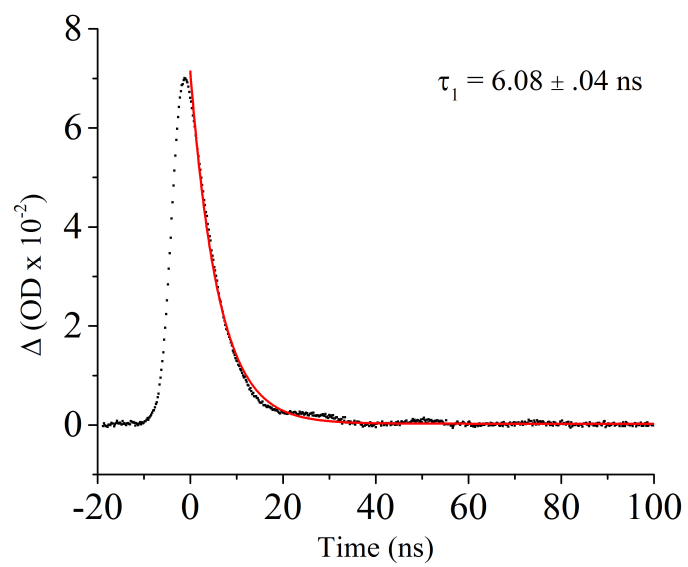




Corrected emission spectrum of CrOH in DCM with excitation wavelength designated. Emission at 475 nm is characteristic of the photodecomposition product.



Emission lifetime of Cr^{III}OTi^{IV} obtained in dichloromethane. Fitted to a single exponential decay function using Origin Pro8.



Emission lifetime of CrOH obtained in dichloromethane. Fitted to a single exponential decay function using Origin Pro8.

Appendix G Single Crystal Data

Single Crystal Refinement Data for FeOH

A dark orange plate-like specimen of $C_{37}H_{38}F_6FeN_5O_9S_2$, approximate dimensions 0.067 mm x 0.143 mm x 0.478 mm, was used for the X-ray crystallographic analysis. Instrument description The X-ray intensity data were measured.

The total exposure time was 10.62 hours. Integration The frames were integrated with the Bruker SAINT software package using a narrow-frame algorithm. The integration of the data using a triclinic unit cell yielded a total of 65851 reflections to a maximum θ angle of 28.56° (0.74 Å resolution), of which 9891 were independent (average redundancy 6.658, completeness = 98.8%, $R_{int} = 3.94\%$, $R_{sig} = 3.21\%$) and 7974 (80.62%) were greater than $2\sigma(F^2)$. Unit cell The final cell constants of $a = 12.0099(5)$ Å, $b = 12.8695(6)$ Å, $c = 15.2089(7)$ Å, $\alpha = 65.384(2)^\circ$, $\beta = 78.509(2)^\circ$, $\gamma = 66.816(2)^\circ$, volume = $1962.75(16)$ Å³, are based upon the refinement of the XYZ-centroids of 294 reflections above $20 \sigma(I)$ with $3.820^\circ < 2\theta < 65.45^\circ$. Scaling Data were corrected for absorption effects using the multi-scan method (SADABS). The ratio of minimum to maximum apparent transmission was 0.947. The calculated minimum and maximum transmission coefficients (based on crystal size) are 0.7690 and 0.9620.

Structure solution The structure was solved and refined using the Bruker SHELXTL Software Package, using the space group P -1, with $Z = 2$ for the formula unit, $C_{37}H_{38}F_6FeN_5O_9S_2$. Structure refinement The final anisotropic full-matrix least-squares refinement on F^2 with 624 variables converged at $R1 = 3.42\%$, for the observed data and $wR2 = 8.69\%$ for all data. The goodness-of-fit was 1.031. The largest peak in the final difference electron density synthesis was $0.519 e^-/\text{Å}^3$ and the largest hole was $-0.444 e^-/\text{Å}^3$ with an RMS deviation of $0.065 e^-/\text{Å}^3$. On the basis of the final model, the calculated density was 1.575 g/cm^3 and $F(000)$, 958 e^- . Structure Packing Sample and crystal data

Table 1. Sample and crystal data for rds468.

Identification code	rds468
Chemical formula	C ₃₇ H ₃₈ F ₆ FeN ₅ O ₉ S ₂
Formula weight	930.69 g/mol
Temperature	100(2) K
Wavelength	0.71073 Å
Crystal size (mm)	0.067x0.143x0.478
Crystal habit	dark orange plate
Crystal system	triclinic
Space group	P -1
Unit cell dimensions	a = 12.0099(5) Å b = 12.8695(6) Å c = 15.2089(7) Å
Volume	1962.75(16) Å ³
Z	2
Density (calculated)	1.575 g/cm ³
Absorption coefficient	0.581 mm ⁻¹
F(000)	958

Single Crystal Refinement Data for Co^{III}OTi^{IV}

A dark red-purple prism-like specimen of C₅₅H₅₅CoF₆N₈O₁₀S₂Ti, approximate dimensions 0.184 mm x 0.242 mm x 0.341 mm, was used for the X-ray crystallographic analysis. Instrument description The X-ray intensity data were measured.

The total exposure time was 15.59 hours. Integration The frames were integrated with the Bruker SAINT software package using a narrow-frame algorithm. The integration of the data using a triclinic unit cell yielded a total of 126008 reflections to a maximum θ angle of 30.51° (0.70 Å resolution), of which 16878 were independent (average redundancy 7.466, completeness = 100.0%, R_{int} = 3.66%, R_{sig} = 2.56%) and 13646 (80.85%) were greater than 2 σ (F²). Unit cell The final cell constants of \underline{a} = 12.7561(5) Å, \underline{b} = 13.3757(5) Å, \underline{c} =

18.1228(8) Å, $\alpha = 73.9640(10)^\circ$, $\beta = 70.2320(10)^\circ$, $\gamma = 76.7800(10)^\circ$, volume = 2765.24(19) Å³, are based upon the refinement of the XYZ-centroids of 129 reflections above 20 $\sigma(I)$ with $4.399^\circ < 2\theta < 50.86^\circ$. Scaling Data were corrected for absorption effects using the multi-scan method (SADABS). The ratio of minimum to maximum apparent transmission was 0.960. The calculated minimum and maximum transmission coefficients (based on crystal size) are 0.8200 and 0.8970.

Structure solution Structure refinement The final anisotropic full-matrix least-squares refinement on F^2 with 756 variables converged at $R1 = 4.24\%$, for the observed data and $wR2 = 12.16\%$ for all data. The goodness-of-fit was 1.023. The largest peak in the final difference electron density synthesis was 1.579 e⁻/Å³ and the largest hole was -1.023 e⁻/Å³ with an RMS deviation of 0.083 e⁻/Å³. On the basis of the final model, the calculated density was 1.529 g/cm³ and $F(000)$, 1312 e⁻.

Table 1. Sample and crystal data for rds269.

Identification code	rds269
Chemical formula	C ₅₅ H ₅₅ CoF ₆ N ₈ O ₁₀ S ₂ Ti
Formula weight	1273.02
Temperature	110(2) K
Wavelength	0.71073 Å
Crystal size (mm)	0.184x0.242x0.341
Crystal habit	dark red-purple prism
Crystal system	triclinic
Space group	P -1
Unit cell dimensions	a = 12.7561(5) Å b = 13.3757(5) Å c = 18.1228(8) Å
Volume	2765.24(19) Å ³
Z	2
Density (calculated)	1.529 g/cm ³
Absorption coefficient	0.607 mm ⁻¹
F(000)	1312

Single Crystal Refinement Experimental Information for CrOH

The sample (x12031) was submitted by Travis Lekich of the Weare research group at North Carolina State University. The sample was mounted on a Mitegen polyimide micromount with a small amount of Paratone N oil. All X-ray measurements were made on a Bruker-Nonius Kappa Axis X8 Apex2 diffractometer at a temperature of 110 K. The unit cell dimensions were determined from a symmetry constrained fit of 9700 reflections with $4.88^\circ < 2\theta < 65.06^\circ$. The data collection strategy was a number of ω and ϕ scans which collected data up to 70.2° (2θ). The frame integration was performed using SAINT. The resulting raw data was scaled and absorption corrected using a multi-scan averaging of symmetry

equivalent data using SADABS.

The structure was solved by direct methods using the SIR92 program. All non-hydrogen atoms were obtained from the initial solution. The hydrogen atoms were introduced at idealized positions and were allowed to ride on the parent atom. The structure also contained a region located about a crystallographic inversion center which was occupied by solvent molecules (presumably pentane and diethyl ether.) However, no chemically sensible model could be obtained for this portion of the structure. Therefore, the SQUEZZE procedure as implemented in PLATON was used to subtract out the solvent's contribution to the diffraction pattern. The structural model was fit to the data using full matrix least-squares based on F^2 . The calculated structure factors included corrections for anomalous dispersion from the usual tabulation. The structure was refined using the XL program from SHELXTL, graphic plots were produced using the NRCVAX crystallographic program suite. Additional information and other relevant literature references can be found in the reference section of the Facility's Web page (<http://www.xray.ncsu.edu>).

Single Crystal Refinement Data for Cr^{III}OTi^{IV}

A pink-orange rod-like specimen of $C_{115}H_{77}B_2Cl_4CrF_{48}N_6O_4Ti$, approximate dimensions 0.100 mm x 0.160 mm x 0.400 mm, was used for the X-ray crystallographic analysis. The X-ray intensity data were measured.

The total exposure time was 18.27 hours. The frames were integrated with the Bruker SAINT software package using a narrow-frame algorithm. The integration of the data using a monoclinic unit cell yielded a total of 139961 reflections to a maximum θ angle of 26.56° (0.79 Å resolution), of which 23703 were independent (average redundancy 5.905, completeness = 98.3%, $R_{int} = 4.14\%$, $R_{sig} = 2.99\%$) and 19058 (80.40%) were greater than $2\sigma(F^2)$. The final cell constants of $\underline{a} = 13.4112(3)$ Å, $\underline{b} = 18.3529(5)$ Å, $\underline{c} = 46.9774(11)$ Å, $\beta = 90.4300(10)^\circ$, volume = $11562.4(5)$ Å³, are based upon the refinement of the XYZ-centroids of 9785 reflections above $20 \sigma(I)$ with $4.438^\circ < 2\theta < 52.36^\circ$. Data were corrected for absorption effects using the multi-scan method (SADABS). The ratio of minimum to maximum apparent transmission was 0.883. The calculated minimum and maximum transmission coefficients (based on crystal size) are 0.6583 and 0.7454.

The structure was solved and refined using the Bruker SHELXTL Software Package, using the space group $P 1 21/n 1$, with $Z = 4$ for the formula unit, $C_{115}H_{77}B_2Cl_4CrF_{48}N_6O_4Ti$. The final anisotropic full-matrix least-squares refinement on F^2 with 1684 variables converged at $R1 = 6.91\%$, for the observed data and $wR2 = 19.20\%$ for all data. The goodness-of-fit was 1.036. The largest peak in the final difference electron density synthesis was $1.692 \text{ e}^-/\text{\AA}^3$ and the largest hole was $-1.725 \text{ e}^-/\text{\AA}^3$ with an RMS deviation of $0.096 \text{ e}^-/\text{\AA}^3$. On the basis of the final model, the calculated density was 1.598 g/cm^3 and $F(000)$, 5588 e^- .

Table 1. Sample and crystal data for rds031.

Identification code	rds031
Chemical formula	$C_{115}H_{77}B_2Cl_4CrF_{48}N_6O_4Ti$
Formula weight	2782.14
Temperature	110(2) K
Wavelength	q0.71073 Å
Crystal size (mm)	0.100x0.160x0.400
Crystal habit	pink-orange rod
Crystal system	monoclinic
Space group	P 1 21/n 1
Unit cell dimensions	a = 13.4112(3) Å b = 18.3529(5) Å c = 46.9774(11) Å
Volume	11562.4(5) Å ³
Z	4
Density (calculated)	1.598 g/cm ³
Absorption coefficient	0.389 mm ⁻¹
F(000)	5588

Single Crystal Refinement Data for CoOH

A violet-pink block-like specimen of $C_{31}H_{32}CoF_6N_5O_{10}S_2$, approximate dimensions 0.200 mm x 0.200 mm x 0.400 mm, was used for the X-ray crystallographic analysis. The X-ray intensity data were measured.

The total exposure time was 3.12 hours. The frames were integrated with the Bruker SAINT software package using a narrow-frame algorithm. The integration of the data using a monoclinic unit cell yielded a total of 74552 reflections to a maximum θ angle of 42.58° (0.53 Å resolution), of which 12350 were independent (average redundancy 6.037, completeness = 99.5%, R_{int} = 4.41%, R_{sig} = 3.74%) and 9857 (79.81%) were greater than $2\sigma(F^2)$. The final cell constants of \underline{a} = 8.6794(2) Å, \underline{b} = 20.0213(4) Å, \underline{c} = 9.7142(2) Å, β =

94.5880(10)°, volume = 1682.66(6) Å³, are based upon the refinement of the XYZ-centroids of 9051 reflections above 2 σ (I) with 5.129° < 2 θ < 79.94°. Data were corrected for absorption effects using the multi-scan method (SADABS). The ratio of minimum to maximum apparent transmission was 0.945. The calculated minimum and maximum transmission coefficients (based on crystal size) are 0.7576 and 0.8670.

The structure was solved and refined using the Bruker SHELXTL Software Package, using the space group P 1 21/m 1, with Z = 2 for the formula unit, C₃₁H₃₂CoF₆N₅O₁₀S₂. The final anisotropic full-matrix least-squares refinement on F² with 275 variables converged at R1 = 3.62%, for the observed data and wR2 = 9.90% for all data. The goodness-of-fit was 1.034. The largest peak in the final difference electron density synthesis was 0.787 e⁻/Å³ and the largest hole was -0.752 e⁻/Å³ with an RMS deviation of 0.092 e⁻/Å³. On the basis of the final model, the calculated density was 1.720 g/cm³ and F(000), 892 e⁻.

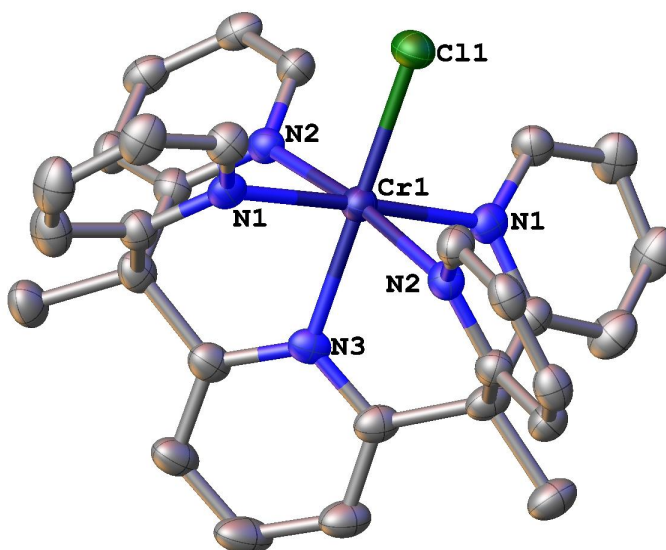
Table 1. Sample and crystal data for RDS008.

Identification code	RDS008
Chemical formula	C ₃₁ H ₃₂ CoF ₆ N ₅ O ₁₀ S ₂
Formula weight	871.67
Temperature	100(2) K
Wavelength	0.71073 Å
Crystal size (mm)	0.200x0.200x0.400
Crystal habit	violet-pink block
Crystal system	monoclinic
Space group	P 1 21/m 1
Unit cell dimensions	a = 8.6794(2) Å b = 20.0213(4) Å c = 9.7142(2) Å
Volume	1682.66(6) Å ³
Z	2
Density (calculated)	1.720 g/cm ³
Absorption coefficient	0.735 mm ⁻¹
F(000)	892

Single Crystal Refinement Experimental Information and Structure for CrCl

The sample (x13001) was submitted by John Nguyen of the Weare research group at North Carolina State University. The sample was mounted on a Mitegen polyimide micromount with a small amount of Paratone N oil. All X-ray measurements were made on a Bruker-Nonius Kappa Axis X8 Apex2 diffractometer at a temperature of 110 K. The unit cell dimensions were determined from a symmetry constrained fit of 9905 reflections with $4.88^\circ < 2\theta < 48.42^\circ$. The data collection strategy was a number of ω and φ scans which collected data up to 49.8° (2θ). The frame integration was performed using SAINT. The resulting raw data was scaled and absorption corrected using a multi-scan averaging of symmetry equivalent data using SADABS.

The structure was solved by direct methods using the XS program. All non-hydrogen atoms were obtained from the initial solution. The hydrogen atoms were introduced at idealized positions and were allowed to ride on the parent atom. The CF₃ groups containing carbon atoms C31, C38, C38, and C46 exhibited an orientational disorder. The alternative positions were for fluorine atoms were obtained from difference Fourier maps. The normalized occupancy for the major conformer refined to values 0.63(3) for C31, 0.570(19) for C38, 0.728(15) for C39 and 0.718(13) for C46. The C—F distances and F···F distances for these disordered groups were restrained to values 1.324 Å and 2.110 Å. These values were obtained from a CSD search of undisordered structures containing 3,5-difluoromethyl phenyl groups where the data were collected at temperatures of 120K or lower. There were 241 hits obtained from the CSD search. The structural model was fit to the data using full matrix least-squares based on F². The calculated structure factors included corrections for anomalous dispersion from the usual tabulation. The structure was refined using the XL program from SHELXTL, graphic plots were produced using the NRCVAX crystallographic program suite. Additional information and other relevant literature references can be found in the reference section of the Facility's Web page (<http://www.xray.ncsu.edu>).



Single Crystal Structure of CrCl